DEVELOPMENT AND VALIDATION OF LOWER- AND UPPER-EXTREMITY ROBOTIC MEDICAL EDUCATION TASK TRAINERS FOR NEUROLOGIC EXAMS

BY

YINAN PEI

DISSERTATION

Submitted in partial fulfillment of the requirements
for the degree of Doctor of Philosophy in Mechanical Engineering
in the Graduate College of the
University of Illinois Urbana-Champaign, 2022

Urbana, Illinois

Doctoral Committee:

Professor Elizabeth T. Hsiao-Wecksler, Chair and Director of Research
Associate Professor Mariana E. Kersh
Assistant Professor João Ramos
Assistant Professor Manuel E. Hernandez
Dr. Christopher M. Zallek, OSF HealthCare

ABSTRACT

During neurologic exams, clinicians perform manual assessments of various joints and rely on haptic experiential knowledge to diagnose underlying neurologic conditions. It is imperative to afford clinical learners more exposure to the haptic feeling of common abnormal behaviors. Traditionally, training is carried out on practice patients or even classmates, but outcomes are not always consistent and reliable. Alternatively, medical education training simulators could render accessible, safe, consistent, and scalable training environments.

Although simulators have been widely adopted for surgical and anatomical procedures, there are no commercial task trainers for practicing neurologic examination techniques. Task trainers that can simulate multiple behaviors at various severity levels should integrate high-fidelity force control capability into human-size limb mannequins. Considering the device shares many similar technical challenges to powered prosthetics and exoskeletons, we refer to this category of device as *robotic task trainers*. A few research prototypes have been proposed previously but none have been adopted publicly, possibly due to cost, maintenance, portability, or mechanical complexity issues.

In this dissertation research, we used a series elastic actuator (SEA) design strategy to develop robotic task trainers that achieve a balance across cost, size, and performance. Two prototype task trainers were developed. The lower-extremity trainer mimics ankle clonus and deep tendon reflex. The upper-extremity trainer replicates upper-arm spasticity, lead-pipe rigidity, and cogwheel rigidity. We discussed their design, sensing, modeling, and control aspects. Validation tests (benchtop performance and clinical expert assessments) highlight that these devices can be viable training solutions for learners in healthcare professions.

To My Family, Friends, and Cats

ACKNOWLEDGMENTS

I would like to first acknowledge my advisor, Prof. Elizabeth Hsiao-Wecksler, for her continuous and unconditional support throughout my graduate studies in the Human Dynamics and Controls Lab (HDCL). Liz has this unique talent to be able to see through people to know their essence, and then she will arrange a master plan for their growth until they live up to their aspirations. Back then, as a civil engineering undergraduate student seven years ago, I had no previous experience, but only had (and still have) an aspiration to become a roboticist to build prosthetics or exoskeletons in the future. Here was where Liz's magic master plan started. Throughout the three years I spent working on the purely passive arm training simulator towards my master's degree, I walked into this new field of mechanical engineering and learned so much from Liz, Prof. Randy Ewoldt, my excellent HDCL peers (Carrie, Chenzhang, Leo, Prateek, Maria, Nick, Alan, Matt, Cathy…). Starting from my PhD studies, once Liz believed I became better prepared, I was brought onboard to work on two complex electromechanical robotics projects: SEA-based robotic training simulators (my dissertation topic) and a self-balancing ballbot. These projects introduced me into the field of robotics, where I embarked on this fascinating journey. Now looking back, Liz has been constantly assessing my growth, deliberately selecting projects aligned with my passion, and pushing me out of the comfortable zone to become a more all-round engineer. I feel so fortunate and grateful for having Liz as my advisor over these years and she guides me through all these transitions to step closer to be the person I initially aspire to be. She might seem to only reveal part of her care in front of you, but she always gazes at your growth and well-being, and deep down, she considers and cares 200 % about you.

I would also like to thank Dr. Chris Zallek for his long-term support and guidance. He is not only our clinical collaborator, but more like a co-advisor and mentor to me over the past years.

Chris would always be my trustful source of clinical knowledge. He has a passionate but patient, informative but gentle mentoring style. He is always trying to explain things in a common language both clinicians and engineers can understand. Your attentive and considerate leadership style will continue to accompany and influence me in my future career. Also, I would like thank Prof. Mariana Kersh, Prof. João Ramos, and Prof. Manuel Hernandez for serving on my doctoral committee. Their generous support and invaluable feedback guide me to think more comprehensively and polish my dissertation into a better shape. I would also like to thank Prof. Tao Liu, Prof. Liangjing Yang, and their students at Zhejiang University (ZJU) for their generous hospitality and support for my clinical studies in China during the unpredictable COVID-19 pandemic. Finally, I would like to thank Kathy Smith, Katie Burke, Robbie Vermillion, and other department staff for their heartwarming and generous support throughout my graduate studies.

Next, I would like to thank the graduate and undergraduate peers in the HDCL. Thank you Yu Chen and Chenzhang Xiao for those countless days and nights we working together to learn and become better engineers, and more importantly for your precious friendship over these years and onwards. Thank you Leo Song for being PhD buddies for each other and having each other's back both in research and also in life. I'm honored and proud to work with you through all these projects and I wish you all the best in your next endeavor. Thank you Mahshid Mansouri for your unconditional support and friendship (both long-distance and in-person). My last study would not be possible without you. More importantly I really enjoyed and will remember the time when we debugged, traveled, and presented together. Thank you Kevin Gim for teaching me all those interesting things about robotics and for your friendship. I wish the best for you and your family. Tianyi (Tim) Han, I feel so fortunate to know, work, and develop sincere friendship with you both in the U.S. and in China. I wish you all the best for your upcoming PhD studies. I would also like

to thank other knowledgeable and supportive graduate members in the HDCL: Nick Thompson, Prateek Garag, Maxine He, Abdul Alkurdi, Nadja Marin, Keona Banks, Ezekiel Hsieh, and Yixiao Liu. I cannot thank enough for the things I learned from you and for the help you gave me. I would like to thank the numerous undergraduate students who helped me throughout my PhD projects: Ben Yang, Zeying Lang, Dmitry Ilchenko, Hongyi (Lance) Zhou, Youcheng (Sam) Zhang, Hanyu (Tim) Gan, Yiyue Feng, Haozhou Zeng, Aria Ruan, Annika Srinivasan, Amy Lang, and Zhongchun Yu. None of these projects would be possible without your dedicated efforts. I hope our paths will cross again in the future and wish you all the best in pursuing your aspirations.

I would like to thank all my friends around the world: Niaotao Jiao, Junyi Zhang, Zhaochen Xie, Lechen Yuan, Gaoran Sun, Yuanxu Li, Yuqi Zhang, Jiwei Cai, Ziyi Lian, Chengfang Duan, Ce Shi, Xiaotian Zhang, Mengchao Zhang, Hankun He. Old friends are like stars. Although you don't see them all the time, you know they are always there for you. Getting to know you all is one of the best things happened to me and this paragraph is for you.

Lastly, I would like to thank my family and cats for their continual support and unconditional love. Mom, Dad, Jiayue's parents and grandma, you always encourage me to follow my passion and respect my decisions. You value kindness and integrity more than success. Jiayue and I are so lucky to grow up in families like this. Jiayue, thank you for always believing in what I can do and being there for me in the last nine years. I can't wait to embark on the next stage of our life together. I thank my cats (Chester, Pudding, and Walnut) for their companionship and trust.

These projects were funded by the Jump Applied Research for Community Health through Engineering and Simulation (ARCHES) program and by the ZJU-UIUC Institute Research Program. I would like to thank all the healthcare practitioners I worked with throughout my entire PhD studies. I wish one day the technology/concept developed here could benefit you all.

TABLE OF CONTENTS

CHAPTER 1

INTRODUCTION

1.1 Common Muscle Behaviors Seen in Neurologic Exams

Abnormal muscle behaviors are important clinical manifestations of neurologic conditions [1–5]. For example, approximately 80% of cerebral palsy and multiple sclerosis patients have varying levels of muscle spasticity (an involuntary spend-dependent increase of muscle tone) [6]. During neurologic exams, clinicians usually perform manual assessments on patients, such as passive stretching of affected muscles and tapping the tendon, to elicit muscle responses [7]. These responses can be characterized by distinct muscle tone response patterns, given the difference in underlying pathological mechanisms.

Spasticity, hyperactive deep tendon reflex, and clonus are associated with neurologic conditions that affect partial or entire descending motor pathways, such as cerebral palsy, spinal cord injury, stroke, multiple sclerosis [2]. These conditions cause upper motor neuron (UMN) syndrome, interrupting the inhibition signal of the spinal reflex, so that the resulting muscle behaviors are known to have stretch speed-dependent and abnormal increase in motor activity. Specifically, when being passively (i.e., muscle is reflexed) stretched, the spastic muscle is marked by an abrupt involuntary increase of muscle tone then followed by a drop of muscle tone, where the tone will increase with higher stretch velocity [4]. This unique muscle response is referred as “catch-release behavior” or “clasp-knife behavior” of spasticity. Hyperactive deep tendon reflex is commonly found in patients with spasticity. When their tendons (such as at knee or ankle) were

tapped briskly (i.e., rapidly stretching of the tendon and muscle unit) by a medical reflex hammer, an exaggerated tendon response will be observed [8]. Eventually, a clonus (mostly commonly seen at knee or ankle) is an involuntary rhythmic muscle contraction with a characteristic frequency between 5-8 Hz, which can be triggered by rapid lengthening of the extensor or plantarflexor muscle of the joint [9].

On the other hand, tremor and rigidity (lead-pipe or cogwheel types) are found in patients with Parkinson's disease and these parkinsonian muscle behaviors are not stretch speed-dependent [10]. The exact mechanism of Parkinson's disease still remains unclear but relates to the loss of dopaminergic neurons in the substantia nigra [11]. Patients with lead-pipe rigidity exhibit a uniformly increased muscle tone throughout the range of motion (ROM) during passive stretch test [12], whereas those with cogwheel rigidity will experience similar involuntary muscle tone but switching on and off at around 6-9 Hz [13].

1.2 Why Do We Need Medical Task Trainers?

Clinicians need to rely on haptic experiential knowledge to diagnose the underlying neurologic conditions that are associated with the triggered abnormal muscle behavior [7]. Although more advanced non-invasive assessment techniques are emerging based on wearable position, force, electromyography sensors (such as [14,15]), manual physical assessment is still standard in the clinical setting. Therefore, it is imperative to afford new clinicians, healthcare learners, students, residents, or fellows more exposure to the haptic feeling of common abnormal behaviors during training and to practice their ability to trigger clinical manifestations of neurologic conditions and distinguish the severity of the condition [16–19].

Traditional clinical training of motor skill assessment is carried out on live subjects [20]. To train the students, instructors often bring in a small number of real practice patients who have stable chronic conditions or recruit "standardized patients" who are healthy individuals trained to portray a patient's conditions[1] [21] (Fig. 1.1, left). According to a survey from the Association of American Medical Colleges in 2011, almost 95 % of medical schools are using standardized patients in their curriculums [22]. Though this training method has been widely adopted, learners still suffer from a) incomplete training experience when no practice patients available to present or mimic rare clinical cases [23], b) a lack of practice opportunities due to the limited number of practice patients [24], and c) inconsistent training outcomes given the variability of the practice patients[25]. This training challenge calls for more accessible and consistent ways to provide training opportunities for learners that replace or reduce the need for practice patients and one promising approach is the deployment of medical education task trainers (Fig. 1.1, right).

Fig. 1.1: (Left) A conventional training scenario where an instructor demonstrates the assessment technique on a practice patient for the class. (Right) A simulator-based training scenario where an instructor demonstrates the technique to assess spasticity in the biceps on our previously developed task trainer [53,56].

In this dissertation, the terms "task trainers" and "training simulators" are used interchangeably. To understand what medical training simulators are, we refer to the generic

[1] The term "standardized patient" are defined differently (sometimes also refers to real patients with stable conditions) and used interchangeably with other terms such as "patient actor" or "simulated patient" in the literature [149]. In this dissertation, we refer both real patients and standardized patients as practice patients.

definition of simulation, which is “an imitation of some real thing, state of affairs, or process for the practice of skills, problem solving, and judgement” [21]. The idea of learning or training through simulators was initiated in the nonmedical fields such as aviation [26], aerospace [27], and driving [28] throughout the 20th century. One of the first attempts of deploying a training simulator in the medical field was “Harvey”, a cardiology patient simulator in 1968 [29]. Since then, the global medical simulation market size has grown to around USD $1.72 billion in 2020 [30], and the use of task training simulators has become an increasingly important part of the learning experience for medical student, residents, fellows, nursing staff, physical therapists,, and other healthcare professionals [20,31,32].

Training simulators render easily accessible, safe, consistent, and scalable training environment for students, allowing learners to gain hands-on experience without the presence of human patients [20]. Conventionally, sometimes it is impossible for students to be trained on some rare complications simply because there is no suitable human practice patient available [33]. With the training simulators, the students will have immediate access to the training opportunities with a wide variety of clinical scenarios, rather than waiting for actual patients to present with the condition [34]. During the training process, although the current training technique referred as “see one, do one, teach one” is generally successful, there is still risk to the patient due to novice technique and mistakes. On the other hand, medical simulators allow trainees to practice and master the basic skills before engaging with a real patient [35]. Furthermore, the traditional instructor-centric training style is difficult to scale to a larger cohort due to the instructor’s limited energy and availability, and also might deliver biased learning experiences given the instructor’s personal work habit and way of teaching. Therefore, wide-spread implementation of simulators could improve technique consistency and standardization across different institutions and different methods of

teaching, and establish a distributed (as opposed to centralized around the instructor), self-service type of training environment for the students, which releases the instructor from busy logistics and allows them to focus on teaching and influencing a larger audience of students [36]. Eventually, in the current context of the global COVID-19 pandemic since 2020, the awareness of social distancing and reduction in clinician-to-patient interaction further imposes difficulty on the traditional training methods which involve close, in-personal interaction and crowd gathering. In this case, the decentralized training nature of medical simulators becomes especially valuable and represents a promising alternative solution for clinician learners to continue practicing and honing their technique without close interaction with human patients, rendering a safe education environment for both trainees and patients [37].

1.3 Medical Task Trainers are Everywhere, but Why so Rare for Neurologic Exams?

When speaking of task trainers or training simulators, for most people, it is easy to mentally picture those have been widely adopted in current medical education of surgical and anatomical procedures such as IV insertion, endoscopic procedure, and endovascular procedure [20]. These devices range from as simple as a passive mannequin arm covered with artificial skin [38], more sophisticated full-body articulated mannequin [39], as well as high-fidelity, full-procedure training station that incorporates visual, tactile, audio feedback [40] (Fig. 1.2).

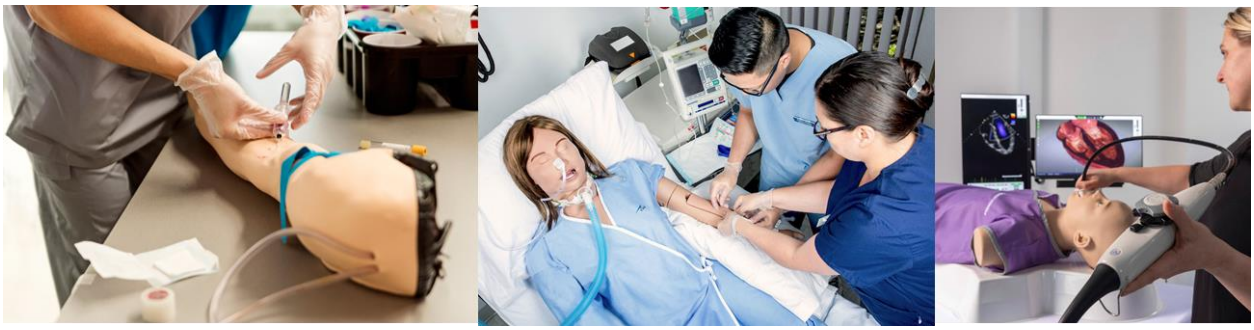

Fig. 1.2: Various commercially available medical task trainers for surgical and anatomical tasks. (A) A standalone mannequin arm for insertion procedure training [38]. (B) A full-body mannequin for nursing scenario training [39]. (C) Emergency care patient simulator for ultrasound imaging, for echocardiography training [40].

From an engineering point of view, although significant amount of product development efforts were put into creating relatively realistic artificial skin and virtual reality environments (although still not perfect) [41], the main technical challenge solved through the development of these task trainers centered around kinematics-related problems [42], such as path planning for technique instruction [43] and user motion tracking for performance feedback [44]. On the other hand, these task trainers usually do not directly deal with the force control[2] problem. For some training scenarios such as stitching, palpation, or endoscopy technique, the task trainer is required

Fig. 1.3: Commercial haptic devices used together with task trainers to kinesthetic haptic feedback. (Left) Phantom Omni from 3D System [45]. (Right) Novint Falcon from Novint Technology, Inc [46].

[2] The term "force control" and "torque control" are often interchangeable in this dissertation, regardless of linear or rotary actuators.

to render kinesthetic haptic feedback to the user to convey sensation information about the texture of and/or the interaction with the virtual environment (e.g., deforming, grasping, or sometimes damaging the virtual tissues). Typically in these cases, the task trainer would rely on using third-party reliable haptic devices as such Phantom series (3D Systems) [45] and Novint Falcon (Novint Technology, Inc.) [46] (Fig. 1.3). In other words, the force control capability is provided via an external haptic device and not integrated in the mannequin. Although these task trainers for surgical and anatomical procedure training were proven to be very successful in kinematic-based procedure training scenarios and received increasing acceptance around the world [21], the existing design knowledge cannot be directly transferred to develop medical training simulators in neurology and physical therapy due to the lack of integrated force control capability, so new designs need to be proposed.

To infer the underlying neurologic conditions from muscle tone or to manage patient condition, neurologic exams require the clinician to move the patient's limb through the range of motion, which stretches the flexor and extensor muscles at the joint being examined. Based on the characteristics and severity of the elicited muscle tone, a diagnosis will be made. In order to replicate this assessment scenario, the task trainer design not only needs to have the appearance of a human limb with articulated joint(s) for students to perform the passive stretch test, but also should incorporate the functionality of creating kinesthetic haptic feedback at the joint(s) of interest to render the muscle behaviors (e.g., resistance, rhythmic contractions). Therefore, the task trainer shares similar operation and design principles as a haptic device [47]: (a) admit and measure the user's input motion (e.g., moving the limb to stretch the muscle) or stimulus (e.g., tendon tap), (b) acts as an impedance source to compute corresponding muscle tone based on the internal simulation model, and (c) eventually delivers the simulated muscle tone back to the user. This

workflow requires the task trainer to either take a form of two adjacent human-sized mechanical limbs (in upper or lower body) that can be moved relative to each other by the user, with integrated force/torque control capability via active/passive actuators at the connecting joint, similar to an arm or leg prosthesis; or alternatively an exoskeleton-type emulator device that is worn by a healthy individual and modulates the joint torque to convert the wearer to a mock patient. Therefore, given these design requirements, the mechatronic design, sensing, and human-robot interaction control challenges for these task trainers are more aligned with those of prosthetics and exoskeletons, unlike traditional passive mannequin-based training simulators.

1.4 Existing Research Task Trainers for Neurologic Exams

Considering the additional technical challenge on force control needs to be addressed, the development of task trainers for neurology and physical therapy are far less mature compared to those discussed in the previous section. Only a few designs have been proposed in the past [48–56]) (Fig. 1.4). Due to the inclusion of moving mechanisms and actuators, these devices look more like robots than traditional passive mannequins, so in this dissertation, we will refer these devices as *robotic task trainers* or *robotic training simulators* to highlight their robotic nature.

These previous medical robotic task trainers can be categorized as *prosthetics-type* and *exoskeleton-type* configurations. The prosthetics-type configuration designs [48,49,52–54,56] usually took the form of human-sized artificial robotic limbs (lower extremity [54] or upper extremity [52]) with an actuated joint (active [48,49] or passive [53]) that mimic a patient's joint affected by pathological muscle behaviors due to underlying neurologic conditions (Fig. 1.4, A-F). The exoskeleton-type configuration designs [51,55] operated similar to wearable exoskeletons. But rather than providing assistance to the wearer, these devices imposed resistive torque to the

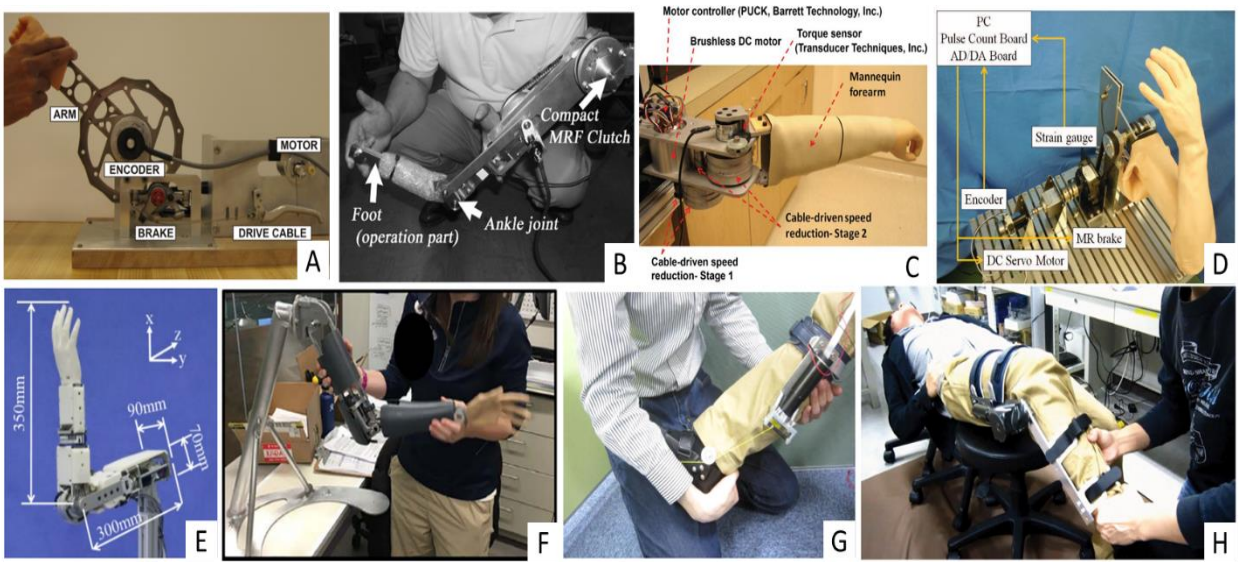

Fig. 1.4: Existing medical education task trainers using different actuation technologies for mimicking various abnormal muscle behaviors: (A) Motor-controlled bike brake for elbow spasticity [49]. (B) Direct-drive motor and magnetorheological fluid (MRF) clutch to mimic ankle spasticity and clonus [54]. (C) Quasi direct-drive motor for elbow spasticity [48]. (D) Geared motor with MRF brake for elbow rigidity/spasticity [52]. (E) Geared motor and nonlinear springs for elbow spasticity/rigidity [50]. (F) Passive hydraulic damper and linkage for elbow spasticity [53,56]. Wearable exoskeleton with geared motor for (G) ankle clonus and spasticity [55] and (H) knee spasticity, rigidity, contracture, and ankylosis [51].

wearer's joint (knee [51] or ankle [55]) on top of the healthy muscle tone to convert a healthy individual and emulate a "mock patient" with certain abnormal muscle behavior (Fig. 1.4, G and H).

A. Simulation of Target Behaviors

Existing trainers mainly targeted mimicking common abnormal muscle behaviors frequently encountered by neurologists and physical therapists such as spasticity [48–56], rigidity (cogwheel and lead-pipe) [50–52,57], and clonus [54,55,58]. The simulated muscle behaviors were created through the modeling of the neuromuscular diseases, but in general, quantitative documentation of the kinematic and kinetic patterns of these abnormal muscle behaviors are lacking from the literature. Therefore, previous researchers have been working around this problem mainly via three approaches: a) first-hand clinical data collection [48], b) expert tuning [52], or c) a

combination of them [54]. For example, Park et al. used a custom wearable measurement device to measure the kinematic and kinetic relationship of nine child subjects with cerebral palsy at the elbow joint and selected four subjects with characteristic spastic muscle tone profiles to mathematically model the elbow spasticity for the development of their arm task trainer [48]. On the other hand, Takhashi et al. invited two experienced physical therapists and asked one therapist to pretend to be a spasticity or rigidity patient by intentionally coactivating the muscle to create resistive muscle tone at the elbow, while the other therapist performed the passive stretch test on the first therapist. Motion capture markers and a load cell were utilized to measure the elbow joint angle and muscle tone during the assessment and these quantified data were later used to program their arm task trainer [52]. Eventually, Kikuchi et al. developed a leg task trainer to replicate ankle clonus and they determined the control parameters such as clonus oscillation frequency, muscle tone amplitude based on previous quantification studies in the literature as well as the fine-tuning by two experienced physical therapists [54]. Although these heuristic detours were reasonable and still very practical for simulator development, the lack of quantitative understanding of the abnormal muscle behaviors poses fundamental challenge for task trainer designers and prevents them from knowing the underlying neuromuscular mechanism behind these behaviors as well as developing mathematical models to simulate these behaviors. This grand challenge requires continuous collective efforts from engineering, neuroscience, physiology, clinical and medical communities in terms of recording, interpreting, and reporting quantitative observations. The development of task trainers with higher fidelity has to be built upon more fundamental understanding of the neuromuscular pathology.

B. Actuation and Control Strategy

Previous robotic task trainer designs adopted various actuation strategies, such as direct

drive [54], quasi-direct drive [48], magnetorheological fluid (MRF) brake/clutch [52,54], or electromechanical brake [49]; yet, there has been no consensus on the optimal actuation solution. In general, robotic designs based on direct and quasi-direct drive electric motors benefit from their transparent force control capability, so the force control algorithm can be greatly simplified thanks to the minimal unmodeled dynamics (e.g., stiction, viscous friction, hysteresis), low backlash, and high drivetrain stiffness [59]. Furthermore, if additional mechanical design considerations are given to reduce friction loss in the transmission and lower the inertia of the motor output link, the measured current (i) in the motor winding together with the motor torque constant (K_T) could be used as a simple, reliable, and robust way to estimate motor output torque at the end effector, i.e., $\tau_{output} = K_T\, i$. This approximated end effector torque information based on current measurement in the motor winding enables open-loop torque control[3] to achieve good torque accuracy without the use of an external force/torque (F/T) sensor [60], which is both very costly and fragile under collision. Finally, low reflected inertia[4] that comes with low gear ratio significantly reduce the peak shock force at impact, reducing not only the risk of hurting the user, but also the risk of damaging the robot drivetrain upon unanticipated collisions. Given these advantages, direct and quasi-direct drive motors are widely used in dynamic mobile robots [60,61], haptic device [62], teleoperation [63], etc. However, in order to implement this actuation strategy to the task trainer application, a few concerns need to be mentioned. Unlike the delicate haptic device operates at the fingertip level, to mimic severe spastic or rigid muscle, these task trainer's continuous torque requirement could be more than 20 Nm. With no or low gear reduction, when outputting large torque frequently or

[3] Torque control is in the outer loop and current control in the inner loop. There is no external F/T sensor, so it is open-loop torque control. With the current sensor in the motor driver, it is closed-loop current control in the motor winding.

[4] Reflected inertia is also called apparent inertia and refers to the motor rotor inertia amplified by the square of the gear ratio (N), i.e., $I_{reflected}=I_{rotor}N^2$. The reflected inertia can be perceived by manually turning the motor shaft to backdrive the motor.

over an extended period, the high operation current and heat dissipation issues of direct or quasi-direct drive motors might compromise user safety during human-robot interaction. In addition, a low gear ratio will force the designers to use large motors, which might result in bulky and nonergonomic joint designs having an adverse effect on the appearance realism. Furthermore, the output link of the task trainer (e.g., the forearm and the foot) needs to match the anthropometric dimensions and contours, so it cannot be as primitive as a lightweight carbon fiber tube and will inevitably have non-negligible mass and inertia. Therefore, due to the gravitational and inertia effects of the output link, there would be torque discrepancy at the actuator output and at the end effector, which likely degrades the effectiveness of open-loop current control. Possibly for this reason, several previous task trainers that utilized direct drive [54] or quasi-direct drive [48] motors still deployed a F/T sensor in their end effectors to use feedback control to mask the link dynamics, resulting in much more expensive and less robust designs.

Active brakes (e.g., electromechanical brakes or MRF brakes) represent another previously attempted actuation approach. The design concept of using brakes to render muscle resistance is natural and intuitive. An electromechanical brake design usually used an electric motor to generate a clamping force to produce a friction force on the surface of braking pads [64]. One example of this design concept is Grow et al.'s work where they used an electric motor to control the clamping timing and force of an off-the-shelf bike disc brake to mimic the muscle response of a spastic patient [49]. A magnetorheological fluid (MRF) brake is another promising option to generate a responsive and smooth haptic feeling. MRF is a smart material consisting of fine, magnetizable particles (typically ferrous particles) whose rheological properties (e.g., viscosity) can be modulated through the application of a magnetic field [65]. A MRF brake generates resistive braking torque through the viscous shear force between the MRF and the brake rotor. Fluid viscosity can be modulated

rapidly (time constant ~ 20 ms [54]) by actively changing the operation current (i.e., altering the magnetic field strength) [66]. However, there are a few obstacles preventing the MRF technology from being widely adopted. First of all, although several custom MRF brake research prototypes exist and it is a fast evolving research direction in the academia [67], the off-the-shelf choice of MRF products is quite limited. Most are mainly used in the automotive field such as active suspension and steering haptic feedback [68], so their sizes are often too bulky to be integrated in medical or robotic applications. Second, although these controllable brakes could modulate the resistance, they have to be used in parallel with powered actuators to mimic active symptoms (e.g., clonus, tremor). It is also a control challenge to precisely control the braking force (for both electromechanical and MRF brakes) to render the desired haptic feedback to the user due to the nonlinear and hysteresis effects in the brake system [69]. Therefore, previous task trainers operated either on closed-loop torque feedback control via a F/T sensor in the end effector (very costly) [70] or simply open-loop torque control by commanding the current in motor and MRF brake (inferior torque control fidelity) [24]. Regardless of all these limitations, as miniature MRF brakes become commercially available in the future, this technology potentially represents a very promising approach to render high resistance in a more smooth, robust, and safe fashion compared to using a highly-geared electric motor.

C. Potential Approaches and Solutions

To the author's knowledge, currently none of these previous research prototype simulators discussed in this section were commercialized nor adopted by medical training institutions beyond those authors' home institutions, possibly due to device complexity, maintenance, cost, or simulation fidelity. To address these practical limitations, in 2014-2018, our research group developed a passive (i.e., without active actuator and power supply) training simulator prototype to

mimic elbow biceps spasticity with purely mechanical mechanisms (Fig. 1.5) [53,56]. The spastic muscle tone was simulated using a custom hydraulic damper with selectable viscous effect. For different severity levels of spasticity, five pairs of orifices were fabricated on the piston head and only one pair was exposed, while the rest were blocked by a cover plate. By varying the orifice size in operation, different viscous effects could be selected based on the severity of the simulated patient. A Scotch-Yoke linkage system was used to convert the damper's linear resistance to a rotary resistance at the elbow joint. The linkage system also determined at which joint angle the damper would start to engage, mimicking the spastic catch angle (i.e., muscle resistance only kicks in after a certain angular position) and replicated the catch-release behavior via a varying moment arm. Due to the lack of quantitative data in the literature, the simulation aspects were designed iteratively driven by clinician feedback. Ideally, the development of a training simulator requires (a) establishing a database that documents the kinematic and kinetic data associated with patients at varied severity, and (b) building a mathematical model that relates the kinematic inputs with the spastic muscle kinetic response at varied severities. The current absence of both pose difficulty on systematically being able to design and tune a simulator towards realistic muscle behaviors. Therefore, Song et al. developed a wearable measurement device to mount on two adjacent limbs (one moving and the other stationary during the stretch test) (see Fig. 5.1 in Chapter 5) [71]. Both moving and stationary modules contained an inertial measurement unit to compute the joint kinematics, and the moving module also had a force sensor to measure the applied load by the assessor. Through our past [72] and ongoing efforts [73] (further discussed in Chapter 5) in clinical quantification studies, we are trying to obtain additional quantitative measures of spasticity and rigidity from more patients for future development and tuning of the simulator.

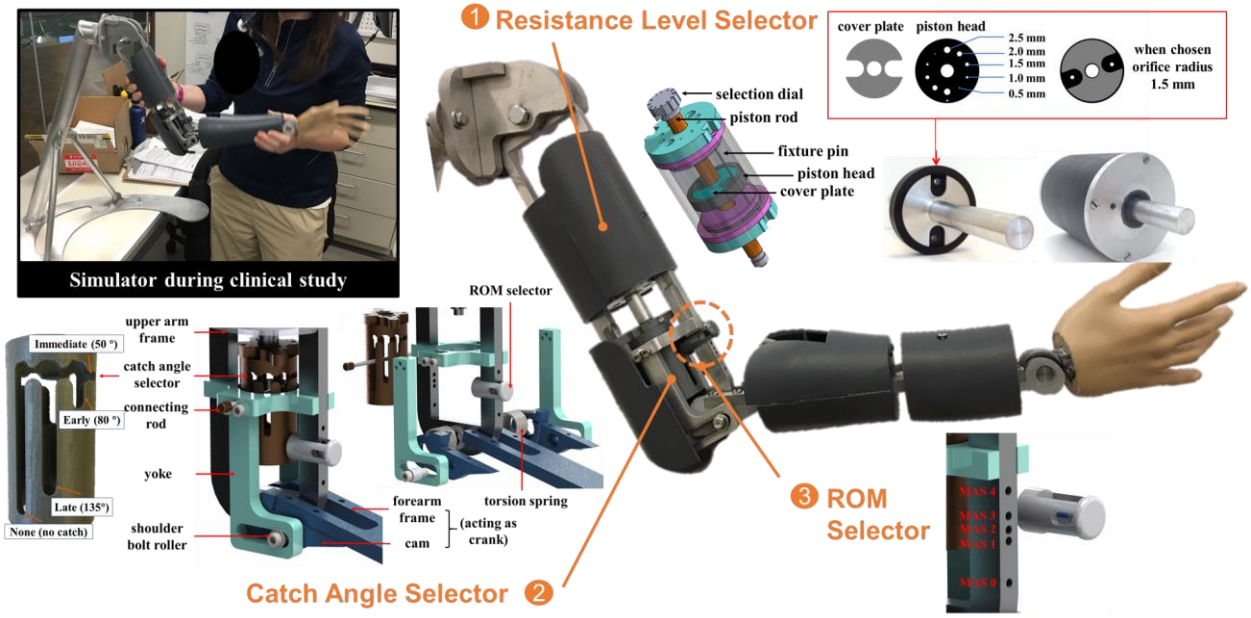

Fig. 1.5: Passive hydraulic training simulator with three mechanical design features highlighted [53,56].

This passive design approach has advantages and disadvantages. First, this simulator requires no external power to operate, so it can be easily transported and deployed in various locations in a training room. Second, the simulator is affordable and compact, consisting of only mechanical components (e.g., linkage, hydraulic device, etc.) without any expensive electrical parts (e.g., sensor, electric motor, hardware controller). This simulator requires no complex control scheme (simply open-loop mechanical response) and is inherently safe due to the passive nature of its actuator (i.e., hydraulic shock absorber), so there is no instability issue during human-robot interaction. On the other hand, with lack of real-time sensing and feedback control, our simulator is unable to generate complex muscle resistance profiles, unlike other active-controlled simulators (e.g., [24,48,50]). The simulator can only provide five distinct simulations to replicate specific severity levels (MAS 0-4), but it is not reprogrammable. In order to adjust simulation performance, new mechanical components would need to be designed, manufactured, tested, and assembled. Additionally, the specific simulator was designed solely to simulate biceps spasticity. To simulate

a different neurologic condition such as rigidity, a new hardware system based on a completely different physical principle would need to be designed and little can be inherited from this prototype. In contrast, electromechanical designs could be easily reprogrammed to simulation different severity levels on the fly and other types of abnormal muscle behaviors without hardware changes (e.g., rigidity and clonus).

Reviewing the pros and cons of previous active and passive design approaches, it is desirable to remove the F/T sensor from the active design to lower the device cost but to still maintain the high-fidelity force control capability to track complex muscle tone profiles. At the same time, we aimed to keep the intrinsic safety and compactness of the passive design. Therefore, the concept of a series elastic actuator was explored to develop a high-performance, cost-effective, and safe training simulator that is educationally useful and economically viable to be integrated into the curriculum of the training institutions.

1.5 Review of Series Elastic Actuator

The series elastic actuator (SEA) has been widely used in the robotics community, e.g., mobile robots [74,75], humanoids [76], quadruped robots [77], prosthetics [78], walking bipedal robots [79], industrial robots [80] (Fig. 1.6), but its use has been absent in the field of robotic medical task trainers. The concept of a SEA was first introduced in the 1990s-2000s via including series elasticity in the drivetrain to enhance force control capability of actuators with high torque density but also high impedance[5] (e.g., hydraulic cylinders, highly-geared electric motors) [81,82]. "Stiffer is better" is the design philosophy for position control tasks [83], where the external force

[5] The impedance of an actuator is the additional force created at the output due to load motion and typically increases with the frequency of load motion [82], e.g., the seal friction in hydraulic actuators, or stiction and viscous friction in the gearbox of geared electric motors.

should result in minimal structural deformation and end-effector position deviation, therefore the use of high-impedance actuators is favored. In contrast, force control tasks emphasize force transparency, i.e., the actuator can actively deliver the accurate force/torque via the drivetrain to the environment, and at the same time, the actuator and drivetrain can be effortlessly backdriven by the interaction with environment. In other words, the actuator and drivetrain are transparent to the flow of force and will not hinder how force flows in both directions [84]. Therefore, low-impedance actuators (e.g., direct- or quasi-direct drive motors, biological muscles) are ideal for force-controlled applications, where the force/torque output can be accurately regulated with simple feedforward control and the load motion disturbance would cause minimal resistive force in the actuation system. However, the lack of compact, low-impedance but high torque density actuators still remains as one of the major bottlenecks to robotics research. Until these ideal force-source actuators (like biological muscles) become available, currently there are three main workarounds on actuation strategy to build highly dynamic, force-controlled robots to work in unstructured environments: a) hydraulic cylinders with servo valves (e.g., in Boston Dynamics Altas [85]), b) pancake torque motors with low gear ratio (e.g., in MIT Cheetah robots [59,86]), and c) series elastic actuators (e.g., ETH ANYmal [77]).

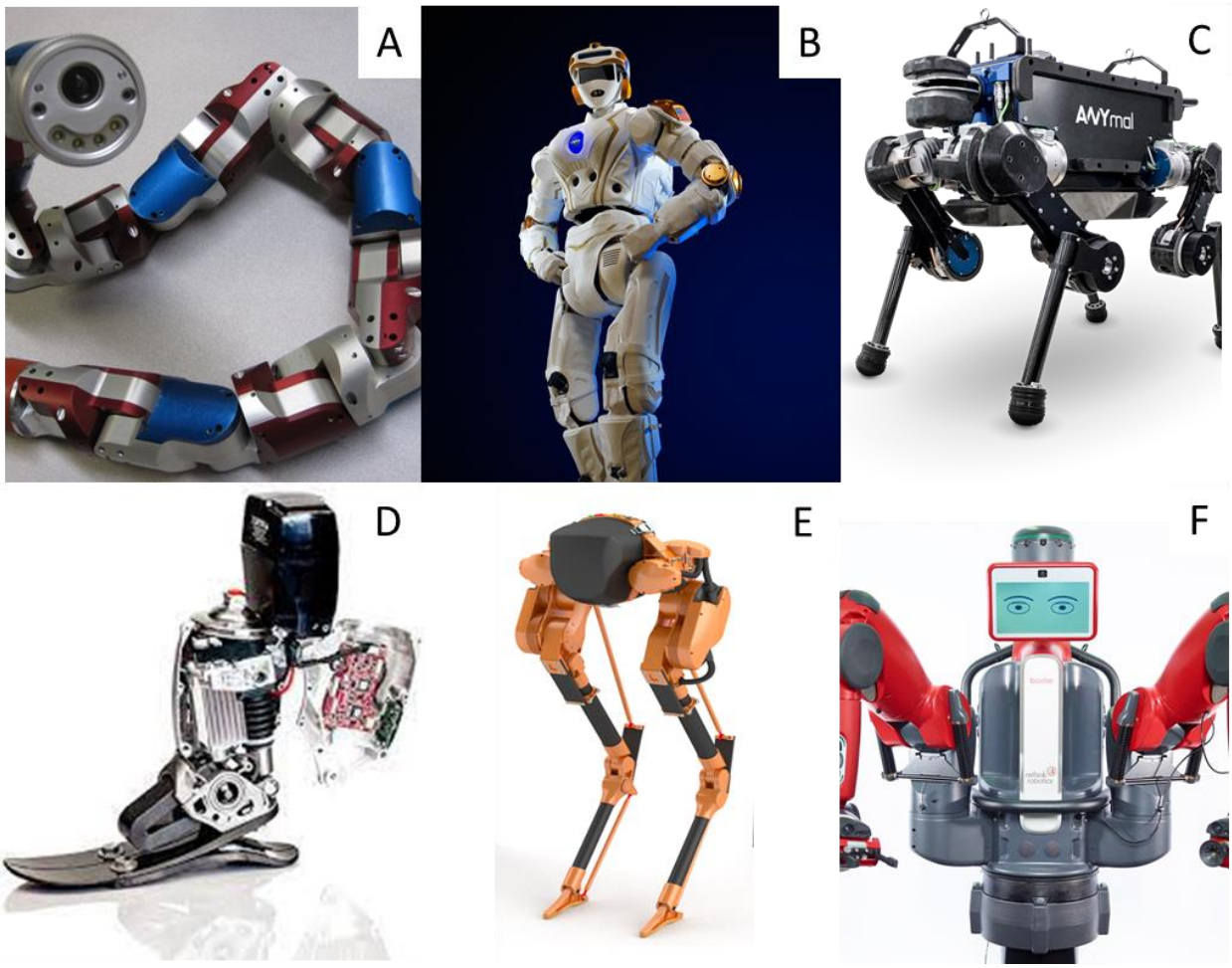

Fig. 1.6: Various well-known robots designed based on SEA strategy. (A) CMU snake robot [74]. (B) NASA Valkyrie humanoid robot [76]. (C) ETH Zurich ANYmal quadruped robot [77]. (D) MIT ankle prosthesis [78]. (E) Agility Robotics Cassie robot [79]. (E) Rethink Robotics Baxter robot [80].

SEA design features several hardware and control benefits. By intentionally placing a compliant element (usually a linear or torsional mechanical spring) in series with a high-impedance actuator, the stiffness of the drivetrain is significantly reduced (Fig. 1.7). Given the intuitive criteria proposed by Whitney for determining force control stability [87],

$$0 < TGK < 1 \tag{1.1}$$

where T is the sampling interval, G is the feedback controller gain, and K is the system interaction stiffness (including both the actuator and the environment). If the sampling interval remains constant, two straightforward, qualitative takeaways interpreted from (1.1) are that a) force control

stability can be more easily satisfied if the actuator is interacting with a less stiff environment or the actuator itself is more compliant [88], and b) if K is decreased by reducing the actuator stiffness (i.e., SEA design), then the controller gain (G) can be further increased and still satisfy (1.1) [89,90]. Higher feedback controller gain will lead to more responsive tracking performance, less steady-state error, and better disturbance rejection. Therefore, a SEA achieves better force control fidelity and stability by essentially trading off physical system stiffness for higher feedback control gain in software. High feedback gain effectively addresses the unmodeled parasitic phenomenon (e.g., stiction, viscous friction) in the high-impedance actuators, which are typically very difficult to be removed using feedforward control. Furthermore, the deflection of the series elastic member (e.g., spring deflection) could be used to estimate the output force via Hooke's Law so that there is no need for an expensive rigid load cell. For this reason, a SEA converts a force control problem into a position control problem by regulating the end position of the series spring. Thus, in order to achieve a desired force output, instead of precisely commanding the motor torque and delicately pre-compensating the gear train loss, we can simply focus on regulating the motor shaft position and output link position using encoder-based feedback [91]. Compared to force feedback control, position feedback control is much easier, more robust, and can be achieved with the use of low-cost motors and drivetrain components. Finally, the series spring decouples the output link from the actuator, so that the reflected inertia of the actuator is physically isolated and only the link inertia is perceived by the user. As a result, the impedance of a SEA can be very small at low frequencies given the low reflected inertia and good backdrivability (achieved via high-gain feedback control). At collisions (i.e., high-frequency impact), the series spring will serve as a mechanical buffer between the actuator and the environment, so the high-frequency impedance of a SEA approaches the physical spring stiffness [81]. Therefore, the SEA strategy is a promising

option to develop low-impedance, high torque density, cost-effective, and compact actuators, which are ideally for force control tasks.

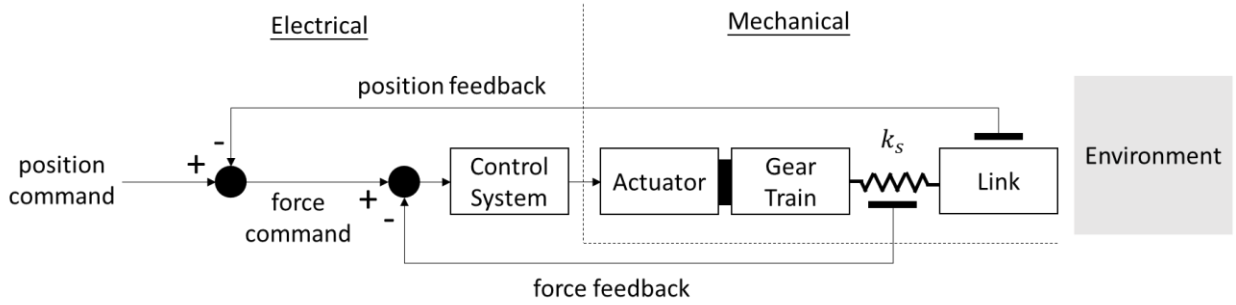

Fig. 1.7: Conceptual schematic of a SEA based on an electric motor, adapted from [61].

Although the lowered drivetrain stiffness in a SEA brings above advantages, it also comes with drawbacks. First, the intentional introduction of a series elastic element will add additional compliance between the actuator (with transmission) and the output link (Fig. 1.7). For position feedback control, the controller has to reduce the feedback gain to avoid exciting the extra dynamics caused by the drivetrain compliance between the actuator and the output link position sensor, essentially compromising its tracking performance to ensure stability. This is known as non-collocated actuator and sensor configuration and will have a detrimental effect on feedback control performance, i.e., the increase of controller gain will easily cause the system to be unstable, meanwhile low gain results in sluggish system response [92]. Therefore, a design trade-off in SEA mechanisms involves sacrificing position control bandwidth and stability for better force control stability. Second, the lower drivetrain stiffness leads to a lower natural frequency of the mechanical system, which can be used to approximate the system open-loop bandwidth[6] and ultimately limits the close-loop control bandwidth [59,93]. Thus, the lower control bandwidth is usually considered

[6] Bandwidth is defined to be the maximum frequency at which the output of a system will track an input sinusoid in a satisfactory manner. The bandwidth is the frequency at which the output is attenuated to a factor of 0.707 times the command [150].

a downside of using a SEA. However, given the relatively low output bandwidth requirement of a manual technique task trainers in neurologic exams (i.e., < 8 Hz), this inherent drawback of SEAs would not be a limitation. Also in our application, since the output link is always held and moved by the user, the robotic task trainer only needs to render haptic feedback via force control, so the SEA's inferior position control performance can also be avoided. By deploying a SEA system in our task trainers, a relatively high gear ratio allows a compact motor with reasonable operation current to be used, while ensuring sufficiently high torque density. A series spring serves as a compliant and cost-effective torque sensor that can accurately measure interaction joint torque between the user and robot. Thus, a SEA strategy is particularly suitable and practical for developing high-fidelity torque control and cost-effective robotic task trainers.

1.6 Dissertation Outline

In the first study (Chapter 2) [7], we present the design, modeling, control, and evaluation of an ankle-foot task trainer to replicate the behavior of ankle clonus. The foot-ankle assembly had two degrees of freedom and a realistic foot shroud. Haptic feedback force was generated from a series elastic actuator design with a cascaded PI feedback control architecture. Series spring stiffness was determined based on the dynamic modeling and control bandwidth requirement. Evaluation tests involved benchtop experiments and a validation study with experienced clinicians.

[7]The majority of this chapter was published in [58]: Pei, Y., Han, T., Zallek, C.M., Liu, T., Yang, L. and Hsiao-Wecksler, E.T., 2021. Design and clinical validation of a robotic ankle-foot simulator with series elastic actuator for ankle clonus assessment training. IEEE Robotics and Automation Letters, 6(2), pp.3793-3800. https://doi.org/10.1109/LRA.2021.3065242. New contributions are some further clinical study details in Section 2.3B.

In the second study (Chapter 3)[8], we continued to utilize the SEA-based ankle-foot trainer's torque control capability and expand its functionality to also simulate the deep tendon reflex response of the Achilles tendon when an external tap is given by the trainee, via incorporating a new artificial tendon structure and proposing a reflex response model. A series of simulation, benchtop, and clinical evaluations were conducted to validate our design.

In the third study (Chapter 4), we used an existing SEA-based arm task trainer that had been constructed by our group [57]. This trainer was programmed to mimic three different common abnormal muscle behaviors, i.e., spasticity, lead-pipe rigidity, and cogwheel rigidity. Mathematical modeling of these behaviors was proposed and used to compute reference joint torque based on trainee's input kinematics. A control scheme consisting of feedback, feedforward, and disturbance observer controller was designed and implemented to deliver the accurate torque feedback to the trainee. The arm trainer then was validated through benchtop and clinical evaluations.

In a side data collection study (Chapter 5), we aimed to conduct a cross-sectional study targeting up to 110 test participants to build a quantitative database on measured elbow kinematic and kinetic behaviors, as well as muscle activation, in patients with spasticity, lead-pipe rigidity, and cogwheel rigidity across severities and healthy controls during passive stretch tests. However, data collection has been delayed due to the COVID-19 pandemic, and so far, we have collected data from ten spasticity patients. This currently available dataset will be used to verify sensor setup and experimental protocol, as well as to identify appropriate data analysis methods in order to

[8] Part of this chapter was published in [151]: Pei, Y., Zallek, C.M., and Hsiao-Wecksler, E.T., 2022. Control Design and Preliminary Evaluation of a Medical Education Simulator for Ankle Tendon Reflex Assessment Training, Proceedings of the 2022 Design of Medical Devices Conference. Minneapolis, MN, USA. April 11–14, 2022. V001T06A007 (5 pages). ASME. https://doi.org/10.1115/DMD2022-1072. New contributions are the mechanical design details, as well as benchtop and clinical validation testing results.

facilitate future test sessions and data processing. The preliminary data analysis provided a guideline for programming the spasticity behavior in our arm trainer discussed in Chapter 4.

Chapter 6 summarizes the works presented in this dissertation, discusses lessons learned, and makes suggestions for future research directions.

CHAPTER 2

DESIGN AND VALIDATION OF A ROBOTIC ANKLE-FOOT TASK TRAINER FOR ANKLE CLONUS ASSESSMENT

Abstract

To fulfill the need for reliable and consistent medical training of the neurologic examination technique to assess ankle clonus, a series elastic actuator (SEA) based haptic training simulator was proposed and developed. The simulator's mechanism (a hybrid of belt and linkage drive) and controller (impedance control) were designed to render a realistic and safe training environment. Benchtop tests demonstrated that the prototype simulator was able to accurately estimate the interaction torque from the trainee (RMSE of 0.2 Nm) and closely track a chirp torque command up to 10 Hz (RMSE of < 0.22 Nm). The high-level impedance controller could switch between different clinically encountered states (i.e., no clonus, unsustained clonus, and sustained clonus) based on trainee's assessment technique. The simulator was evaluated by a group of 17 experienced physicians and physical therapists. Subjects were instructed to induce sustained clonus using their normal technique. The simulator was assessed in two common clinical positions (seated and supine). Subjects scored simulation realism on a variety of control features. To expedite controller design iteration, feedback from Day 1 was used to modify simulation parameters prior to testing on Day 2 with a new subject group. On average, all subjects could successfully trigger a sustained clonus response within 4-5 attempts in the first position and 2-3 in

the second. Feedback on the fidelity of simulation realism improved between Day 1 and Day 2. Results suggest that this SEA-based simulator could be a viable training tool for healthcare trainees learning to assess ankle clonus.

2.1 Introduction

A. Ankle Clonus

Clonus is defined as involuntary and rhythmic muscle contractions caused by lesions in the upper motor neuron pathways [94–98]. Although clonus has been reported in muscle groups at other joints, it is most commonly tested and observed at the ankle joint [99]. Ankle clonus can be elicited during a neurologic examination by rapidly dorsiflexing (DF) the ankle and maintaining a stretched state of the ankle plantarflexor muscles, as a result of sudden peripheral inputs activating the hyperactive stretch reflex [94,100–103]. Ankle clonus response is a rhythmic oscillation (or "beating") of the foot against an external load with a characteristic frequency between 5-8 Hz [94,104].

A patient is diagnosed with ankle clonus if the clinician is able to induce a "sustained clonus" response, i.e., five or more consecutive beats. Successful triggering of ankle clonus requires mastery of the following technique [7]: (a) correct positioning of the examining hand on the foot (i.e., evenly supporting on the plantar metatarsal area or grasping both lateral and medial aspects of the forefoot); (b) minimize ankle inversion (i.e., the foot should be in neutral or eversion); (c) provide a rapid dorsiflexion to trigger a stretch reflex (> 200 °/s); and (d) maintain constant applied torque on the dorsal surface of the forefoot (> 3 Nm). Current medical textbooks often only presented qualitative descriptions of this technique with the absence of numerical values, so the numbers in the parentheses were extracted by the authors from the few available clonus quantification studies or previous attempts on simulating ankle clonus [54,55,100,105,106]. These

numerical values were iterated based on clinical advice (Table 2.1).

B. State of the Art in Training Simulators for Ankle Clonus

As far as the authors were aware, only two devices exist that attempted to recreate ankle clonus for clinicians to train [54,55], and no commercially available product exists yet. Kikuchi et al. developed an electromechanical leg-shaped device that used a DC direct-drive motor to generate oscillatory ankle motion to mimic clonus behavior [54]. The motor output torque was transmitted to the user through a magnetorheological fluid (MRF) clutch. The device would switch to the clonus state based on the user's input stretch speed and sustained interaction torque. However, there were a few drawbacks for this design. It lacked a physiologically-accurate foot shape and the inversion/eversion degree of freedom (DOF) at ankle joint. The device was also mechanically complex due to the use of the MRF clutch. The clutch also introduced unwanted viscous friction torque and as a result the control algorithm had to compute real-time compensation and the device could not command a torque smaller than the viscous torque. Another novel exoskeleton device that created clonus-like behavior on healthy individuals was prototyped by Okumura et al. via a geared DC motor and cable-driven mechanism [55]. The device worn by healthy subjects converted them to mock patients by imposing external actuation force on the wearer's ankle joint to simulate the clonus beats for learners to feel and train. However, several limitations were evident in this design. The force output was relatively small, i.e., 10-20 N. Furthermore, the force control performance was not reported, so it was unclear if the device operated in open-loop current control or used a force sensor for closed-loop feedback. The clinical realism of these two devices were either not established [55], or only examined by two clinicians with minimal result reporting [54].

C. Project Overview

In this chapter, we present the design and evaluation of a novel ankle clonus training simulator. Haptic feedback force was generated from a series elastic actuator design. The foot-ankle assembly had two degrees of freedom (dorsiflexion-plantarflexion and inversion-eversion) and a realistic foot shroud. Evaluation tests involved benchtop performance experiments and a clinician validation study with experienced physicians and physical therapists.

Table 2.1: A summary of pre-programmed clonus parameters. Original column represents numerical design values initially extracted from the literature. Modified column lists the revised design values based on 9 experienced clinicians on Day 1 of clinical study [58].

	Original	***Modified***
Triggering factors *		
Dorsiflexion speed threshold	> 200° /s	> 150° /s
Hand position panel engagement	Must touch plantar metatarsal head, or both medial and lateral	
Inversion/eversion angle range	> 0°	NA
Sustaining factor		
Sustaining torque threshold	> 3 Nm	> 2 Nm
Clonus Simulation Characteristics *		
Frequency of ankle oscillation	5 Hz	6 Hz
Mean position of ankle oscillation	10° PF	0°
Peak-peak oscillation amplitude	8°	4° (decaying)
Duration	6 s	10 s

* In our convention, dorsiflexion and inversion are negative. Zero angular position is defined at the neutral position (shank perpendicular to foot).

2.2 Methods

A. Design Specifications

Our goal was to design a torque-controlled haptic device that rendered a realistic feeling of the muscle response of a patient with ankle clonus to trainees. Considering that an analytical

torque-angle profile of ankle clonus is lacking from the literature, the simulated ankle clonus behavior was defined empirically. Specifically, we quantified the ankle clonus assessment into (i) triggering factors, (ii) sustaining factors, and (iii) clonus simulation characteristic parameters (Table 2.1). This quantification of clonus was used to program the simulator's high-level controller, which calculated the simulated clonus muscle tone based on the user's input kinematics. The low-level torque controller was designed to accurately execute the torque command from the high-level controller. In addition, this device should also provide a safe and low-noise training environment for medical instruction.

B. Mechatronic Design and Modeling

The simulator has the appearance of a robotic lower leg, and its segment lengths and 3D-printed shroud contour were designed based on the anthropometric data of a 50^{th} percentile Caucasian male [107] (Fig. 2.1). To improve device portability (total weight < 7 kg) and reduce rotational inertia of the foot, most structural components were made of FR4 epoxy fiberglass for its high strength-to-weight ratio and the structural design was optimized via topology optimization for balanced stress distribution. The principal DOF was actuated (i.e., dorsiflexion-plantarflexion range of motion (DF/PF ROM): ± 30º). The auxiliary DOF was passive (inversion-eversion (I/E ROM): ± 10º), which was simulated by rotating the foot shroud relative to the underlying structural frame via a pair of inline spherical bearings in the fore and rear foot. The foot shroud geometry and dimensions were obtained from a 3D scanned prosthetic foot (US men's size 10) and the foot's inertial properties were matched with the real human foot [107]. The knee joint can be adjusted and locked easily into a seated or supine position (two common clinical examination poses) with a dowel pin.

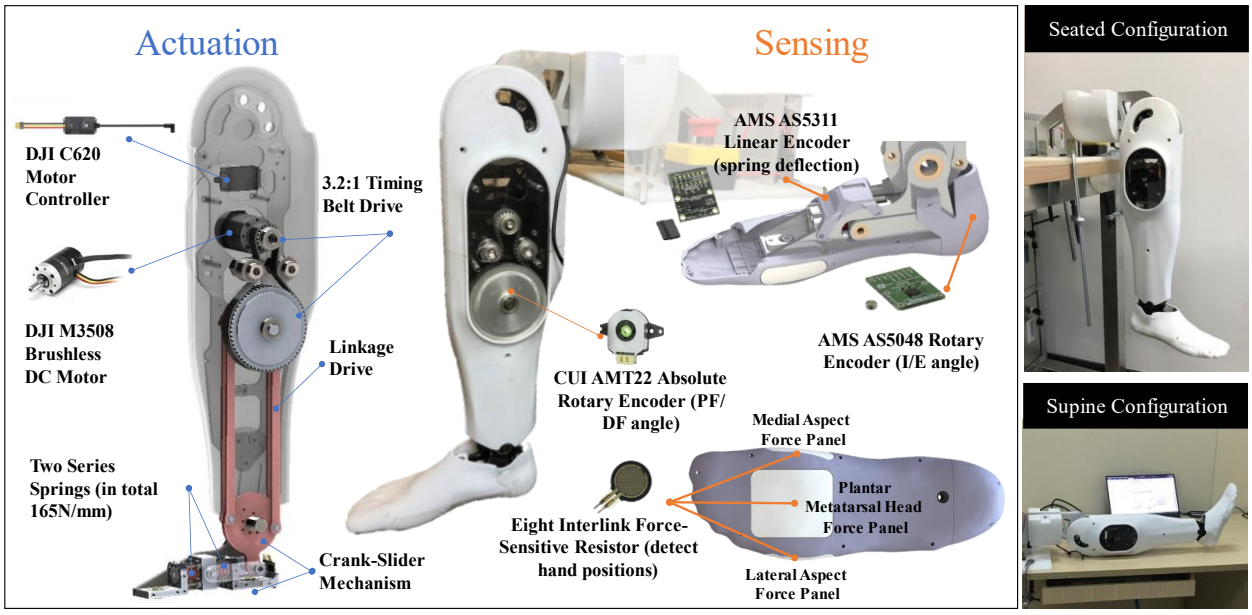

Fig. 2.1: The ankle-foot training simulator with major actuation and sensing components highlighted, as well as two operation configurations [58].

The series elastic actuation strategy was chosen for its safe human-robot interaction, accurate force control, robustness, and relatively low cost (Fig. 2.1) [108]. The specifications of the simulator were derived from previous devices [54,55]. The actuation torque was exerted via a crank-slider mechanism based on a spring cage mounted in the foot frame (Fig. 2.1 and 2.2). The slider in the middle of the spring cage rode on four miniature linear rails with ball bearings. To ensure resistance during both dorsi- and plantarflexion, the slider was preloaded by a die spring (1804N193, McMaster, USA) on each side of the slider, which resulted in a total series spring stiffness of ~165 N/mm. The simulator's drivetrain was actuated by a 150W brushless DC motor with an integrated two-stage planetary gearbox (~19:1) (M3508, DJI, China), followed by a single-stage 3.2:1 timing belt drive (MR5, Misumi, Japan) and a 1:1 linkage drive. The belt drive was advantageous in quiet and multi-turn operation but if spanning over long distance, its intrinsic compliance will drop to the similar magnitude of the series springs and influence the effective system stiffness. Therefore, a custom linkage drive consisting of four thin fiberglass bars was

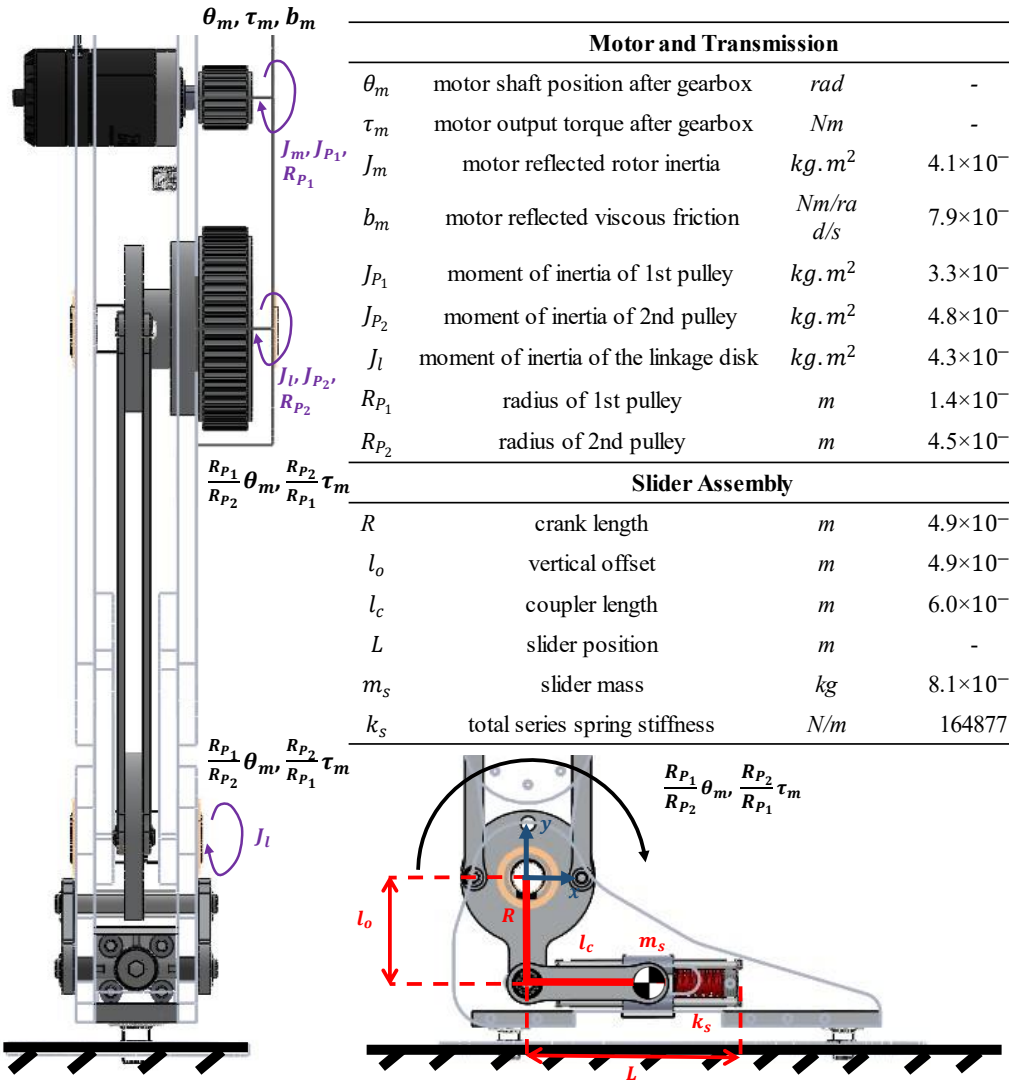

	Motor and Transmission		
θ_m	motor shaft position after gearbox	*rad*	-
τ_m	motor output torque after gearbox	*Nm*	-
J_m	motor reflected rotor inertia	$kg.m^2$	4.1×10^{-3}
b_m	motor reflected viscous friction	*Nm/rad/s*	7.9×10^{-2}
J_{P_1}	moment of inertia of 1st pulley	$kg.m^2$	3.3×10^{-6}
J_{P_2}	moment of inertia of 2nd pulley	$kg.m^2$	4.8×10^{-4}
J_l	moment of inertia of the linkage disk	$kg.m^2$	4.3×10^{-5}
R_{P_1}	radius of 1st pulley	*m*	1.4×10^{-2}
R_{P_2}	radius of 2nd pulley	*m*	4.5×10^{-2}
	Slider Assembly		
R	crank length	*m*	4.9×10^{-2}
l_o	vertical offset	*m*	4.9×10^{-2}
l_c	coupler length	*m*	6.0×10^{-2}
L	slider position	*m*	-
m_s	slider mass	*kg*	8.1×10^{-2}
k_s	total series spring stiffness	*N/m*	164877

Fig. 2.2: Diagram of key parameters in the kinematic and dynamic model [58].

combined with the belt drive to transmit actuation torque to the distal ankle joint, keeping the belt span distance minimal. As a result, this drivetrain could generate a peak ankle torque of 17 Nm, with an effective stiffness of ~5020 N/mm (an order of magnitude larger than the series spring stiffness, thus regarded as rigid).

A dynamic model of the simulator's SEA system was developed to guide choice of series spring stiffness to achieve a torque control bandwidth that was sufficiently high to replicate clonus behavior (Fig. 2.2). The crank-slider mechanism used in this design had nonlinear kinematics.

However, given the crank rotation angle would be within only ± 2º during operation, the equation of motion was safely linearized around an equilibrium point of crank angle at 0º. In addition, considering that the reflected motor inertia dominated the system's inertia, the model assumed the output end (i.e., simulator's foot) to be fixed on the ground and only the DOF of motor-driven slider movement in the spring cage was modeled to investigate system's natural frequency. Thus, with these two simplifications, the system dynamics were reduced to a 1-DOF linear oscillator (2.1). For a SEA, the large torque control bandwidth is limited by the open-loop system bandwidth, approximated by the system's fundamental natural frequency. Using Eq. 1, the spring stiffness was selected such that the system had a fundamental natural frequency at ~16 Hz, allowing a torque control bandwidth up to ~2 times of the maximum clonus motion frequency). This safety factor in control bandwidth was designed to account for any unmodeled dynamics (e.g., bearing friction, spring intrinsic damping, belt compliance) that might slow down the system.

$$0.0041\ddot{\theta}_m + 0.079\dot{\theta}_m + 41\theta_m = \tau_m \tag{2.1}$$

Furthermore, an array of onboard sensing capabilities monitored trainee's performance and provided real-time feedback (Fig. 2.1). Specifically, a linear encoder (AS5311, ams AG, Austria) mounted on the spring cage to measure spring deflection allowed calculation of the interaction force between the trainee and simulator, as part of the SEA strategy (without the need for expensive load cells). Two DOFs (DF/PF and I/E) of the simulator were sensed by two absolute rotary encoders (AMT22, CUI, USA; and AS5048, ams AG, Austria, respectively). These readings were used in the control logic to define whether the clonus would be triggered based on the trainee's input motion (Table I). Eight force-sensitive resistors (FSRs) (Model 400 and Model 402, Interlink Electronics, USA) were integrated into the foot shroud around the metatarsal heads (plantar, medial and lateral aspects) as simple touch sensors to detect whether the trainee's hand was

properly positioned on the forefoot (Table 2.1) [109]. With proper visualization means (e.g., a tablet or screen), data from this sensor array could also provide real-time performance feedback to the trainees for technique correction without the presence of an instructor.

C. Control Strategy

The control system design of the simulator followed the classical control scheme for SEA-based robots (Fig. 2.3) [90]. The low-level controller had a cascaded architecture (from innermost to outermost: current, velocity, and torque controls) and all loops updated at 1 kHz. The innermost control loop provided proportional-integral (PI) current feedback control and was regulated and executed by a motor controller (C620, DJI, China) with a pre-programmed current loop bandwidth of ~500Hz. Motor inertia compensation and current command were also implemented as feedforward current inputs. The middle PI velocity loop was added to provide a tight feedback loop around the motor to address backlash in the integrated gearbox. The velocity loop was tuned to achieve a bandwidth of ~50Hz, roughly 5 times faster than the desired outer torque loop (~10Hz) to guarantee the separation between servo control loops. Eventually, a proportional-derivative (PD) torque controller (essentially a position controller that modulated the spring deflection, given the SEA architecture) was implemented in the outermost loop that received torque output commands from the high-level controller.

The high-level controller was in the form of an impedance controller that produced a desired torque command (τ_d) and switched between clonus (2.2) and non-clonus (2.3) modes by evaluating if all clonus triggering criteria were satisfied (Table 2.1). Each mode was programmed via a desired reference motion trajectory and a set of impedance parameters (2.2). The estimated torque (τ) was calculated using the known series spring stiffness, crank position (using small-angle approximation), and spring deflection (ΔL) directly measured by the linear encoder (2.4).

$$\tau_d = K_{P\_C}(\theta_{clonus} - \theta_{tr}) + K_{D\_C}(\dot{\theta}_{clonus} - \dot{\theta}_{tr}) \tag{2.2}$$

$$\tau_d = -K_{P\_NC}\theta_{tr} - K_{D\_NC}\dot{\theta}_{tr} \tag{2.3}$$

$$\tau = k_s R^2 \left(\frac{R_{P_1}}{R_{P_2}}\theta_m - \theta_{tr}\right) = k_s R \Delta L \tag{2.4}$$

where θ_{clonus} and $\dot{\theta}_{clonus}$ are reference clonus oscillation ankle angle and angular velocity, while θ_{tr} and $\dot{\theta}_{tr}$ are trainee's input kinematics derived from the DF/PF rotary encoder. In clonus mode, the controller generated a sinusoidal reference angle trajectory with parameters defined in Table I, and the reference velocity was obtained by numerically differentiating the angle trajectory. In the non-clonus mode, the reference angle and angular velocity are 0, meaning that the equilibrium point was at neutral position and zero velocity. The impedance controller was a natural choice to control the ankle motion in the non-clonus mode, i.e., mimicking simplified ankle joint dynamics parametrized by linear stiffness (K_{P_NC}) and damping (K_{D_NC}). The use of an impedance controller also naturally extended to the clonus mode by defining an intensified interaction (due to hyperactive stretch reflex) between rhythmic clonus ankle motion and the trainee's input effort. The K_{P_C} (1 Nm/°) and K_{D_C} (0.03 Nm/(°/s)) were the set of virtual stiffness and damping for the clonus mode; similarly, K_{P_NC} (0.15 Nm/°) and K_{D_NC} (0.01 Nm/(°/s)) for the non-clonus mode. These two sets of impedance parameters were obtained from [105,106] with slight increase in the damping ratio to improve stability.

All sensor readings were accessed and packed by a lower-level microcontroller (Teeny 3.5, PJRC, USA) and then transmitted to the upper-level microcontroller (TI C2000, TMS28379D, Texas Instrument, USA) at 1.5 kHz. The control system was implemented on the upper-level

microcontroller and programmed using Simulink Embedded Coder (MATLAB 2019b, MathWorks, USA).

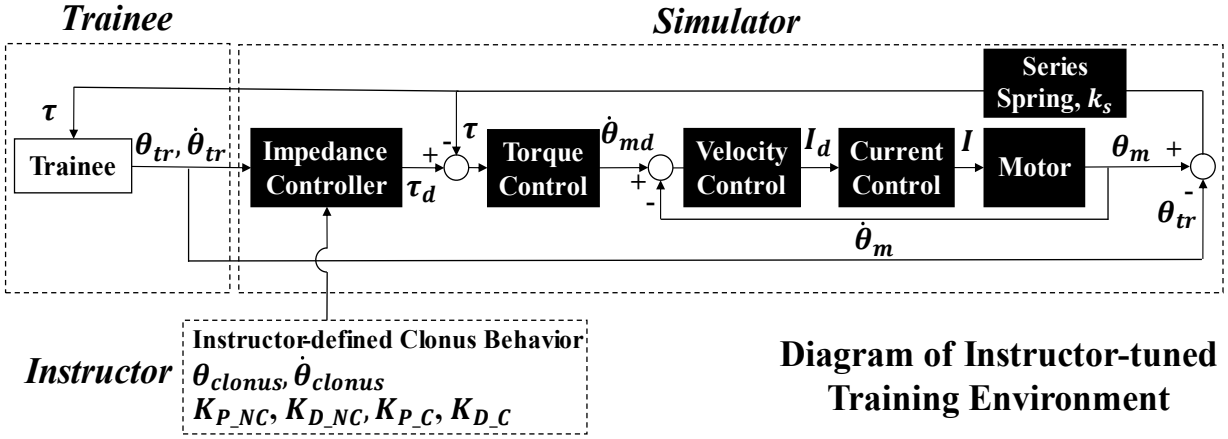

Fig. 2.3: Simulator's control system diagram with inputs from involved parties (trainee, simulator, and instructor). Subscript *d* means desired signal [58].

D. Benchtop Evaluation

A series of benchtop experiments were conducted to evaluate the torque estimation capability of our SEA system, as well as the performance of the low- and high-level controllers. To examine the accuracy of the torque estimated by the SEA system, the motion of the simulator foot was constrained and a torque sensor (TQM301-45N, Omega Engineering Inc., USA) was attached to the ankle joint so that the output torque generated by the motor was measured by the torque sensor. Randomized loadings were exerted on the system by manually rotating the motor rotor, up to $\pm$10 Nm. The estimated ankle torque derived from the deflection of the series springs (2.4) was then compared to the torque sensor reading. The root mean square error (RMSE) between the two signals was calculated to examine the effectiveness of torque estimation via the deflection of the series springs.

Next, a low-level torque control test was performed to validate the torque control accuracy

and bandwidth. With the controller described in Section 2.2C, the simulator was commanded to track a chirp torque command whose frequency swept from 0-10 Hz and amplitude varying between 2-6 Nm. The RMSE between the torque command and the spring-deflection estimated torque was calculated.

The next test was to evaluate the performance of the high-level controller. Three different scenarios were tested: a) no clonus (where the input was slow dorsiflexion), b) unsustained clonus (fast dorsiflexion but not maintaining torque), and c) sustained clonus (fast dorsiflexion and maintaining torque). The ankle angle reference trajectory was defined by the parameters in Table 2.1 (column labeled Original). Clinically, a response behavior will be considered to be "sustained clonus" when at least 5 consecutive beats are observed. The researcher (YP) manually performed the clonus assessment technique on the simulator, following guidance from an expert clinician

Fig. 2.4: Four subjects interacting with the simulator in two testing configurations that represented a patient in a seated or supine position [58].

(CMZ). All signals were sampled at 1 kHz and filtered using a 4^{th}-order Butterworth filter with a cut-off frequency of 50 Hz.

E. Clinician Validation

To establish simulation realism, we coordinated an expert clinician validation study in the Rehabilitation Center at the Zhejiang Hospital in Hangzhou, China and invited physicians and physical therapists (PT) to examine how well the prototype simulator could simulate typical ankle clonus behavior. The inclusion criteria were that subjects should have at least of 2 years of clonus assessment experience and perform at least 10 assessments per month. All recruited subjects had no prior experience with interacting with a robotic training simulator. The study was approved by the IRB at the University of Illinois at Urbana-Champaign and Medical Ethics Committee of Zhejiang Hospital.

The study was conducted over two consecutive days. Data analyses were based on input from 9 subjects on Day 1 and 8 on Day 2. The test protocol was the same for both days. Each subject was asked to induce sustained clonus at least three times in each of the two configurations (seated and supine), using the usual assessment technique (Fig. 2.4). For 16 out of 17 subjects, the first tested configuration was seated position. The controller parameters were the same between the two configurations. For each test configuration (i.e., seated and supine), the number of attempts to the first successful sustained clonus triggering was recorded. To document subjective feedback on the simulator performance and user experience, each subject answered a post-test questionnaire on 12 items (Table 2.2). Subjects were asked to evaluate these simulation items on a five-point scale, where a score of 3 matching the word “about right” was considered as an ideal score, meaning the simulated behavior felt similar to their clinical experience. To expedite controller design iteration, feedback received on Day 1 about the realism of the simulator was used to revise

the clonus parameters, which were implemented in the simulator's controller during Day 2 testing (Table 2.1, column Modified; Fig 2.5). Therefore, questionnaire scores between Day 1 and Day 2 were compared using two-sample, one-tailed t-tests with unequal variances ($\alpha = 0.05$) to study any significant change in simulation realism features per clinicians' feedback. In addition, all results were broken down into three subgroups based on job titles, i.e., all subjects, physicians only, PTs only.

Table 2.2: Post-test review questionnaire summary [58].

Item	**Simulation Realism Item**	**Score**				
		1	**2**	**3**	**4**	**5**
Clonus Triggering Factors						
1	Dorsiflexion velocity threshold to trigger clonus	Too slow		About right		Too fast
Clonus Maintaining Factors						
2	Sustaining torque threshold	Too Small		About Right		Too Large
Clonus Simulation Characteristics						
3	Frequency of ankle oscillation	Too low		About right		Too high
4	Oscillation amplitude					
5	Resistance torque magnitude					
6	Mean oscillation position	Too DF				Too PF

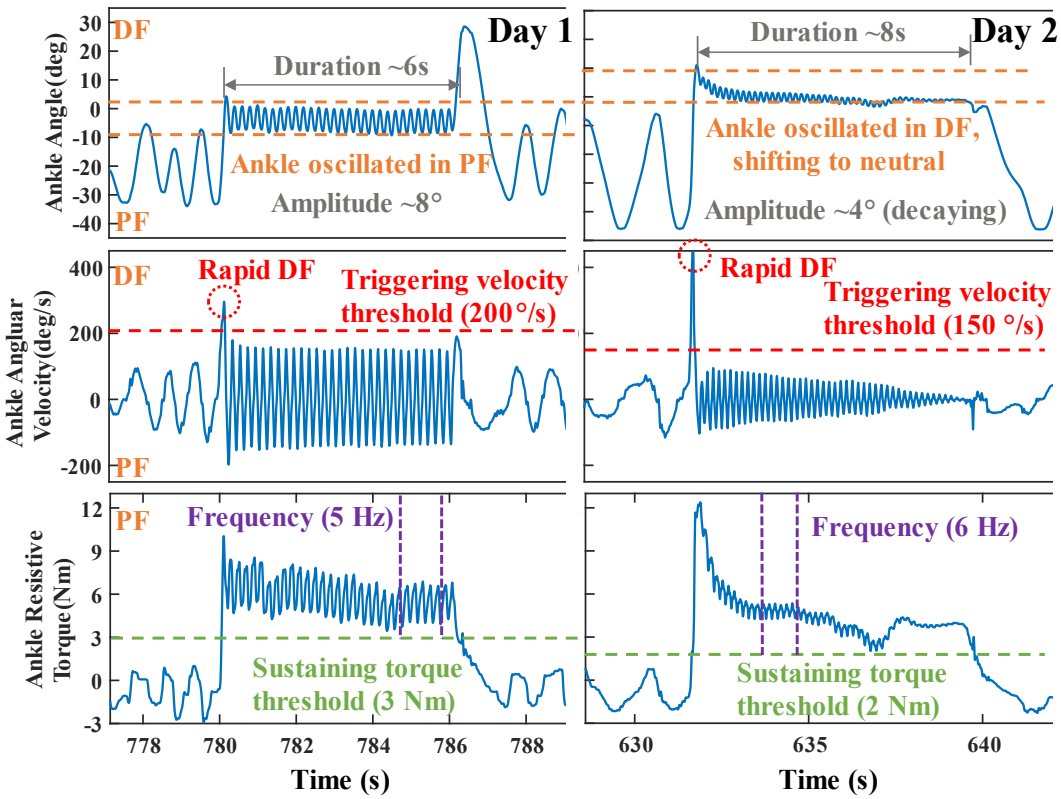

Fig. 2.5: Simulated clonus behavior before and after the controller revisions. (Left) Participant 8 on Day 1. (Right) Participant 17 on Day 2 [58].

2.3 Results

A. Benchtop Evaluation Results

The custom SEA system's torque estimation and torque control capabilities were verified (Fig. 2.6-2.7). The torque estimated by the deflection of the series springs matched well with the torque sensor reading, where the average RMSE was 0.20 Nm (Fig. 2.6). The tuned controller was able to track a chirp torque signal up to 10 Hz without sign of motor saturation, with average RMSE < 0.22 Nm (Fig. 2.7). Noticeable torque errors were found at the peaks of the sine wave at low frequency (i.e., ~1-3 Hz) and disappeared at higher frequency (i.e., > 3Hz). This error might be caused by motor gearbox stiction, since this error decreased as the frequency increased (i.e., motor started mainly experiencing dynamic friction). The high-level impedance controller was

able to simulate the behavior of a patient with clonus and to switch between clonus and non-clonus modes based on velocity and torque thresholds (Fig. 2.8). Specifically, clonus could not be triggered under low dorsiflexion velocity (Fig. 2.8, Left) and was not sustained when applied torque on the foot dropped below the torque threshold (Fig. 2.8, Middle). Only a combination of rapid dorsiflexion (i.e., > 200 °/s) and applied torque on the foot (i.e., > 3 Nm) induced a sustained clonus behavior (Fig. 2.8, Right). The experimental ankle angle profile obtained during sustained clonus case was qualitatively similar to a clinically-observed clonus behavior in terms of frequency and oscillation amplitude.

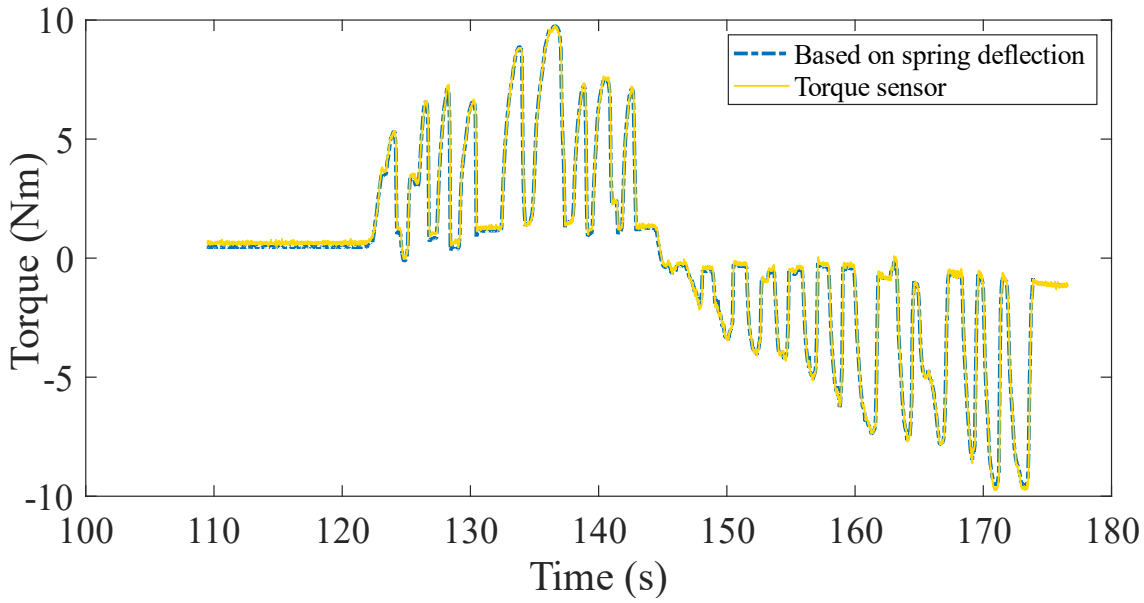

Fig. 2.6: Torque estimation test – comparison of torque computed from deflection of series springs and measured by a torque sensor [58].

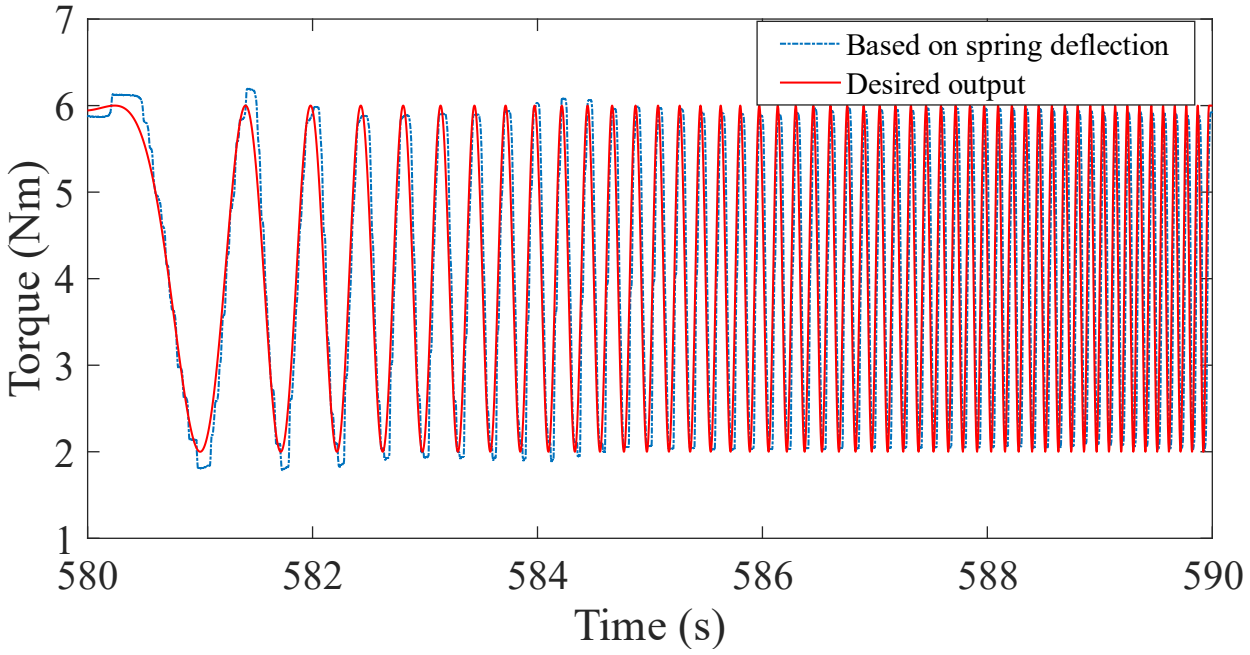

Fig. 2.7: Torque control accuracy and bandwidth test – comparison of torque computed from deflection of series springs and desired torque based on frequency swept from 0-10Hz and peak-peak amplitude of 4Nm [58].

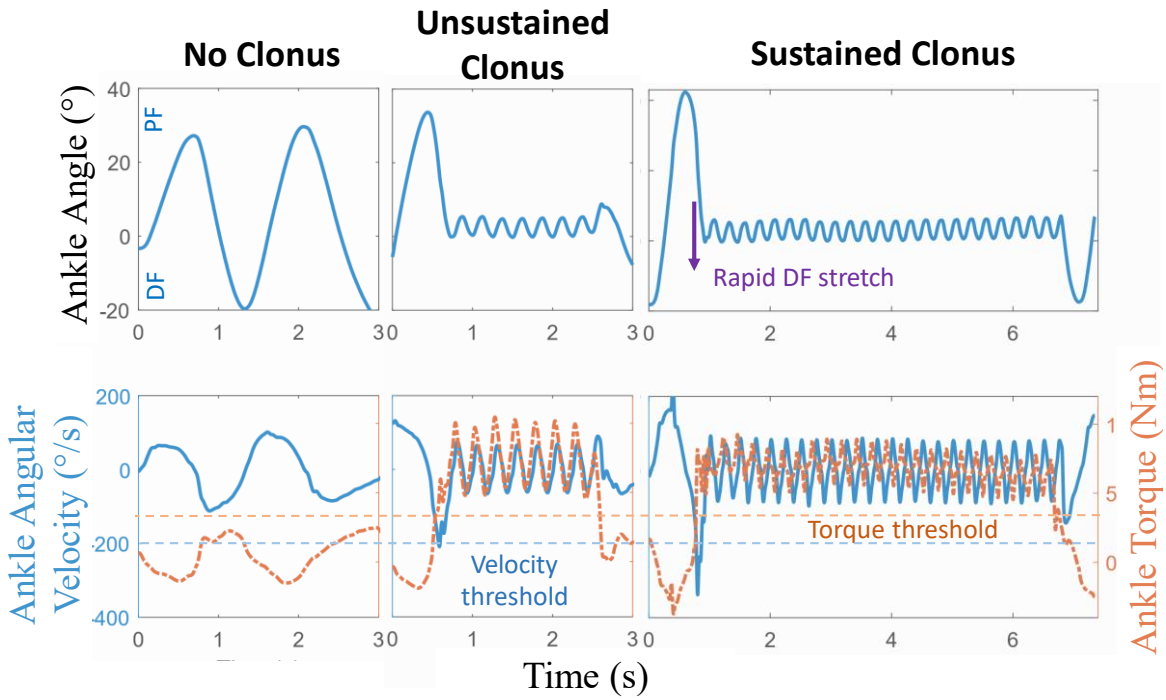

Fig. 2.8: Three operation states of the simulator: (Left) no clonus triggered due to low DF stretch speed. (Middle) Unsustained clonus triggered but not continued due to lack of DF torque. (Right) Sustained clonus behavior [58].

B. Clinician Validation Results

The simulator was validated by 20 clinicians in two configurations with the attempt numbers and questionnaire responses recorded, and data analysis was based on 17 of 20 clinicians who have sufficient experience with clonus assessment given the inclusion criteria (Table 2.3). On average, all subjects could successfully trigger a sustained clonus response within 4-6 attempts in the first tested configuration and 2-3 in the second (Table 2.4). The decrease in the number of attempts in the second configuration suggested a learning effect. The number of attempts to first success also showed trends with participants' backgrounds (Table 2.4). Participants with more years of assessment experience and more monthly assessments tended to require fewer attempts to success for both configurations, suggesting training and practice experience improve the efficiency of neurologic exam. On the other hand, no clear trend was observed in terms of the participants' medical degrees. The number of trials for PTs were nearly double compared to the average number used by physicians in both configurations. One possible cause for this large difference may have been that physicians had more experience assessing clonus as part of their job responsibilities, whereas PTs were used to trying to directly suppress clonus in patients, rather than assess/feel clonus, so there were extra adaptation and change of mindset required for PTs.

Table 2.3: Participant demographic background summary. In total 20 subjects were recruited and Subject 5, 12, and 19 were excluded due to lack of experience.

ID	Medical Education Degree	Job Title	Year of experience	Monthly clonus assessment
1	Master (7 years)	Physician	13	50
2	Master (8 years)	Physician	5	30
3	Master (8 years)	Physician	15	30
4	Master (7 years)	PT	5	20
6	Bachelor (4 years)	PT	5	66
7	Bachelor (4 years)	PT	7	14
8	Bachelor (5 years)	Physician	20	8
9	Bachelor (4 years)	PT	7	18
10	Master (7 years)	PT	3	3
11	Bachelor (4 years)	PT	5	7
13	Bachelor (4 years)	PT	5	8
14	Bachelor (4 years)	PT	4	7
15	Bachelor (4 years)	PT	8	8
16	Bachelor (4 years)	PT	6	0
17	Master (8 years)	Physician	3	20
18	Bachelor (5 years)	Physician	10	4
20	Bachelor (4 years)	PT	6.5	7

Table 2.4: Number (mean ± standard deviation) of trials to the first success for different subgroups.

	Day 1		Day 2
1st configuration	4.0 ± 3.6		6.4 ± 5.0
2nd configuration	2.0 ± 1.7		3.4 ± 3.1
	Years of Clonus Assessment Experience		
	$0 < x \leq 5$	$5 < x \leq 10$	$10 < x \leq 20$
1st configuration	6.7 ± 4.1	4.5 ± 5.0	1.0 ± 0.0
2nd configuration	3.2 ± 2.6	2.7 ± 2.9	1.0 ± 0.0
	Number of Clonus Assessments Per Month		
	$0 < x \leq 5$	$5 < x \leq 10$	$10 < x$
1st configuration	6.5 ± 4.9	4.5 ± 3.9	2.3 ± 1.9
2nd configuration	3.6 ± 3.1	1.3 ± 0.4	1.7 ± 0.9
	Medical Degree		
	Bachelor		Master
1st configuration	5.2 ± 4.7		5.7 ± 4.5
2nd configuration	3.1 ± 3.0		2.2 ± 1.8
	Job Title		
	Physician		Physical Therapist
1st configuration	3.0 ± 4.0		6.6 ± 4.5
2nd configuration	1.2 ± 0.4		3.6 ± 2.9

For each questionnaire item, the average score was calculated for each test day and by subgroup of physician or PT (Fig. 2.9). After the controller tuning/calibration, Day 2 subjects felt that simulated clonus behavior was generally "about right" in terms of realism and controller

revision moved the mean scores of questionnaire items closer to the ideal with reduced scoring variance. Additionally, the average scores for sustaining torque threshold and oscillation amplitude were significantly reduced, moving closer to 3. There was little difference in scores between seated and supine configurations.

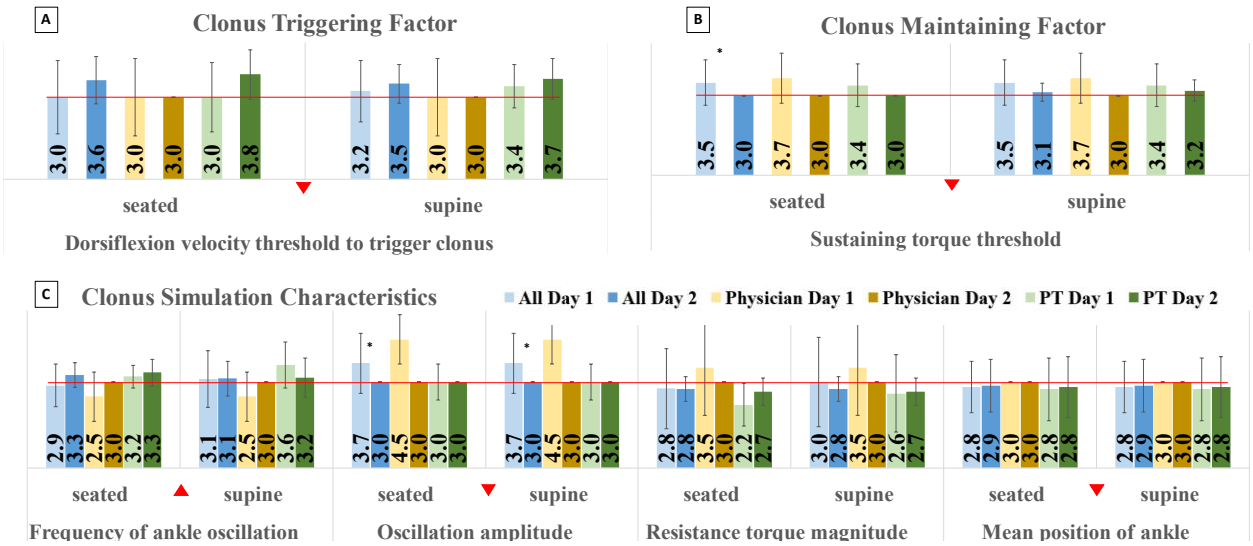

Fig. 2.9: Mean (standard deviation bars) of questionnaire scores for both days across three groups (i.e., all subjects, physicians only, and PTs only). Red lines indicate the ideal score. Red triangles indicate the tuned item and its tuning direction after Day 1 feedback (Table 2.1). T-tests were only performed between All Day 1 and All Day 2 ($\alpha = 0.05$) [58].

The assessment techniques of participants were grouped into either of two types (1 or 2) based on examining hand position within the supine or seated configurations (Fig. 2.10). Clinicians with Type 1 technique tended to only support the plantar surface of the foot to dorsiflex the ankle, whereas those with Type 2 technique would hold onto both plantar and dorsal surfaces of the foot to get a firm grasp. Each individual participant tended to use the same hand position (i.e., the same type) for both configurations. Since both Types 1 and 2 touched the plantar FSR sensors required in the simulator triggering criteria (Table 2.1), both techniques were considered to be effective. It was found that the assessment technique type had no clear trend with participant background, e.g., years of experience and monthly assessments. Therefore, this result implied that a clinician's

technique tended not to vary with experience or proficiency and was likely adopted at their training institutions. The percentage of physicians used Type 1 technique was 50% vs. 42% among PTs, showing no standardized technique existed in either group.

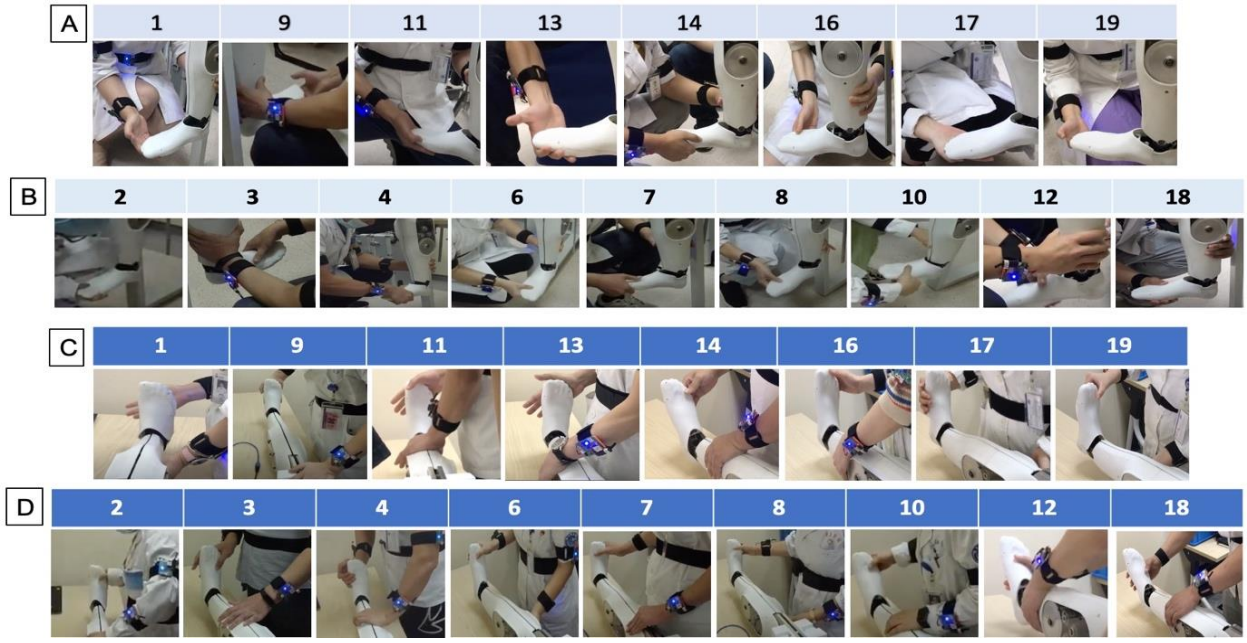

Fig. 2.10: Examining hand position categories for seated and supine configurations. Seated configuration: (A) Type 1 (B) Type 2. Supine configuration: (C) Type 1 (D) Type 2.

2.4 Discussion

In this paper, a SEA-based ankle-foot simulator that replicated the behavior of a patient with ankle clonus and could be deployed in medical training programs as a robotic mock patient was proposed and developed. In the benchtop validations, the prototype simulator with the custom SEA system had very good estimated torque accuracy, torque control accuracy, and sufficient bandwidth for our application (i.e., 5-8 Hz of clonus oscillation) (Fig. 2.6-2.7). The use of a SEA resulted in a compact and cost-effective simulator design. The overall gear ratio of ~60:1 in the prototype simulator allowed a commercial-grade, small motor (DJI M3508 motor size of 4.2cm in diameter and 6.6cm in length; cost of $140, including a C620 motor controller) to be used and all

components fitted within the human lower-leg geometry. Thanks to the economical actuation system, this simulator with good torque control fidelity was developed in a total BOM cost less than $500. Just the force/torque sensor alone used in the previous designs cost more than the overall cost of our device. Therefore, the SEA design not only demonstrated good torque control capability but also lowered the cost barrier for the training simulator to be adopted.

To validate the realism of clonus simulation, 17 clinicians with experience doing clonus assessment evaluated the clinical performance of the prototype simulator. Feedback from the Day 1 session with 9 clinicians was used to refine the controller behavior and then the modified controller was evaluated during the Day 2 session with 8 different clinicians (Table 2.1, Fig. 2.5). After revising the clonus controller parameters prior to the Day 2 session, the variance of scores decreased in all items except for mean ankle position, which stayed the same. Note that the large score variances on Day 1 (Fig. 2.9) may be partly due to the large variance in years of experience among Day 1 subjects (SD: 5.3 on Day 1 vs. SD: 2.7 on Day 2). Subjects on average demonstrated quick adaptation to the simulated clonus behavior and successfully triggered a sustain clonus on the simulator within a few trials using their usual technique. The small number of attempts to success implied that the simulator's control logic (i.e., triggering and maintaining clonus) aligned with participants' existing clinical knowledge and training. Physicians were found to be able to successfully trigger sustained clonus with fewer attempts than PTs. It is possible that this difference was due to physical therapists' job habit/mindset to suppress clonus in patients, rather than to induce and assess clonus like physicians. This additional adaptation for PTs might have caused them to take longer to succeed. Also, it was interesting to see there was no consistent manual technique across the subjects, i.e., both Type 1 and 2 technique were observed with roughly equal percentage. Both were considered as valid hand positions, given the current simulator control

logic. If in the future more clinical evidence suggests one of them would be more effective, the control logic could be adjusted (e.g., placing additional contact sensors on the dorsal surface of the foot) to drive the technique standardization via the proposed training simulator.

Valuable feedback was received throughout the clinician validation study and several design limitations were recognized. Subjects commented that in the supine configuration, the patient's leg will often be externally rotated at the hip with the knee flexed; however, our prototype lacked a thigh and hip joint. Furthermore, some level of randomized variation was suggested in the controller parameters to prepare the trainees with the unpredictable nature of clinical cases. Similarly, simulations of other common abnormal muscle behaviors at the ankle joint such as rigidity and spasticity (as selected) were suggested to increase training sophistication. Therefore, future work should involve enhancing the dexterity of the simulator to match the DOFs of the lower limb; and in order to maximize the potential of device hardware, more variations of simulation algorithm should be implemented.

2.5 Conclusion

The prototype ankle-foot SEA-based simulator was validated in both benchtop tests and clinician evaluation. The experimental results and clinical feedback were promising and suggested that this device could mimic a real patient by a) generating a simulated clonus behavior whose triggering and maintaining mechanism aligned with clinicians' experience, and b) recreating a relatively realistic haptic response of affected muscles. However, the device still lacks the full dexterity of a human lower-extremity, which requires further design iterations. The use of a SEA system resulted in not only a high-performance research simulator, but also a cost-effective and compact design that could become viable to be widely deployed as a valuable training tool for learners.

CHAPTER 3

DESIGN AND VALIDATION OF A ROBOTIC ANKLE-FOOT TASK TRAINER FOR ANKLE TENDON REFLEX ASSESSMENT

Abstract

Ankle (or Achilles) tendon reflex is commonly assessed in a neurologic examination. For a clinician trainee to master the correct assessment technique of ankle tendon reflex and to be able to distinguish among various reflex activity levels indicating health or abnormality, repetitive training and practice are necessary. We developed a robotic medical education training simulator that would generate a realistic reflex behavior depending on the simulated reflex activity level selected when given a tendon tap assessment. A reflex model was developed to estimate the ankle reflexive torque based on the input tap force. This reflex model prediction was validated in simulation and then implemented into our robotic simulator prototype. Benchtop results demonstrated that our simulator was able to accurately deliver the reflexive torque pattern required to simulate the clinical reflex response to the trainee. Nine experienced clinicians evaluated the device through a blind assessment test and a disclosed assessment test. Subjects were able to distinguish three intensity levels of tendon reflex with a good accuracy of 77 % on average. Subjects also demonstrated their assessment technique, which mostly aligned with the simulator hardware and control design. Clinical feedback were collected for future design iteration.

3.1 Introduction

A. Overview of Ankle Tendon Reflex Assessment

A reflex is an involuntary response to an external stimulus. Pathological changes in muscle stretch reflex behavior are often early indicators of neurologic diseases, so for this reason, the reflex evaluation is a regular and important neurologic exam procedure [7]. Among many types of reflexes, we focused on the deep tendon reflex (DTR) or muscle stretch reflex in this work. The DTR could be induced by application of a rapid stretch stimulus to the tendon of the muscles examined. Ankle (or Achilles) tendon reflex is one of the most commonly examined DTRs and also often more difficult to elicit than the knee tendon reflex. A clinician will use a medical reflex hammer to tap the ankle tendon, in order to trigger the reflex and evaluate its intensity [8]. This tendon tap technique is widely used among therapists and physicians [7].

The goal of a tendon tap test is to evaluate if the tendon stretch reflex is healthy or affected by neurologic conditions [7]. After a proper tap applied by the examiner on the ankle tendon, the muscle stretch reflex response will be triggered and induce the contraction of the calf muscles, causing the foot to plantarflex. A normal tendon reflex usually generates a moderate plantarflexion. On the other hand, if the elicited plantarflexion is too weak or too strong (brisk), then hypo- or hyperreflexia (including sometimes even ankle clonus) is observed. Clinically, the reflex activity is graded using DTR levels [110] (Table 3.1). DTR 4 usually associate with certain neurologic conditions (such as stroke [111]), while DTR 0 means reflex activity is absent and DTR 1 is often considered as weaker but healthy reflex. In the scope of this work, we aimed to focus on simulating only DTR levels 2, 3, and 4, since they are more frequently seen clinically.

Table 3.1: Clinical scale used to score different levels of reflex activity. Only DTR 2-4 are simulated in this work.

DTR Grading	0	1	2	3	4
Description	Absent	Sluggish or diminished	Normal	Exaggerated	Markedly hyperactive

Effective triggering of the ankle tendon reflex consists of three factors: a) proper stretching of the muscle before tapping via passive dorsiflexion of the ankle, b) a brisk and forceful tap with the hammer, and c) correct tap location on the tendon [7,8]. Clinically, the examiner will use one hand to support the plantar surface of the foot to maintain a proper tension on the tendon/muscle (Fig. 3.1, left). Then the examiner will use the other hand to apply an effective tap with the reflex hammer at the insertion of the Achilles tendon above the calcaneus.

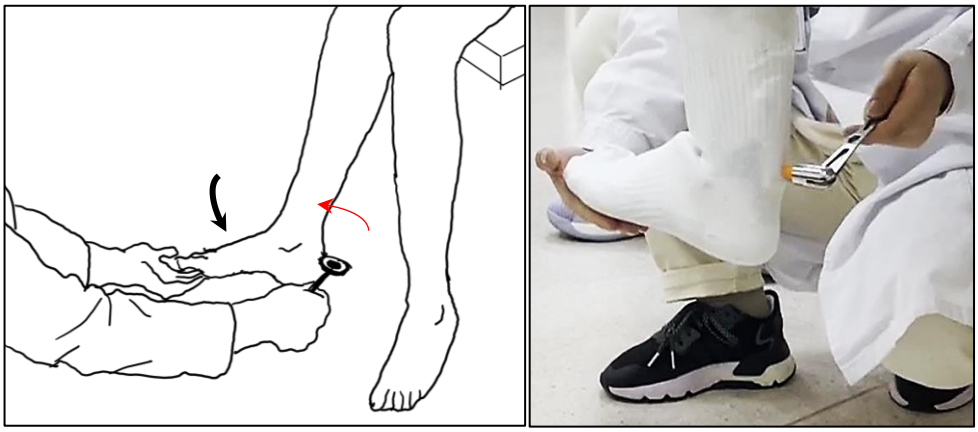

Fig. 3.1: (Left) A sketch of tendon tap technique to assess Achilles tendon reflex, adapted from [7]. (Right) A tendon tap test on the ankle-foot simulator.

B. Project Overview

In this project, we continued to utilize the SEA-based ankle-foot simulator's torque control capability and expand its functionality to also simulate the ankle tendon reflex response when an

external tap is given by the trainee, via incorporating a new artificial tendon structure and proposing a reflex response model. A series of simulation, benchtop, and clinical evaluations were conducted to validate our design.

3.2 Mechatronic Design

A. Ankle-Foot Training Simulator Design Overview

The training simulator for ankle clonus has the appearance of a robotic lower leg (Fig. 3.2A), and its segment lengths and 3D-printed shroud contour were designed based on the anthropometric data of a 50^{th} percentile Caucasian male [107]. The ankle joint is actuated, where the main dorsiflexion-plantarflexion (DF-PF) range of motion (ROM) is ± 30º and the auxiliary inversion-eversion (I-E) ROM is ± 10º. The foot shroud geometry and dimensions were obtained from a 3D scanned prosthetic foot (US men's size 10).

The series elastic actuation strategy was chosen for its safe human-robot interaction, accurate force control, robustness, and relatively low cost [82]. By deploying a SEA module in our simulator, a relatively high gear ratio would allow a compact motor with reasonable operation current (<13 A) to be used, and a pair of series springs (stiffness of ~165 N/mm) would serve as a compliant and inexpensive torque sensor that could accurately measure interaction joint torque between the user and robot.

Furthermore, an array of onboard sensing capabilities monitored trainee's performance and provided real-time feedback. Specifically, a linear encoder (AS5311, ams AG, Austria) measuring spring deflection allowed calculation of the interaction torque between the trainee and simulator. Two degrees of freedom (DOF) (i.e., DF/PF and I/E) of the ankle joint were sensed by two absolute rotary encoders (AMT22, CUI, USA; and AS5048, ams AG, Austria, respectively). Eight force-

sensitive resistors (FSRs) (Model 400 and Model 402, Interlink Electronics, USA) were integrated into the foot shroud as simple touch sensors to detect whether the trainee's hand was properly positioned on the forefoot. Considering the procedure of ankle tendon tap does not involve I/E DOF and focuses on the tap location (not on hand positioning on the foot), therefore the I/E angle encoder and FSRs were temporarily disabled in this study.

B. Design of an Artificial Achilles Tendon Structure

In order for the ankle-foot simulator to mimic the ankle tendon reflex response, an artificial Achilles tendon structure was incorporated at the back of the shank shroud like the biological counterpart, allowing the trainees to tap on it to trigger the tendon reflex response (Fig. 3.2B-D). The design goal of this tendon structure was three-fold. First, the tendon should be able to sense the tap force applied by trainees so that this input signal would be sent to controller for generating the reflex response. Second, clinically, a triggering sweet spot exists along the Achilles tendon where it is most effective to elicit the reflex and our simulator needs to teach trainees to properly hit within this area. Thus, if trainees tap away from the sweet spot, the exerted tap force should be attenuated by the tendon structure and no reflex would be triggered. Furthermore, tapping on the artificial tendon structure should feel similar to a biological tendon.

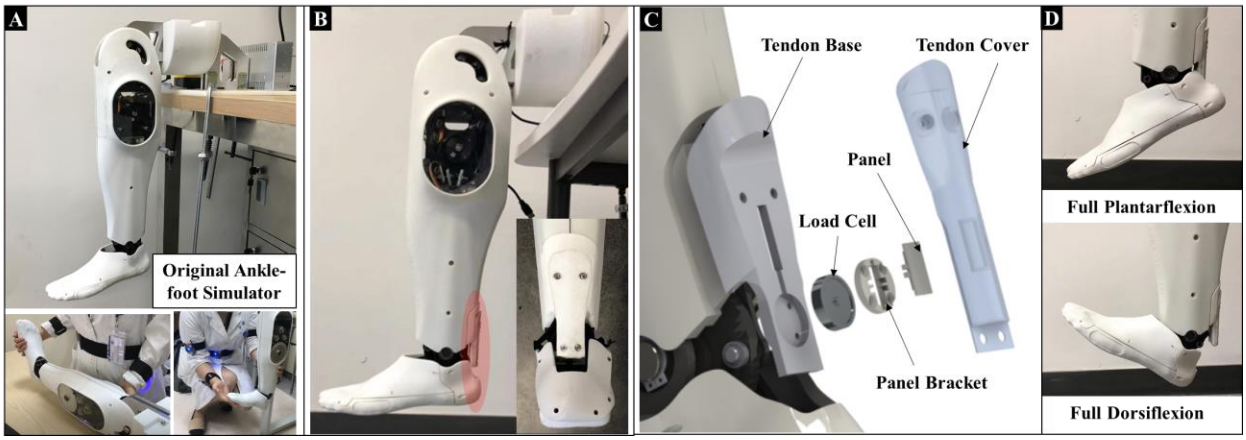

Fig. 3.2: Overview of ankle-foot training simulator design. (a) Original simulator designed only for clonus assessment training. The simulator was operated by clinicians at supine and seated configurations, adapted from [15]. (b) Addition of artificial tendon structure (highlighted in red). (c) The exploded view of the tendon design. (d) The simulator with the tendon structure at full plantarflexion and dorsiflexion.

These design considerations resulted in a multi-layer tendon design with a uni-axis compression load cell (1171-100N, Arizon Technology, China) (Fig. 3.2C). The tendon base structure was 3D printed using PLA material serving as a rigid foundation for the load cell to mount. Following the recommendation by the neurologist in the research team (CMZ), the load cell was mounted directly behind the ankle joint (i.e., the tendon triggering sweet spot). This sweet spot was designed to be a rectangle of 2 cm long along the longitudinal direction the tendon and 1 cm wide. To fit into the tight space of the tendon structure, a pancake-type (5 mm thick) compression load cell was utilized. The original sensing spot on this load cell was a circle of 2 mm in diameter. To cover the entire 2 cm × 1 cm area, a two-piece resin adaptor (a bracket and a panel) was fabricated and mounted on top of the load cell. The panel sitting on top of the load cell expanded the sensing area from the tiny circle to the entire 2 cm × 1 cm space. The bracket constrained the panel motion such that it could only move vertically. Resin was selected for low sliding friction and high manufacturing precision via stereolithography 3D printing. During practice, trainees might tap anywhere on the tendon structure, but only taps within the rectangular sweet spot would be

registered as valid input triggering signals via the load cell. A soft silicone-molded tendon cover was installed as the outermost layer. The cover was designed to be relatively thin on top of the load cell (i.e., correct tap location) to improve force transmission and thick in other areas (i.e., wrong tap areas) to dampen the tap force propagating to the load cell and provide a compliant and elastic feeling upon impact.

3.3 Tendon Reflex Response Quantification

A. Quantification of Input Tap Force

The development of this simulator started with understanding the clinically observed input tap force signal during ankle tendon assessments. Based on a human subject study on ankle reflex activity by Chung et al. [111], with a custom instrumented reflex hammer, the profile of the tap signal was observed to be similar to an impulse signal with a duration of ~15 ms. The force threshold that would evoke an ankle tendon reflex was measured to be 13.6 ± 4.3 N for stroke patients and 19.1 ± 5.4 N for healthy controls. Given these results, we proposed an impulse signal with an amplitude of 13 N and a duration of 15 ms and used it as an input signal to validate if our proposed reflex model could generate torque profiles similar to those observed clinically.

B. Quantification of Reflex Activity across DTR Levels

Individuals with higher DTR levels will exhibit more exaggerated and brisker reflex behavior at the ankle given the same input tap force. According to the statistical results from subjects with various DTR levels [111], it was observed that the peak reflexive torque would increase with DTR level. In [111], this increasing trend was quantified by calculating the reflex gain (the ratio between peak measured reflexive torque and the peak tap force) across DTR levels (Table 3.2).

Clinically, DTR 4 will often be accompanied by a few beats of clonus [1]. Therefore, two beats of clonus were superimposed on the DTR 4 torque profile. The oscillatory frequency (6 Hz) and torque fluctuation amplitude (1.5~2 Nm) of the simulated clonus behavior were adapted from our previous study [58].

Table 3.2: The mean and standard deviation of the reflex gains across DTR levels, extracted from [111] (n: number of subjects tested) [151].

DTR		1 (n=2)	2 (n=28)	3 (n=9)	4 (n=6)
Measured reflex gain	mean	1.36	3.51	4.65	9.67
	SD	0.42	2.16	2.77	6.39

C. Estimation of Reflexive Torque Profile Shape

A parametric method to the model reflex behavior was proposed by Mirbagheri et al. [112–114]. In their works, a system identification approach was used to quantify the ankle dynamics and ankle position was controlled as a disturbance signal to the ankle. Therefore, in the original formulation, the input signal was position and then it went through a time derivative (to get velocity), a half-wave rectifier (to make negative values to zero), a 40 ms reflex loop delay, a reflex gain (unit of viscosity, converting velocity to torque), a first-order filter, and eventually second-order reflex dynamics. This formulation is very inspiring, but does not exactly fit in our application, because our input signal is the tap force measurement rather than position. Thus, we used a different interpretation of the reflex gain (unit of length, converting force to torque), similar to the reflex gain definition in Chung et al. [111]. In addition, the time derivative and rectifier blocks associated with processing position signal were removed. As a result, our custom reflex model consisted of a 40 ms reflex loop delay, a reflex gain, a first-order filter, and second-order reflex dynamics, all connecting in series (Fig. 3.3A).

In this reflex model, there are four parameters: reflex gain (G), natural frequency (ω_n) and damping ratio (ζ) of the reflex dynamics, and cut-off frequency of the first-order filter (p). Specifically, the reflex gain determines the amplitude of the reflexive torque profile, while the other three parameters modulate the shape of the profile. By observing the real DTR 2 and 4 reflexive torque profiles reported in [111] (adapted in Fig. 3.7B), the durations of reflexive torque were almost the same (~600 ms, where rising for ~200 ms and decaying for ~400 ms) and the main difference was the amplitude (peak torque of ~2 Nm for DTR 2 and ~6 Nm for DTR 4). Therefore, in our design, the same values for the set of parameters ω_n, ζ, and p were used for all DTR levels and only G was varied (Table 3.3).

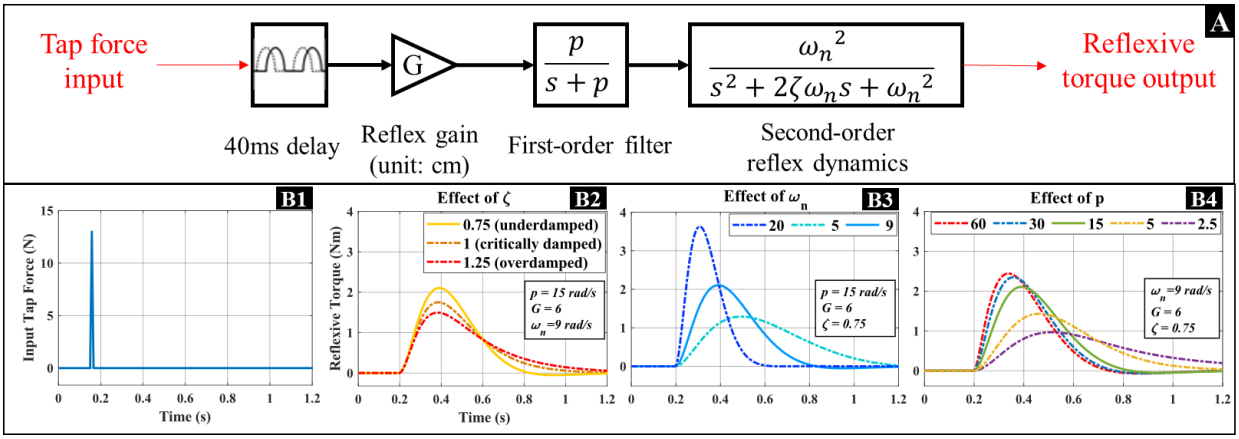

Fig. 3.3: (A) The reflex model proposed in this work. (B1-4) A parameter study that demonstrates how each model parameter modulates the time-domain shape of the reflexive torque profile. Solid lines corresponded to chosen values and dashed lines indicated effect of parameter variations.

A model parameter study was conducted to investigate how each parameter affects the torque profile (Fig. 3.3B). The same tap force input (Fig. 3.3B1, described in Section 3.3A) was given and only one parameter varied in each scenario. ζ was most straightforward and it determined whether the torque profile was under-, critically-, or over-damped. An underdamped value of 0.75 was chosen to create a steeper decaying profile so that reflexive torque terminated at ~0.8 s (Fig.

3.3B2). Both ω_n and p modulated the pole locations of first-order filter and second-order reflex dynamics, so smaller values led to a slower response (or stronger filtering effect). Specifically, ω_n defined the general shape of the torque profile, while p provided secondary shape adjustment (or filtering). ω_n was selected to be 9 rad/s in order to have a ~200 ms rising period and a ~400 ms decaying period (Fig. 3.3B3). Given ω_n = 9 rad/s, if p was smaller than 9 rad/s, it introduced a dominating slow pole (Fig. 3.3B4 for p = 2.5 and 5 rad/s), whereas if p larger than 9 rad/s, the response was mainly determined by ω_n (i.e., a pair of slower complex poles) and increasing p from 15 to 60 rad/s only marginally speeded up the response (Fig. 3.3B4 for p = 15, 30, and 60 rad/s). Therefore, p was chosen to be 15 rad/s. In summary, this set of parameter values (ζ = 0.75, ω_n = 15 rad/s, and p = 9 rad/s) was chosen to modulate the simulated reflexive torque profile across DTR levels (Table 3.3).

The remaining parameter, reflex gain (G), was determined based on the relationship between reflex gain and DTR level in Table 3.2. Specifically, values of G for DTR 2-4 matched the relative magnitude of the mean values in Table 3.2. The reflex gain for DTR 3 was 1.3 times larger than that of DTR 2, while the reflex gain for DTR 4 was 2.8 times larger than that of DTR 2. The baseline G at DTR 2 was selected as 6 to generate a peak reflexive torque of 2 Nm, and as a result, G values for DTR 3 and 4 were calculated to be 8 and 16.5 using the scaling relationship.

Table 3.3: Summary of our reflex model parameters for DTR 2-4 [151].

DTR	G	ω_n (rad/s)	ζ	p (rad/s)
2	6			
3	8	9	0.75	15
4	16.5			

During the development of reflex model, we started from Mirbagheri et al. [112–114] and further tried simplifying the model from 3rd order to 2nd order by removing the first-order filter. However, it was found that a 2nd order model could not provide such steep decay between 400 and 600 ms in Fig. 3.7B. If using a smaller damping ratio (i.e., ζ<0.75) to accelerate the decay, underdamped oscillation would occur at the tail of the torque profile. The extra pole introduced by the first order filter provided additional adjustability (i.e., two control knobs ω_n and p) on the time-domain shape of the profile and resulted in a smoother rising period as well as a steeper decay period, better matching the clinical observed profile. Similar first-order filter was also used in other studies such as [115].

D. Control Design

The simulator was designed to mimic the ankle joint behavior of individuals with DTR 2-4. When the trainee manipulates the simulator's foot before tendon tap, the simulator should only exhibit inertial and gravitational effects ($I_f\ddot{\theta}$ and $m_f glcos\theta$), and joint impedance (τ_{imp}) (3.1). τ_{imp} is the output torque of the impedance controller and is defined by (3.2). When there is a valid tendon tap, he desired haptic behavior rendered to the trainee ($\tau_{trainee\_d}$) should consist of three components: a) natural foot dynamics (i.e., foot inertia and gravity), b) ankle joint impedance (τ_{imp}), and c) reflexive response upon tap (τ_{reflex}) (3.3).

$$\tau_{trainee\_d} = I_f\ddot{\theta} - m_f glcos\theta + \tau_{imp}(\theta, \dot{\theta}) \tag{3.1}$$

$$\tau_{imp} = K_p(\theta_{eq} - \theta) - K_d\dot{\theta} \tag{3.2}$$

$$\tau_{trainee\_d} = I_f\ddot{\theta} - m_f glcos\theta + \tau_{imp}(\theta, \dot{\theta}) + \tau_{reflex}(DTR) \tag{3.3}$$

In this equations, I_f (0.035 kg.m^2) and m_f (1.06 kg) are foot inertia (about the ankle joint) and mass based on 50th percentile male data [107], and θ and its time derivatives are measured ankle joint kinematics. K_p and K_d are the simulated ankle stiffness and damping (18 Nm/rad and 0.6 Nm/(rad/s), respectively), and θ_{eq} is the equilibrium ankle angle (17° in plantarflexion) [111].

When the trainee is ready to perform the tendon tap assessment, ankle joint angle and tap force signals will be monitored as triggering criteria. If the load cell embedded in the tendon structure detects a tendon tap with peak amplitude above 13 N and the ankle position is between neutral position (0°) and 10° dorsiflexion, a mock triggering signal (an impulse of 13 N with 15 ms duration, i.e., the same input signal as in Fig. 3.3B1) will be sent to the reflex model to generate the reflexive torque (τ_{reflex}) for the specific DTR level being simulated. This mock signal was chosen over the real-time load cell signal because this low-cost load cell exhibited non-negligible ground noise even with filtering, which would cause unwanted chattering of the ankle if fed to the controller as an input signal. To ensure the consistency of each tendon tap trial, once all triggering criteria were satisfied, the same mock input signal would be sent. To reduce the noise in the load cell measurement, the load cell readings (i.e., ADC values) were low-pass filtered with a 4th order Butterworth filter with a cut-off frequency of 20 Hz in real-time. Considering the load cell reading amplitude (especially the high-frequency tap force signal) might be distorted due to filtering and potential damping effect of the silicone tendon cover, the ADC values of the load cell were calibrated using a research-grade force sensor. The calculated torque command in (3.1) or (3.3) was executed by a cascaded torque controller (from innermost to outermost: current, velocity, and torque controls, developed in [58]) and all signals were sampled at 1 kHz.

3.4 Evaluations

A. Benchtop Evaluations

In order to validate the hardware design, proposed reflex model, and torque tracking capability, a series of benchtop and simulation tests were conducted.

Artificial Tendon Structure Force Sensing Evaluation

The new artificial tendon structure was fabricated and its capability for detecting static and dynamic loads was evaluated via a static load validation test and a dynamic impact force calibration test before mounting on the simulator. A ground-truth force sensor (PASPORT PS-2189, PASCO, USA) was mounted on a vertical linear rail test rig and the load cell was at the bottom (Fig. 3.4). In the static test, the force sensor would be initially in contact with the load cell and then different weights between 5 N and 25 N were placed on the force sensor to exert static loads on the load cell. In the dynamic test, the force sensor free-fell onto the load cell from different initial heights to mimic tap forces with different peak forces (approximately 15, 20, 25, 30, and 35 N; 10 trials per height). In both tests, the load cell readings were compared to the readings from the gold standard force sensor. Furthermore in the dynamic test, the filtered ADC reading of the load cell was calibrated into force measurement using the force sensor as a benchmark. To replicate the impact between medical reflex hammer and the tendon structure, a commercial reflex hammer's rubber hammer head was disassembled and attached to the metal testing probe of the force sensor.

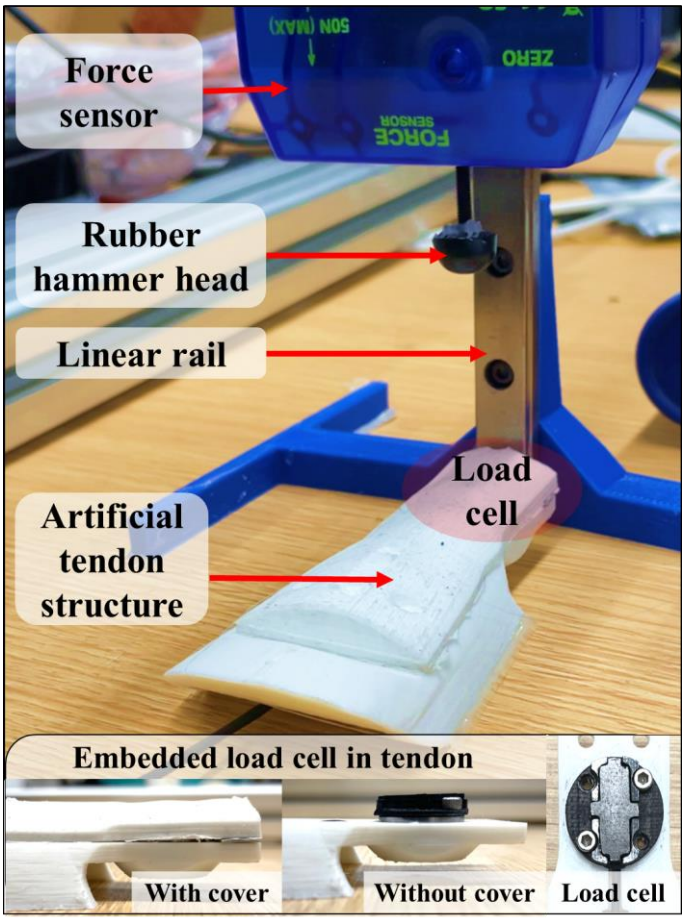

Fig. 3.4: A test rig to validate and calibration the force sensing of the artificial tendon structure.

Reflex Model Simulation Evaluation

The proposed reflex model was tested in simulation (MATLAB 2020b, MathWorks Inc., Natick, MA) at different DTR levels when given an impulse force signal (amplitude of 13 N and duration of 15 ms). The resulting reflexive torque profiles were compared to literature data [111] (Fig. 3.7B).

Control System Torque Tracking Evaluation

After the tendon hardware and reflex model simulation were validated, the mechatronic and control systems were implemented on the simulator prototype and were tested with and without triggering the reflexive torque. First, the simulator's foot was manually moved by hand

with increasing frequency (1~2.5 Hz) and no tap was given. In this case, only natural foot dynamics and joint impedance were rendered. Next, the ankle simulator's foot was supported by hand near a neutral angle position and tendon taps were given to trigger reflex behavior at DTR 2-4. To validate torque control fidelity in both scenarios, the root mean square error (RMSE) between the torque command and measured torque was calculated.

B. Clinical Evaluations

In order to further validate the simulator's realism, we coordinated an expert clinician validation study in the Rehabilitation Center at the Zhejiang Hospital in Hangzhou, China. We invited 10 clinicians (6 physicians and 4 physical therapists)to examine how well the prototype simulator could simulate the ankle tendon reflex behavior (Table 3.4 and Fig. 3.5). The only additional inclusion criteria for the study was subjects needed to have a medical related Bachelor degree or above with at least 5 years of ankle tendon tap assessment experience. One physician (Subject 5) was excluded from data analysis due to lack of experience. All subjects have given informed consents before test sessions. The study was approved by the IRB at the University of Illinois at Urbana-Champaign and Medical Ethics Committee of Zhejiang Hospital.

Table 3.4: Demographic summary of participating subjects. Subject 5 was removed due to lack of experience.

Subject ID	Job Title	Education	Medical Field	Years for DTR evaluation	# of Evaluation per month
1	Physician	Master	Rehabilitation Medicine	12	10
2	Physician	Master	Rehabilitation Medicine	5	8
3	Physician	Master	Rehabilitation Medicine	9	8
4	Physician	Master	Rehabilitation Medicine	7	30
6	Therapist	Bachelor	Rehabilitation Medicine	9	15
7	Therapist	Bachelor	Rehabilitation Medicine	9	2
8	Therapist	Bachelor	Rehabilitation Medicine	10	10
9	Physician	Master	Internal Medicine-Neurology	10	20
10	Therapist	Bachelor	Rehabilitation Medicine	7	2

The validation study consisted of a blind assessment test and a disclosed assessment test. In the blind assessment test, the simulator provided 9 simulations (3 simulation trials per DTR

level, 3×3 = 9) in randomized sequence to each subject, who did not know the preset level. For each of the 9 trials, the subject was asked to assess the simulated DTR level using their typical tendon tap technique and made a judgement on reflex grading. The agreement between simulated level and subject's judgement was reported as agreement percentage. In the disclosed test, the subject was told the DTR level being simulated and was asked to closely examine and provide feedback on the simulation aspects of each DTR level, as well as on the reflex triggering criteria. Subjects scored each simulation aspect using a five-point Likert scale where a score of 3 represented simulated behavior aligned with subject's experience, while a score of 1 or 5 suggested deviation (low or high, respectively) from the clinical observed behavior (Table 3.5). Also, subjects were asked to demonstrate their typical reflex triggering technique, and their triggering techniques were documented in terms of the ankle joint for properly stretching the plantarflexor muscle and tendon, tap location, hand positioning, and peak tap force.

Fig. 3.5: Clinicians evaluating the ankle tendon reflex using tendon tap technique.

Table 3.5: Five-point Likert scale questions during the disclosed assessment test.

Simulation Realism Item	Score				
	1	2	3	4	5
Amplitude of reflexive torque	Too low				Too high
Responsiveness of Reflex behavior	Too slow		About right		Too fast
Duration of reflex behavior	Too short				Too long

3.5 Results

A. Benchtop Validation

The static load validation test results demonstrated good match between the load cell and the gold standard force sensor (Fig. 3.6A). A linear regression between load cell and force sensor resulted in a R^2 value of 0.999 and a slope of 0.96 (a slope of 1 indicated perfect match), suggesting good static load detection capability. In the dynamic force calibration test, means and standard deviations (across 10 trials) of peak filtered ADC readings were calculated and were calibrated with averaged peak force sensor measurement under each force condition. These data exhibited a good linear fit with R^2 value of 0.991 (Fig. 3.6B). This linear regression equation (force = 0.56×ADC-0.011) was used to convert the load cell's ADC reading to actual tap force on the tendon structure.

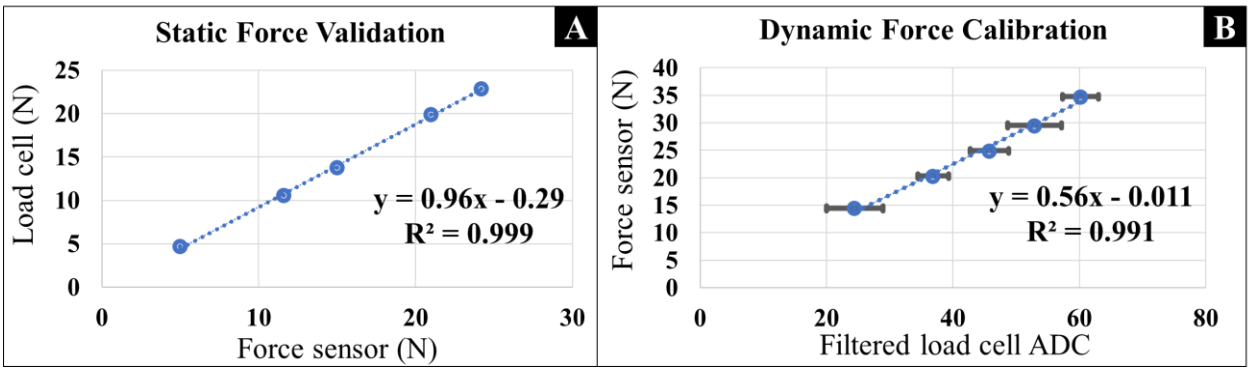

Fig. 3.6: Results of (A) static load validation and (B) dynamic force calibration (error bars: standard deviations).

The proposed reflex model, with the control parameters given in Table 3.3, generated simulated reflexive torques at DTR 2 and 4 (without clonus) very similar to clinically observed torque profiles reported in [111] (Fig. 3.7). We were unable to directly validate the shape of the torque profiles for DTR 3 and 4 (with clonus) due to lack of literature data, but the peak torque magnitude of DTR 3 matched the results in [111], and DTR 4 with clonus would be validated in the clinical study.

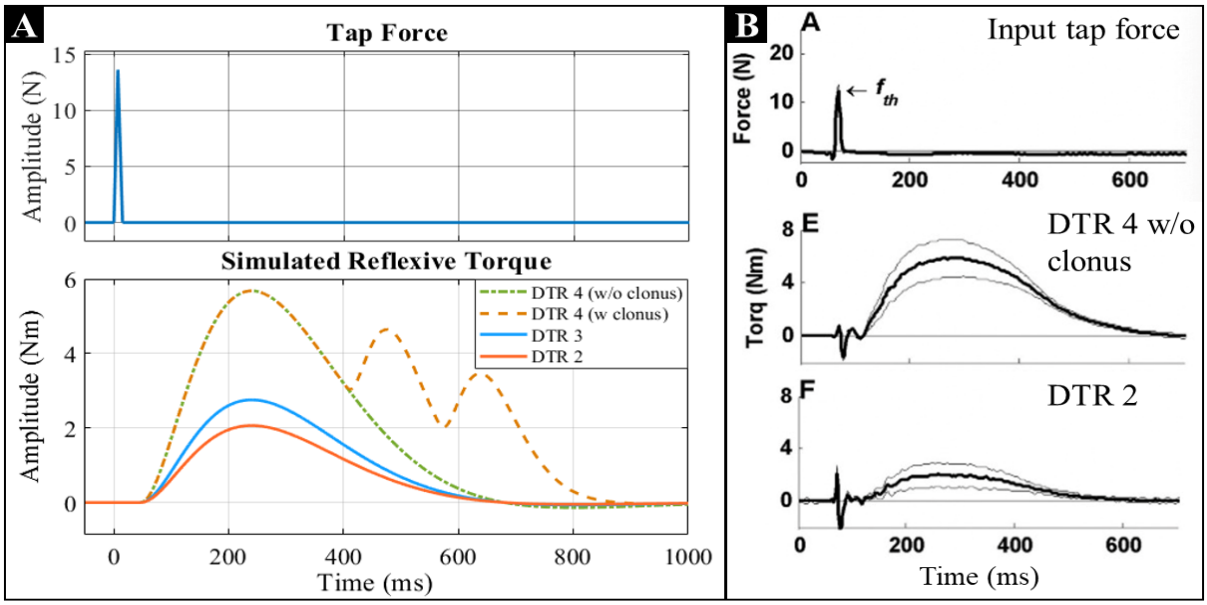

Fig. 3.7: (A) Simulation results of the reflex model at DTR 2-4 [151]. (B) Clinically observed response of DTR 2 and 4 reported in Chung et al. [111] were adapted with permission and compared with the

After the new tendon structure and reflex model were validated, they were implemented on the simulator prototype where the control system was tested. The simulator demonstrated good torque tracking capability when mimicking foot dynamics, ankle impedance, and reflexive torque (Fig. 3.8 and 3.9). When no tendon tap was given, and as the motion frequency increased, the torque error slightly increased but remained low (RMSE 0.18 Nm) throughout the test (Fig. 3.8). Next, the simulator's ankle was manually held at near neutral position to be ready for tendon tap. Since this position deviated from the equilibrium position of the impedance controller, a plantarflexion torque (roughly 2 Nm) was present at the beginning of each trial (Fig. 3.8, bottom). This torque was as expected and represented a combination of ankle muscle stretching and gravitational effect. With a tap at t = 0, a reflexive plantarflexor torque was commanded after an intentional 40 ms reflex loop delay, together with the baseline torque, forming the torque command. Across DTR 2-4, this torque command was tracked accurately by the simulator with a RMSE of 0.17, 0.24, and 0.19 Nm, respectively (Fig. 3.9). Another observation was that the actual torque generation had a slight delay (~25 ms) compared to the torque command.

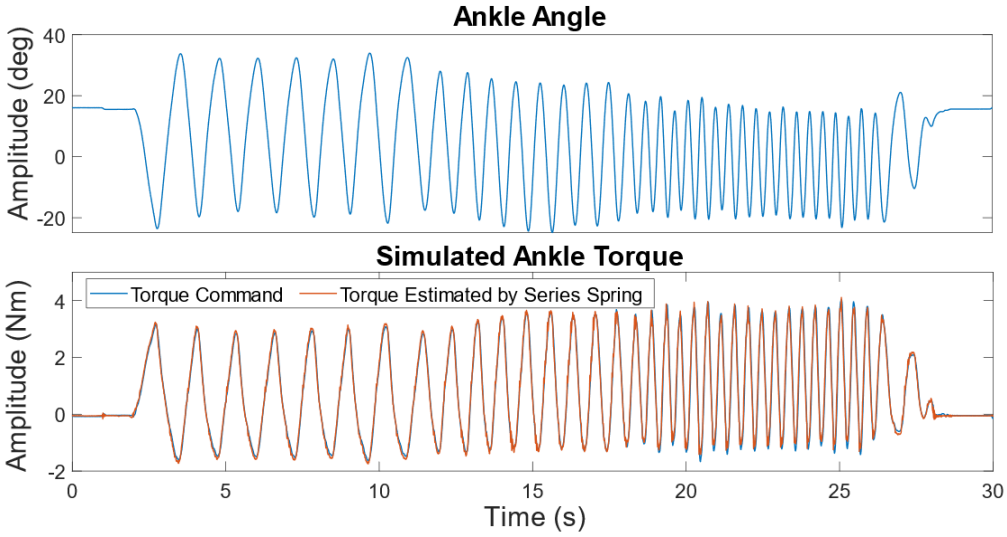

Fig. 3.8: Benchtop results of only simulated foot dynamics and joint impedance.

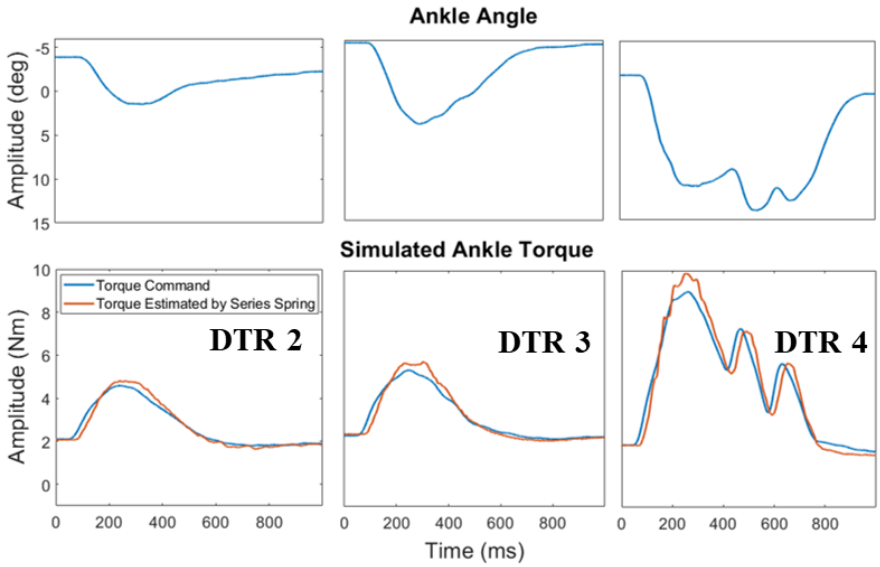

Fig. 3.9: Benchtop results with reflexive torque at DTR 2, 3, and 4 (tap force applied at t = 0) [151].

B. Clinical Validation

Across nine of ten clinician subjects, during the blind assessment test, the overall agreement percentage between the simulated DTR levels and subjects' judgements was 77% ± 18% (Table 3.6). DTR 4 had the highest agreement percentage (85%) as it was the most distinctive with the clonus behavior. DTR 3 was easily confused with DTR 2 due to subtle torque amplitude difference, explaining its lowest agreement percentage. In addition, most physical therapists noted that they would pay less attention to DTR 3 in their daily work environment, since usually they considered a DTR 3 reflex behavior as non-pathologic but just brisker than normal, requiring no rehabilitation need. If dividing the subjects into subgroups, physicians and therapists had similar subgroup agreement percentages, but the standard deviation was lower for physicians.

Table 3.6. Blind assessment test results in terms of agreement percentage.

	Agreement Percentage (%)					Subgroup	
	Subject	DTR2	DTR3	DTR 4	Mean	Mean	SD
physician	1	100	67	33	67	80	14
	2	67	100	100	89		
	3	67	67	100	78		
	4	56	100	0	67		
	9	100	100	100	100		
therapist	6	67	100	100	89	75	25
	7	67	0	67	44		
	8	33	67	100	67		
	10	100	100	100	100		
	Mean	78	67	85	77		
	SD	22	38	23	18		

In the disclosed assessment test, subjects closely evaluated each aspect of the simulation and scores were in general close to 3 (i.e., appropriate design), suggesting that subjects thought that the simulated reflex behavior at DTR 2, 3, and 4 aligned with their clinical experience (Table 3.7). For responsiveness at DTR 3, a score of 2.7 was given, so subjects expected the reflex behavior should occur faster. Torque amplitude at DTR 4 was scored at 3.3 meaning that the DTR 4 torque might be higher than clinically observed behavior, but at the same time a standard deviation of 0.7 might suggest potential lack of consensus among subjects on this item.

Table 3.7: Disclosed assessment test results across DTR 2-4. For amplitude, responsiveness, and duration, a score < 3 indicated too low/slow/short, and a score > 3 indicated too high/fast/long, respectively.

		Mean	SD
DTR2	Amplitude	3.2	0.4
	Responsiveness	2.9	0.6
	Duration	3.0	0.0
		Mean	SD
DTR3	Amplitude	3.0	0.5
	Responsiveness	2.7	0.5
	Duration	3.1	0.3
		Mean	SD
DTR4	Amplitude	3.3	0.7
	Responsiveness	3.0	0.5
	Duration	3.1	0.3

Subjects were asked to demonstrate the three triggering criteria for the ankle tendon reflex behavior and their technique was quantified (Table 3.8) and these observations mostly aligned with our predefined triggering criteria. On average, subjects first supported the foot at 3.6° in dorsiflexion to pre-stretch the plantarflexor muscle and then tapped on the tendon at 0.8 cm below the ankle joint, with a peak force of around 20 N. Large variances were observed for each feature across subjects might indicate a lack of standardized technique and also suggest that the simulator's triggering criteria should be more lenient that accept a wider range of ankle angles and tap locations as valid inputs.

Table 3.8: A comparison between experimentally recorded triggering criteria and predefined triggering criteria. Negative ankle angle of indicated a dorsiflexed position. Negative tap location suggested tapping below the ankle joint.

	Ankle Angle (degree)	Tap Location (cm)	Peak Tap force (N)
Mean (SD)	-3.6 (6.9)	-0.8 (1.0)	20.0 (5.2)
Predefined Triggering Criteria	-10 ~ 0	0	> 13

3.6 Discussion

In this chapter, we presented our approach to develop a medical education training simulator that could replicate different levels of ankle reflex behavior during tendon tap assessments. An artificial tendon structure and a load cell were installed on the existing ankle-foot simulator from [58] for trainees to perform tendon tap practice. A reflex model was proposed to compute the corresponding reflexive torque at the ankle based on the input tap force. Preliminary simulation, benchtop, and clinical results (with 9 experienced physicians and therapists) are promising in that the reflex model could generate a realistic reflexive torque profile. This torque command and resulting overall haptic experience could be accurately delivered to the trainee via our ankle-foot simulator.

In Section 3.3D, we explained that, due to a relatively high baseline noise, the raw load cell signal had to be additionally filtered, calibrated, and taken threshold before feeding into the controller. Furthermore, during the clinical validation, when some subjects tapped on the tendon structure with a tilting angle, the load cell could not detect that off-axis tap force well (i.e., with shearing component) and failed to trigger a reflex response even at the correct tap location and with enough force. In that case, investigators had to remind subjects of hitting the tendon more carefully to exert vertical force. A more expensive or multi-axis load cell might save these engineering workarounds and clinical hints, but the device cost would significantly increase, so this was a design trade-off. One of the initial design goals for the simulator prototype was cost-effective [58]. Therefore, throughout this project, we strived to keep the simulator affordable, so an inexpensive uni-axis compression load cell (~$150 including the sensor and signal conditioner) was used to detect the tendon tap force. However, based on the documented triggering technique during the clinical study, a scattered distribution of tap locations (centered around 0.8 cm below the ankle joint with a standard deviation of 1 cm along the ankle tendon) was observed even for experienced clinicians. Thus in future iteration, other possible design approaches that enable a larger detection area should be considered, such as building an instrumented reflex hammer (such as [116,117]) or covering the Achilles tendon area with a pressure sensor matrix.

For the simulator's control system, while different reflexive torque profiles were implemented, one simplification we made was using the same set of impedance control parameters (stiffness and damping) and the same triggering force threshold (> 13 N) across DTR 2-4. However, clinically, individuals with DTR 2 and 3 reflex behaviors are usually healthy, while DTR 4 reflex is often observed in spastic patients. Therefore, to further improve the simulation sophistication, two different sets of impedance parameters and tap force threshold could be designed for healthy

and spastic individuals. It is known that a patient with ankle spasticity exhibits higher ankle muscle tone with increased stiffness and damping [114], and tendon reflex response could be triggered more easily with a lower tap force than a healthy individual [111]. During the clinical study, several subjects helped fine-tune the impedance parameters on the fly and they ended up with a stiffness of 0.05 Nm/rad for DTR 2 and 3 (healthy individuals) and 0.25 Nm/rad for DTR 4 (spastic patients), comparing to the original value of 0.15 Nm/rad. Two subjects also mentioned that nonlinear stiffness profile should be implemented (i.e., higher stiffness towards the end of ROM). Also, participating clinicians on average tapped the tendon with a peak force of 20 N, aligning with the reported force threshold for healthy individuals [111] (see Section 3.3A). Therefore, in the future, the triggering force threshold could be further set as ~20 N for DTR 2 and 3, and ~13 N for DTR 4.

Furthermore, we observed the delay of torque generation (~ 25 ms) using the current torque controller during the benchtop test. However, we were unsure how much a difference that this adjustment would make, so we decided to first obtain subject feedback on the responsiveness of the reflex behavior during the clinical study. And indeed subjects on average expected the reflex behavior to occur more responsively for DTR 2 and 3 (scores of 2.9 and 2.7, respectively). To compensate this issue, a naïve approach could be reducing the intentional reflex loop delay in our model from 40 ms to 15 ms. In the long term, feedforward control scheme should be incorporated into the low-level torque controller to improve the tracking performance.

3.8 Conclusion

In this chapter, we presented our design methodology and validation cycle for developing a robotic training simulator that could replicate ankle reflex behavior during tendon tap assessments. Benchtop and clinical validation results are promising for deploying a SEA-based

training simulator to medical education setting. In addition, the lack of standardized technique observed during the clinical study may further motivate the need of introducing robotic simulators that provide consistent and accessible training for future clinician learners.

CHAPTER 4

UPPER-EXTREMITY ROBOTIC MEDICAL EDUCATION TASK TRAINER FOR SPASTICITY AND RIGIDITY ASSESSMENT

Abstract

The goal of this study was to validate a series elastic actuator (SEA)-based robotic arm that can mimic three abnormal muscle behaviors due to upper motor nueron lesions, namely lead-pipe rigidity, cogwheel rigidity, and spasticity for medical education training purposes. Key characteristics of each muscle behavior were first modeled mathematically based on clinically-observed data across severity levels. A controller that incorporated feedback, feedforward, and disturbance observer schemes was implemented to deliver haptic target muscle resistive torques to the trainee during passive stretch assessments of the robotic arm. A series of benchtop tests across all behaviors and severity levels were conducted to validate the torque estimation accuracy of the custom SEA (RMSE: ~ 0.16 Nm) and the torque tracking performance of the controller (Error: < 2.8 %). A clinical validation study was performed with seven experienced clinicians to collect feedback on the task trainer's simulation realism via a Classification Test (CT) and Disclosed Assessment Test (DAT). In the CT, subjects were able to classify different muscle behaviors with an accuracy > 87 % and could further distinguish severity level of each behavior satisfactorily. In the DAT, subjects generally agreed with the simulation realism and provided suggestions on misclassified conditions for future iteration. Overall, subjects scored 4.9 out of 5

for the potential usefulness of this device as a medical education tool for students to learn spasticity and rigidity assessments.

4.1 Introduction

A. Overview of Rigidity and Spasticity

Spasticity and rigidity are common abnormal muscle behaviors [5] and are characterized by distinct resistive muscle tone characteristics when the the affected muscle is passively stretched (Fig. 4.1). Rigidity is often observed in patients with Parkinson's disease, manifested as an increased muscle tone which is independent of the stretch speed [118]. There are two types of rigidity: a) lead-pipe rigidity (LR) which exhibits a uniformly elevated muscle resistance across the full range of motion and b) cogwheel rigidity (CR) which has an intermittent pattern of resistance with a frequency of 6-9 Hz [119]. Unlike rigidity, spasticity (SP) manifests as an increased muscle tone but with stretch speed dependency and is commonly observed in patients with neurologic conditions that cause upper motor neuron lesion (e.g., stroke, cerebral palsy, spinal cord injury). A typical spasticity resistance response is marked by an abrupt increase in the resistance called "catch" at a relatively consistent angle within the range of motion (ROM) and followed by a quick drop of resistance called "release" [120].

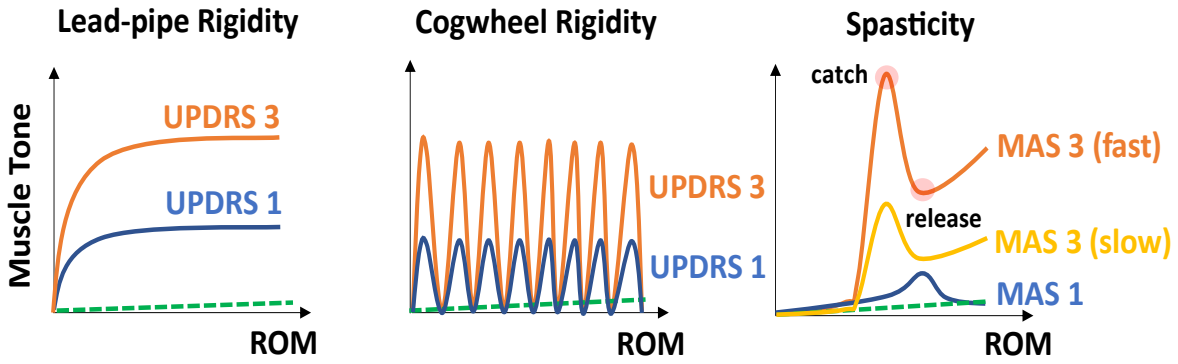

Fig. 4.1: Conceptual schematics comparing lead-pipe rigidity, cogwheel rigidity, and spasticity muscle tones during a passive stretch test (dashed green line: healthy muscle behavior).

B. Current Medical Training Methods and Challenges

Clinical assessment of these behaviors is done by passively moving the joint at various speeds to stretch the affected muscle. Based on the resistance felt, the clinician will diagnose the type and severity level of the behavior. To classify different severity levels of spasticity or rigidity, the examiner relies on qualitative assessment tools such as clinical scales (e.g., Modified Ashworth Scale (MAS) shown in Table 5.1, or motor portion of the Unified Parkinson's Disease Rating Scale (UPDRS) shown in Table 5.2, respectively). A score of 0 indicates the absence of spasticity/rigidity (i.e., healthy behavior), whereas higher and increasing scores indicate increasing severity of the spasticity/rigidity condition. Due to the qualitative and ambiguous nature of using these scales, clinical diagnosis often leads to subjective interpretations and introduces inter-rater reliability issues across different clinicians [121].

Given the subtlety and variation observed within and between different abnormal muscle behaviors, accurate diagnosis is built upon a good understanding of these behaviors and repetitive hands-on practice. However, for current clinical/medical learners, the training opportunity and consistency is often limited by the availability and small number of practice patients [52]. One promising approach to address this training challenge is the deployment of robotic task trainers to provide realistic and easily accessible practice opportunities for future medical trainees [20].

C. Review of Previous Robotic Task Trainers

Only a few task trainer designs have been proposed in the past [48–56]. Trainers for clinical assessment usually take the form of human-sized artificial robotic limbs with an actuated haptic joint (e.g., active [48,49] or passive [53]) that mimic a patient's joint affected by pathological muscle behaviors due to the underlying neurologic conditions. Existing trainers have mainly targeted mimicking common abnormal muscle behaviors such as spasticity [48–56], rigidity

(cogwheel and lead-pipe) [50–52,57], and clonus [54,55,58]. The simulated behaviors were created by modeling the neurologic diseases based on clinical data [48], clinical expert tuning [52], or a combination thereof [54]. However, in general, quantitative documentation of these abnormal kinematic and kinetic behaviors is lacking in the literature. In addition, a few studies have also evaluated the simulation realism of their proposed robotic trainers clinically by inviting a group of experienced clinicians and obtaining their subjective feedback on the task trainer performance. Such task trainers render a relatively realistic, consistent, and potentially scalable training environment for students, allowing learners to gain hands-on experience without the presence of real patients. However, to the best of the authors' knowledge, none of the previous research prototype trainers were commercialized nor adopted by medical training institutions beyond the authors' home institutions, possibly due to the device complexity, maintenance, or cost.

In order to render the desired haptic feeling to the user, some previous designs simply relied on the actuator to perform open-loop torque control, which often suffers from friction loss in the drivetrain [51,55]. On the other hand, to achieve better torque tracking, others used closed-loop torque control via the torque feedback from a six-axis force/torque sensor at the end effector [48,54]. However, the downside was the high cost and mechanical frailty of the sensor. Even though the delivery of accurate interaction torque under imposed disturbance (i.e., user's input motion) is a core challenge in the field of robotic task trainers, surprisingly there is a lack of discussion and reporting of the force/torque control scheme as well as the torque tracking performance in the literature, except for [122].

D. Review of Modeling and Control for Series Elastic Actuator (SEA)

Several modeling and control strategies have been proposed for series elastic actuators (SEAs) and evolved over the years. A single SEA robotic joint consists of two degrees of freedom

(DOFs), the actuator side DOF and the link side DOF (sometimes referred as the load side DOF), decoupled by a series spring. Due to the difficulty in accurately modeling the environmental dynamics on the link side, most previous works have modeled their SEA designs as 1-DOF dynamic systems (or a 1-mass system) and only considered the dynamics on the actuator DOF, by assuming that the link side DOF is fixed. Only a few works explicitly explored the link motion and environmental dynamics by modeling both the SEA and its output link via a 2-DOF dynamic system (or a 2-mass system) [123,124]. Most force control schemes were designed based on a 1-DOF dynamic model and considered the unknown environmental dynamics as a disturbance to reject. Popular controller choices included cascaded a PID controller [90,125], disturbance observer-based controller [123,126,127], adaptive controller [128], and acceleration-based controller [81,88]. Only a few model-based control schemes explicitly accounted for a 2-DOF system [123,129].

E. Study Overview

The goal of this study was to model three target abnormal muscle behaviors and design the control system for a previously developed SEA-based robotic arm trainer by our research group [57] to accurately deliver the appropriate muscle resistance response to the trainee (Fig. 4.2). A series of benchtop and clinical validation tests were conducted to verify the trainer's control performance as well as clinical realism.

4.2 Methods

A. Arm Trainer Mechatronic Design Overview

The robotic arm trainer used in this study is a 1-DOF kinesthetic haptic torque display device that resembles a human arm. The dimensions of the limb (upper arm, forearm, and hand) were matched with the anthropometric data of a 50th percentile Caucasian male [107]. The forearm

and hand (the moving segments) together have a mass of 0.91 kg and a moment of inertia of 0.046 kg.m2 around the elbow joint, which are lower than those of a biological counterpart (1.57 kg and 0.067 kg.m2). The ROM of the simulator was from 45º (fully flexed) to 150º (fully extended). More design details can be found in [57].

Fig. 4.2: A mock interaction between the learner and the task trainer.

B. Mathematical Modeling and Parameter Determination of Lead-pipe rigidity, Cogwheel rigidity, and Spasticity

In this study, three target behaviors for the arm task trainer were considered: lead-pipe rigidity (LR), cogwheel rigidity (CR), and spasticity (SP). The modeling of LR was inherited from [57], and the modeling of CR and SP are proposed in this work. In general, LR and CR are relatively simple to model, but it is more complex to model SP. This section describes how these behaviors were mathematically modeled at different severity levels and how their resulting

resistive muscle tones were calculated based on the user input kinematics (Fig. 4.3)[9].

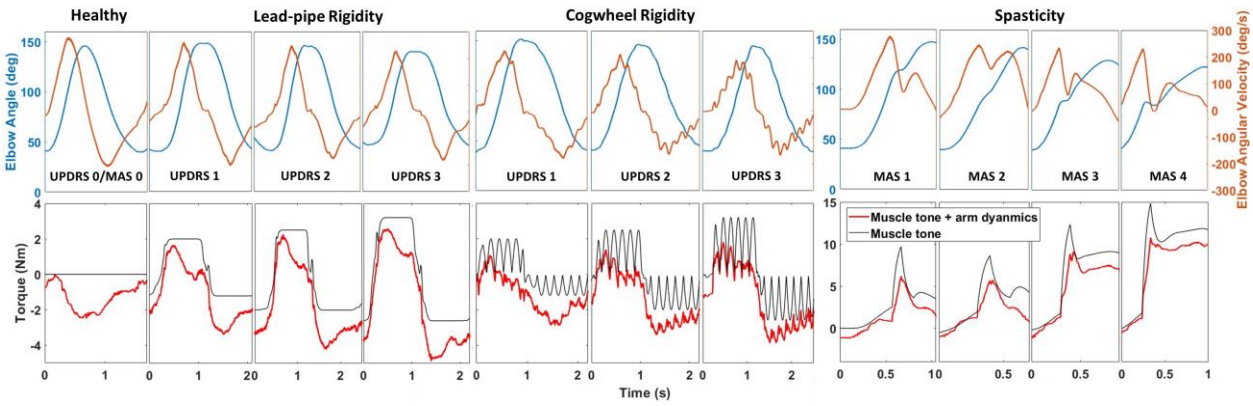

Fig. 4.3: Muscle kinematics and tone (torque) profiles for healthy, lead-pipe rigidity, cogwheel rigidity, and spasticity across severity levels given mathematical model and control parameters. These profiles were generated when a passive stretch test was performed on the task trainer arm. Only biceps spasticity results are shown. Triceps spasticity has similar profiles, and are omitted for clarity.

Lead-pipe Rigidity (LR)

In lead-pipe rigidity, once the clinician starts to move the patient's arm, a uniformly elevated muscle resistance will appear throughout the ROM and the resistance level tends to increase with the UPDRS score (Table 4.2). To command this step response-like constant resistance, a smooth transition of the torque (τ_{muscle}) from zero torque to an elevated torque level (at the UPDRS score being simulated) was implemented using a hyperbolic tangent function [57]

$$\tau_{muscle} = -\tau_{avg} tanh\left(\frac{\dot{\theta}_E}{\omega_{thresh}}\right) \tag{4.1}$$

where elbow angular velocity is $\dot{\theta}_{elbow}$, the clinically-derived average muscle tone is τ_{avg}, and a threshold velocity constant is ω_{thresh}. Note that ω_{thresh} determines the velocity at which τ_{ref} will approach to the desired value of τ_{avg}, which was set to be 66 °/s [57]. To extract τ_{avg} for each

[9] Positive torque is a torque applied in the direction of elbow flexion (resisting extension motion) and vice versa.

UPDRS score, we initially referred to the clinical data from [130] in the design phase [57] and the magnitudes of τ_{avg} were further iterated during a clinical validation study with a group of 11 experienced clinicians [131]. Since gravity assists the stretch motion in extension, but resists it in flexion, the values were adjusted to be higher for extension to partially offset the effect of gravity ($\tau_{avg} = 1.2, 2.0, 2.6$ Nm for flexion and $\tau_{avg} = 2.0, 2.5, 3.2$ Nm for extension for UPDRS 1 to 3, respectively).

Cogwheel Rigidity (CR)

To model cogwheel rigidity, the simulated muscle tone generated by the proposed LR model was turned on and off intermittently by a rectified sinusoidal function with a tremor frequency of ω.

$$\tau_{muscle} = -\tau_{avg} tanh\left(\frac{\dot{\theta}_E}{\omega_{thresh}}\right)|sin\,(\omega t)| \tag{4.2}$$

The tremor frequency ω for cogwheel rigidity has been reported to vary between 6-9 Hz in the literature [119], and we used ω = 6 Hz to model this behavior in our arm trainer. For practical implementation, an exponential moving average filter (with a forgetting factor[10] of 0.75) was used to smooth the commanded signal.

Spasticity (SP)

We started with the spasticity model proposed in Park et al. [48] as the baseline model since it is one of the few published works that modeled SP mathematically. Park et al.'s piecewise model divided the SP resistance response into three phases: a) pre-catch, b) catch, and c) post-catch, where a separate governing equation was used to model each phase (Fig. 4.4). For

[10] In recursive filters, a forgetting factor gives exponentially less weight to older samples [152].

controlling the trainer, τ_{muscle} would be set to the following torque terms based on the phase.

(1) ***Pre-catch phase***

The pre-catch muscle tone (τ_{pre}) was modeled as a mildly damped feeling added to the arm dynamics.

$$\tau_{pre} = b_{pre}\dot{\theta}_E \tag{4.3}$$

where b_{pre} is the pre-catch damping coefficient and $\dot{\theta}_E$ is the joint angular velocity. This model implies that during the pre-catch phase, minimal abnormal muscle tone appears.

The pre-catch phase will transit to the catch phase when the arm reached a certain joint angle called the catch angle (θ_{catch}). θ_{catch} is specified in the real time based on the average joint angular velocity during the pre-catch phase. Note that SP is a stretch-velocity dependent behavior, so if the arm is moved very slowly (less than a certain threshold speed, v_L), θ_{catch} will be set as an unreachable angle and no catch will occur. Therefore, θ_{catch} was expressed as

$$\theta_{catch} = \begin{cases} \text{no catch} & \text{if } \dot{\theta}_{pre\_avg} < v_L \\ \theta_{catch\_MAS} & \text{if } \dot{\theta}_{pre\_avg} \geq v_L \end{cases} \tag{4.4}$$

In this study, a constant catch angle for each MAS level was assumed for simplicity. $\dot{\theta}_{pre\_avg}$ is the average arm stretch speed during the pre-catch phase and $v_L = 60$ °/s based on [48].

(2) Catch phase

The torque during the catch phase was expressed as

$$\tau_{catch} = \tau_{pre\_end} + H\dot{\theta}_{catch\_init}\delta(t) \tag{4.5}$$

$$\text{with } \delta(t) = \begin{cases} 1 & if\ t - t_{catch\_init} < \Delta T_{catch} \\ Q\ (Q < 1) & if\ t - t_{catch\_init} \geq \Delta T_{catch} \end{cases}$$

where τ_{pre_end} is the torque at the end of the pre-catch phase, H and Q are parameters that determine the catch amplitude ($H\dot{\theta}_{catch\_init}$) and release amplitude ($H\dot{\theta}_{catch\_init}Q$), respectively (Fig. 4.4) and vary across different MAS levels, $\dot{\theta}_{catch\_init}$ is the elbow stretch speed at the beginning of the catch phase, t_{catch_init} is the time when the catch phase initiates, and ΔT_{catch} represents the catch duration and is given by $\Delta T_{catch} = \frac{D}{\dot{\theta}_{pre\_avg}}$, where D is a heuristically determined constant that specifies the catch duration. The model structure for this phase was adopted from Park et al., but the control parameters were retuned based on our clinical data (Chapter 5 and [130]).

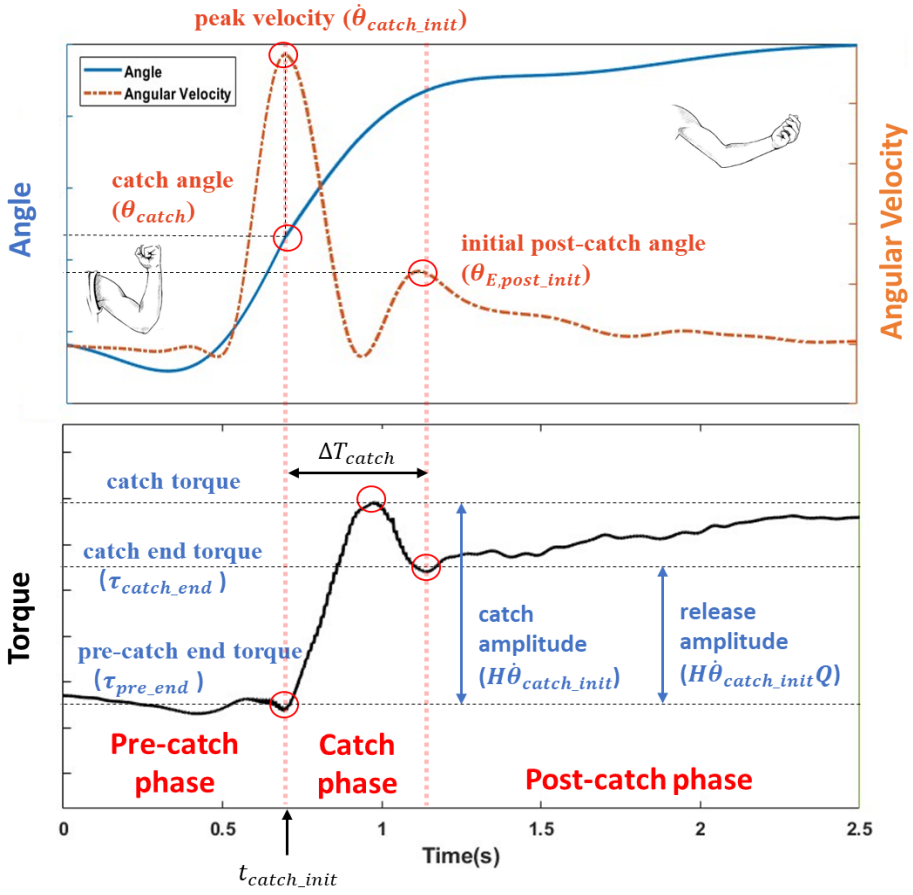

Fig. 4.4: A sample extension trial to illustrate different phases of biceps spasticity muscle tone profile and definitions of key simulation parameters.

(3) Post-catch phase

The post-catch torque was modeled as the impedance with a virtual spring and a damper:

$$\tau_{post-catch} = k_{post}(\theta_E - \theta_{E,post_{init}}) + b_{post}\dot{\theta}_E\, \tau_{catch-end} + k_{ROM}\,(\theta_E - \theta_{ROM}) + b_{ROM}\dot{\theta}_E \quad (4.6)$$

where k_{post} is the post-catch stiffness, b_{post} is the post-catch damping coefficient, $\theta_{E,post\_init}$ is the elbow angle at the beginning of the post-catch phase, θ_{ROM} is the elbow angle at the end of ROM for each MAS level (Table 4.1), and $\tau_{catch-end}$ is the torque at the end of the catch phase. $\tau_{catch-end}$ was included as a torque continuity term between catch and post-catch phases. Furthermore, if the elbow angle exceeded the prescribed ROM, a software bumper was implemented in the controller as a very stiff impedance control to limit the ROM for each MAS score (i.e., $k_{ROM} = 0.3$ Nm/° and $b_{ROM} = 0.05$ Nm/°/s).

(4) Arm reset phase

For a given practice condition, the arm trainer was configured to replicate spasticity in only one muscle group at a time (i.e., spasticity in only the biceps or only the triceps). Therefore, when the user was resetting the arm to the starting position for the next trial (most flexed or extended position, respectively), the muscle resistance was set to go exponentially to zero.

$$\tau_{reset} = \tau_{terminal}\, e^{-\beta t} \quad (4.7)$$

where t is time, $\tau_{terminal}$ is the magnitude of the torque right before the user reverses the motion of the arm, and β determines how fast the torque decays to zero ($\beta = 120$ s^{-1}).

(5) Spasticity parameter determination

Among three abnormal muscle behaviors, SP had the most complex model and the greatest number of control parameters. For each MAS level, Park et al. identified the spasticity parameters based on clinical data collected from four child spasticity subjects (one subject per each MAS level). However, due to the relatively small sample size and their underage subjects, we used spasticity parameters from two clinical studies datasets collected by our research group (Chapter 5 and [130]) and compared with Park et al.'s original values.

Song et al. tested 15 adult spasticity subjects (6 males, 9 females) in both elbow flexion and extension movements each for three trials and at four different speeds, i.e., slow (5-20 º/s), medium (20-80 º/s), fast (> 80 º/s), and the clinician's preferred speed) [130]. Additionally, in an ongoing study described in Chapter 5, 10 adult spasticity subjects (7 males, 3 females) have been assessed while performing both elbow flexion and extension trials at two different speeds (slow (< 30 °/s) and the clinician's preferred speed).The inclusion/exclusion criteria for using the clinical data from both studies were: a) subjects with elbow contracture who had very high catch muscle tones were excluded from testing, b) trials without any catch or with very little catch were also excluded, and c) only the trials performed at the clinician's preferred speed were used to determine the control parameters.

To extract the muscle tone response, the torques due to forearm gravity and inertia were removed from the clinically-measured torque during post-processing. Combining the data from both studies and from both biceps and triceps, for each spasticity subject, all parameters were calculated and averaged across all valid trials. Finally, the calculated parameters were averaged for each MAS level, and the average and standard deviation of the calculated values were computed. Figure 4.4 is a sample extension trial of a MAS 2 spasticity subject at the clinician's

preferred speed (from the study in Chapter 5) to illustrate our definitions of spasticity control parameters extracted from the clinical data. The catch angle was defined as the joint angle corresponding to the peak angular velocity (i.e., θ_{catch} = 109 ° ± 13.1 °, 75.5° ± 8.7°, 82.1° ± 10.5°, 76.8° ± 1.1 ° for MAS 1-4). To extract H, the catch amplitude was first calculated as the difference between the catch and pre-catch torques, which represents $H\dot{\theta}_{catch_{init}}$, and then was divided by the peak angular velocity (approximating $\dot{\theta}_{catch_{init}}$) (i.e., H =1.73 ± 0.61, 1.67 ± 0.75, 2.49 ± 1.17, 3.81 ± 1.58 Nm/°/s for MAS 1-4). Q was calculated by first taking the difference between the release torque and the pre-end torque, which equals to $Q \times \left(H\dot{\theta}_{catch_{init}}\right)$ and then, dividing it by $H\dot{\theta}_{catch_{init}}$ (i.e., Q =0.71 ± 0.08, 0.67 ± 0.12, 0.71 ± 0.02, 0.65 ± 0.23 for MAS 1-4).

In parallel with extracting SP parameter from clinical datasets, two experienced clinicians (a physical therapist and a neurologist, both with 20+ years of experience) were invited and asked to perform extension trials at their preferred speed to provide expert tuning on SP parameters for each MAS score. They evaluated the simulated SP behaviors based on the parameters from Park et al.'s study [48] and adjusted the parameters on the fly. The H values suggested by the clinicians were quite close to the values reported in Park et al.'s study, as well as the clinical values. (i.e., $H_{clinician}$ = 1.5, 1.9, 2.8, 3.7 Nm/°/s and H_{park} = 1.4, 2.0, 2.8, 3.8 Nm/°/s for MAS 1-4) and the Q values were smaller (i.e., $Q_{clinician}$ = 0.075, 0.15, 0.4, 0.5 and Q_{park} = 0.15, 0.30, 0.6, 0.8 for MAS 1-4).

Eventually, all three sources of information (i.e., clinical datasets, preliminary expert tuning, and original values from Park et al.) were considered to finalize the control parameters for spasticity simulation. Values of H and catch angle were extracted heuristically considering the two datasets and clinician's preliminary feedback. On the other hand, Q values from the clinical studies

were much higher compared to the values suggested by the clinicians for MAS 1 and 2 but were more similar for MAS 3 and 4. Note that the clinicians also indicated that for MAS 1 and 2, there should be a large release in torque after catch which implied that *Q* should be very small. Therefore, we adopted the *Q* values determined by the clinicians. For the ROM, clinicians mentioned that a full ROM should be observed except for MAS 4. Therefore, θ_{ROM} was set to be 150 º for MAS 1-3 and 130 º for MAS 4. k_{post} values were also tuned based on the input from the clinicians (zero for MAS 1 and 2 to render minimal resistance at the end of ROM). All control parameters were summarized in Table 4.1.

Table 4.1. Summary of spasticity parameters. $\bar{\theta}_{catch}$ and *H* used by the trainer, based on data extracted from two clinical datasets (Chapter 5 and [130]) . *Q*, θ_{ROM}, and k_{post} were tuned by clinicians. *D* was adopted from Park et al. [48].

MAS	θ_{catch} (°)	H $(Nm/°/s)$	Q	θ_{ROM} (°)	D	k_{post} $(Nm/°)$
1	110	1.8	0.075	150	60	0
2	80	1.8	0.15	150	50	0
3	80	3	0.4	150	30	0.05
4	80	3.8	0.5	130	25	0.05

C. System Modeling and Control Design

The control system consisted of high-level and low-level control schemes (Fig. 4.5). To replicate the target abnormal muscle behavior and patient's arm dynamics, the high-level controller calculated the desired reference interaction torque felt by the user (τ_{user}^{d}):

$$\tau_{user}^{d} = \tau_{muscle} + \tau_{dyn} \tag{4.8}$$

where τ_{muscle} is the simulated muscle tone for a selected behavior, and τ_{dyn} is the simulated torque due to the patient's arm dynamics calculated based on the 50th percentile human forearm inertia and gravity when driven by the user's input motion. This desired torque command was then input

to the low-level control, which consisted of three controllers: a cascaded PI feedback controller (C_{FB}), a model-based feedforward controller (C_{FF}), and a disturbance observer (C_{DOB}). This low-level control was motivated by the needs of compensating for the mass and inertia mismatch between robotic and real patient's forearms, as well as rejecting the external disturbance from user interaction. The actual interaction torque between the arm trainer and the user (τ_{user}) was estimated based on the torque measured by the series springs in the SEA with corrections using the knowledge of the robotic forearm mass and inertia properties ($\hat{\tau}_{user}$).

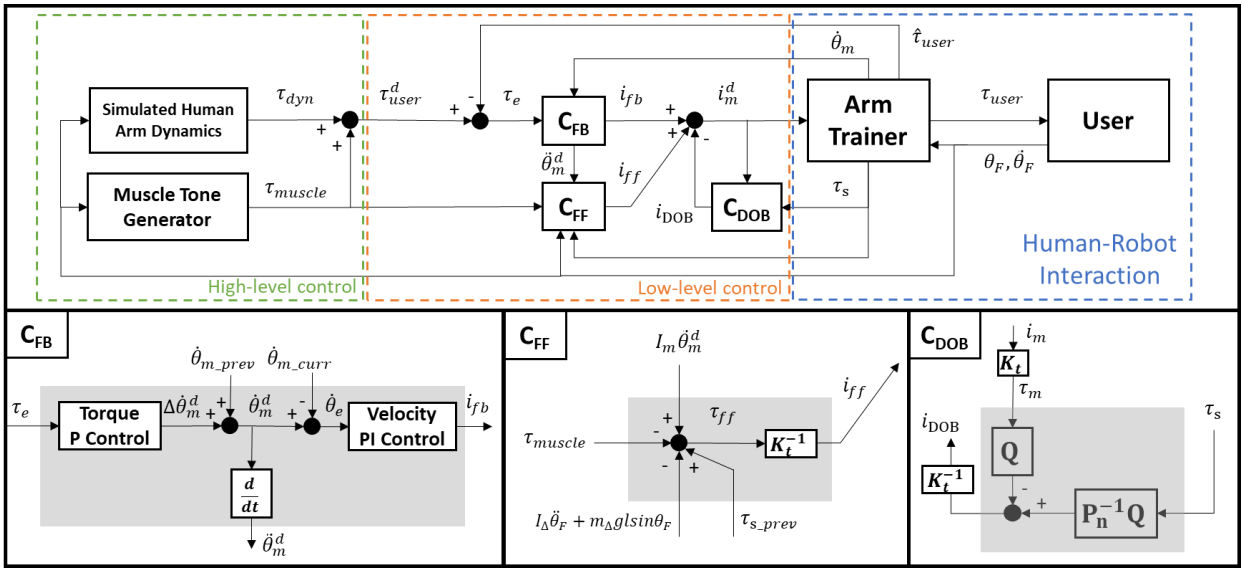

Fig. 4.5: (Top) Control system block diagram of the arm trainer and interaction with the human user. (Bottom) The details of the block diagram of each controller shown individually with corresponding inputs and outputs. FB: feedback, FF: feedforward, DOB: disturbance observer. Symbols are defined in the text.

Feedback controller

The initial control design started with a cascaded PI feedback controller (innermost to outermost loop: current, velocity, and torque control) (Fig. 4.5, C_{FB}), inherited from our previously developed ankle-foot robotic task trainer (Chapter 2 and [58]). There were two design considerations. First, the purpose of the extra middle velocity loop was to form a tight encoder-based velocity feedback around the motor to fight against stiction and backlash in the motor and

its gearbox. This implementation was similar to [132,133], which is often referred as velocity-sourced SEA control. Second, the reference motor velocity ($\dot{\theta}_m^d$) was calculated by summing the measured motor velocity in the previous time step ($\dot{\theta}_{m\_prev}$) with a desired change of velocity ($\Delta\dot{\theta}_m^d$) obtained in the outer torque control loop based on the interaction torque error (τ_e). Essentially, the torque control loop only specified the change of motor velocity on top of the current velocity, rather than commanding a completely new velocity set point. This technique helped smooth out the reference velocity trajectory and also effectively reduced the effect of external link motion disturbance driven by the user, in the same spirit of "load motion compensation" suggested in [88,124]. However, given the nonnegligible mass and inertia difference between the robotic forearm and the human forearm, this controller alone was less effective compared to its original implementation on the ankle-foot trainer, so additional controllers were introduced.

Feedforward controller

To account for the mass and inertia discrepancy between the human arm and arm trainer, a 2-DOF dynamic model of the arm trainer was established to guide the design of the components in a feedforward control effort (Fig. 4.5, C_{FF} and Fig. 4.6). For clarity and without loss of generality, the drivetrain gear ratio was ignored in the model (but was implemented in the actual controller). Friction and damping at the motor gearbox and at the elbow joint were not modeled and assumed to be mostly removed by the feedback control. The equations of motion for the motor output torque (τ_m) and the user's applied torque, i.e., also the user felt torque (τ_{user}) were derived as:

$$\tau_m = I_m\ddot{\theta}_m + k_s(\theta_m - \theta_F) \tag{4.9}$$

$$\tau_{user} = I_T\ddot{\theta}_F + k_s(\theta_F - \theta_m) + m_T g l cos\theta_F \tag{4.10}$$

where θ_F and $\ddot{\theta}_F$ are the forearm segment angle and acceleration, θ_m and $\ddot{\theta}_m$ are the motor shaft angle and acceleration, k_s is the series spring stiffness, I_m is the reflected motor rotor inertia, m_T and I_T are the mass and moment of inertia (around the elbow) of the task trainer's forearm, and l is the distance between the elbow and forearm center of mass. By combining (4.9) and (4.10), the user felt torque was obtained as

$$\tau_{user} = I_T\ddot{\theta}_F + I_m\ddot{\theta}_m - \tau_m + m_T g l cos\theta_F. \tag{4.11}$$

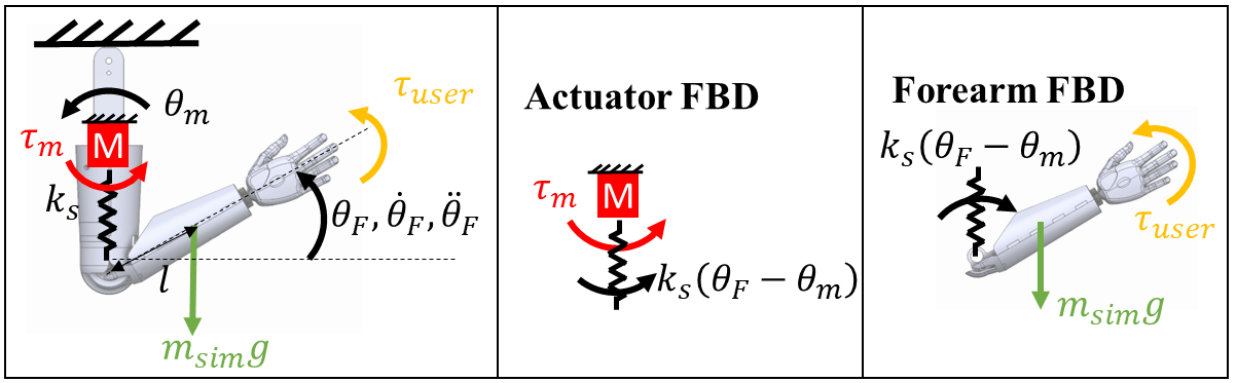

Fig. 4.6: Free body diagrams of the robotic task trainer.

The torque due to simulated arm dynamics was defined as

$$\tau_{dyn} = I_H\ddot{\theta}_F + m_H g l cos\theta_F \tag{4.12}$$

which consists of the torque due to the human forearm inertia ($I_H\ddot{\theta}_F$) and gravity ($m_H g l cos\theta_F$). I_H (0.071 kgm^2) and m_H (1.63 kg) values are 50th percentile human forearm moment of inertia and mass [108].

Considering that the mass and inertia of the task trainer's forearm were less than that of an actual human forearm, two positive constant terms were defined as $I_\Delta = I_H - I_T$ and $m_\Delta = m_H -$

m_T. Therefore, since the goal was to minimize the error between the user felt torque (τ_{user}) and the desired torque (τ_{user}^d) to achieve a good torque tracking performance, by setting $\tau_{user} = \tau_{user}^d$, the feedforward torque command to the motor was strategically chosen as

$$\tau_{m\_ff} = -I_\Delta \ddot{\theta}_F - m_\Delta g l cos\theta_F + I_m \ddot{\theta}_m - \tau_{muscle}. \quad (4.13)$$

Equation 4.13 motivated the structure of the feedforward controller. The following signals were fed forward: reference muscle tone profile (τ_{muscle}), motor inertia compensation ($I_m \ddot{\theta}_m$), and the torques used to render the gravity and inertia difference between the task trainer and the real human arm. To implement this feedforward law practically, to calculate the motor inertia compensation, motor reference acceleration ($\ddot{\theta}_m^d$) was used (instead of the actual motor acceleration $\ddot{\theta}_m$) to obtain a smoother signal. In addition, θ_F was approximated by the absolute encoder reading on the actuator side and $\ddot{\theta}_F$ was obtained via double differentiation of θ_F. In addition to these feedforward terms in (4.13), the spring torque in the previous time step (τ_{s_prev}) was also fed forward to maintain the current interaction torque similar to the use of $\dot{\theta}_{m\_prev}$ described above. This approach also minimized the feedback control effort to compress the spring [133]. Given the inevitable unmodeled dynamics and model mismatch, the residual torque error between τ_{user} and τ_{user_d} will always exist and were dealt with by the feedback control. τ_{m_ff} was then converted to feedforward current command (i_{ff}) through the motor torque constant (K_t).

Disturbance Observer

A disturbance observer (DOB) is a simple and effective robust control scheme that has been widely used in industrial motion control [134]. Since the SEA converts the force control problem into a position control problem by using the motor torque to modulate the spring

deflection, DOB has become a popular technique for SEA control especially when there is a need to minimize the effect of internal and external disturbances [123,126,135,136].

The implementation of a DOB involved specifying a nominal plant (P_n) and a low-pass filter (Q_{LP}) (Fig. 4.5, C_{DOB}). Intuitively, a DOB compares the reference motor torque and the estimated motor torque, calculated using the series spring torque and the inverse nominal plant, and then compensates the difference due to various sources of disturbance. The low-pass filter determines up to which frequency the disturbance would be rejected and also makes $P_n^{-1}Q_{LP}$ realizable [134]. To obtain the nominal plant transfer function, a system identification process was conducted. The forearm was fixed in a 90° joint angle configuration and the motor was operated in a current-control mode given a chirp current signal with an amplitude of 1 A and frequency changing from 0.1 – 10 Hz. The torque estimated by the series spring was also recorded. The open-loop plant (P_{ol}) was fitted (System Identification Toolbox v9.13, MATLAB 2022a) with a transfer function from the geared motor torque ($N\tau_m$, where N = 5) to spring torque (τ_s) with mechanical efficiency (η < 100 %).

$$P_{ol}(\mathrm{s}) = \frac{\eta\tau_s(s)}{N\tau_m(s)} = \frac{\eta}{N}\frac{N\omega_n^2}{s^2+2\omega_n\zeta s+\omega_n^2} = \frac{312.5}{s^2+9.945s+366.4} \tag{4.14}$$

From (4.14), the system identification results suggested an open-loop natural frequency (ω_n) of ~3 Hz and an efficiency of ~85 %. To track a torque command up to 6 Hz (i.e., the case of CR), DOB in the inner loop was implemented to shape the existing plant into a faster plant to facilitate outer loop control [123,134]; thus, the nominal plant was selected to have a natural frequency of 8 Hz (4.15).

$$P_n(\mathrm{s}) = \frac{2524}{s^2+13s+2524} \tag{4.15}$$

The low-pass filter was designed to be a second-order Butterworth filter with a cut-off frequency of 15 Hz, which was the highest cut-off frequency allowed by the trainer hardware.

$$Q_{LP}(s) = \frac{8883}{s^2+133.3s+8883} \tag{4.16}$$

Interaction torque estimation

One advantage of the SEA is the ability to use series spring deflection to estimate the interaction force or torque, instead of using an expensive external force/torque sensor. If rearranging (4.10), note that the torque estimated by the series spring (τ_s) did not directly measure the torque felt by the user, since it also contained gravitational and inertial torques of the trainer's forearm (4.17).

$$\tau_s = k_s(\theta_F - \theta_m) = \tau_{user} - I_T\ddot{\theta}_F - m_T g l cos\theta_F \tag{4.17}$$

$$\hat{\tau}_{user} = \tau_s + I_T\ddot{\theta}_F + m_T g l cos\theta_F \tag{4.18}$$

As a result, instead of directly feeding the series spring torque back as the measured interaction torque, the estimated forearm's gravitational and inertial torques were first compensated based on the series spring torque to calculate the estimated user felt torque ($\hat{\tau}_{user}$) as in (4.17) and then the error between $\hat{\tau}_{user}$ and τ_{user}^d would be the input to the feedback controller (Fig. 4.7).

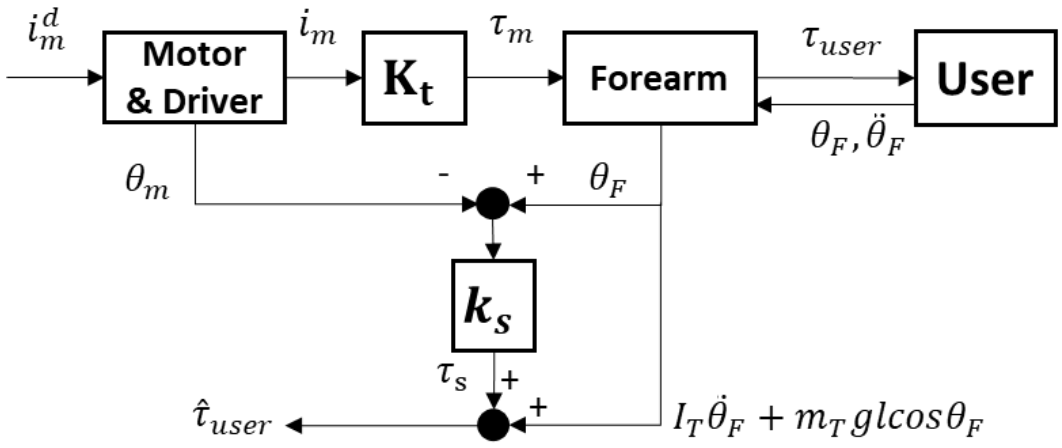

Fig. 4.7: Diagram of SEA's interaction torque estimation scheme.

D. Evaluation Protocol

Benchtop Evaluations

Torque estimation verification test

Benchtop tests started with verifying the interaction torque estimated by the series spring. The actual user felt torque (τ_{user}) was measured by a shear force load cell (20 kg, CZL635, Phidgets Inc., Canada) installed between the trainer's forearm and user (Fig. 4.8). Due to the presence of the load cell, the forearm shroud and hand were removed. To roughly match their mass and inertia, a weight of 2 lb (0.91 kg) was rigidly attached to the forearm. Based on (4.18), to compute the estimated user felt torque ($\hat{\tau}_{user}$), the mass and inertia of the task trainer's forearm (m_T = 1.41 kg, I_T = 0.040 kg·m^2) were obtained from the CAD model, and the spring torque (τ_s), forearm segment angle (θ_F) and acceleration ($\ddot{\theta}_F$) were collected from onboard sensors. The test protocol involved manually moving the trainer's forearm throughout the 150° ROM within 1 s for three trials (holding the handle tip with a fixed 27 cm moment arm). To evaluate the interaction torque estimation accuracy, the root mean squared error (RMSE) between $\hat{\tau}_{user}$ and τ_{user} was calculated. Note that after this test, the load cell and the additional weight were removed, and the forearm shrouds and hand were reinstalled. m_T and I_T were rederived from CAD model accordingly, which were 0.91 kg and 0.046 kg·m^2.

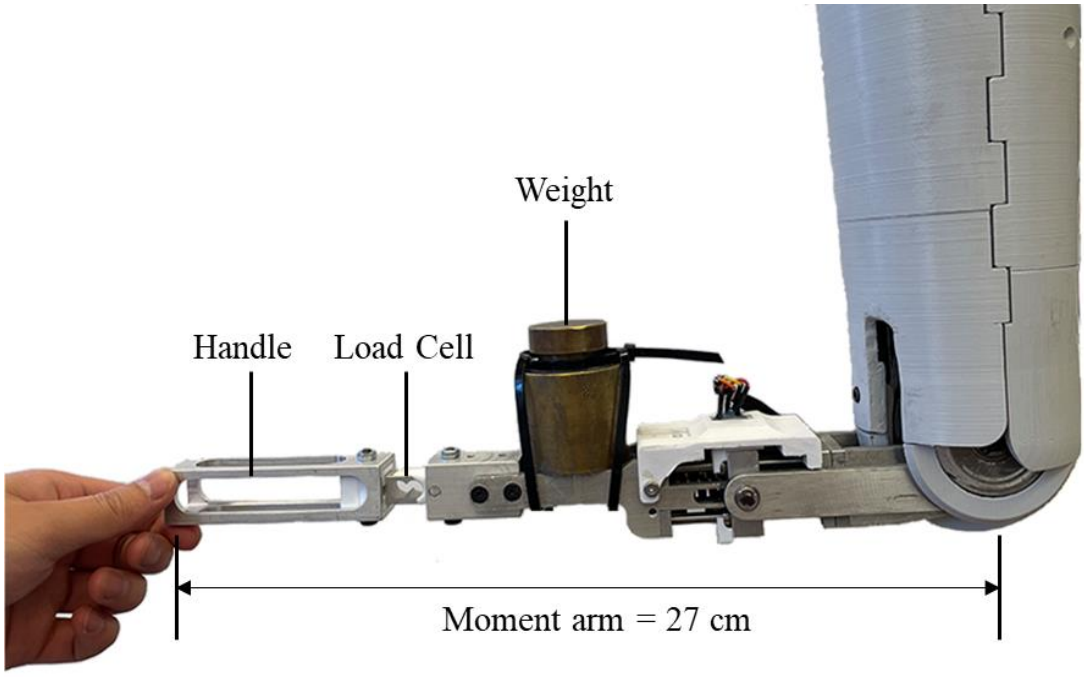

Fig. 4.8: Experimental setup for torque estimation verification test.

Torque tracking accuracy test

The proposed control system was tested to evaluate its performance on delivering the desired interaction torque to the user (τ_{user}^{d}). To understand the effectiveness of each controller, an ablation study was conducted to examine the tracking performance of four controller settings: a) feedback control only (C_{FB}), b) both feedback and feedforward control ($C_{FB} + C_{FF}$), c) feedback control, feedforward control, and disturbance observer ($C_{FB} + C_{FF} + C_{DOB}$), and d) same as case c but with higher feedback gain ($C_{FB} + C_{FF} + C_{DOB}$ with high gain). In case d, note that with the addition of the C_{FF} and C_{DOB}, the torque loop P gain in C_{FB} could be further increased. For each setting, the investigator performed the passive stretch test by mimicking the standard clinical technique (moving the arm through the ROM within 1 s) on the arm trainer to assess the simulated behavior for three trials. This procedure was repeated for each behavior across severities (3 UDPRS scores for LR, 3 UPDRS scores for CR, and 4 MAS scores for biceps and triceps SP, shown in Fig. 4.2). For each trial, to verify the torque tracking accuracy, the RMSE was calculated

throughout the ROM (extension only for SP; both extension and flexion for LR and CR) and then averaged across three trials with standard error (SE) reported. Additionally, the percentage errors were calculated as $\frac{averaged\ RMSE}{|maximum\ torque|} \times 100\ \%$, where the maximum torque was extracted from the thick red curve (muscle tone + arm dynamics) in Fig. 4.3.

Clinical Expert Evaluations

Test protocol

To validate the realism of the task trainer in mimicking the three behaviors, a validation evaluation was conducted to get feedback from clinical experts in spasticity and rigidity assessment. The study was approved by the Institutional Review Board at University of Illinois at Urbana-Champaign and informed consent was obtained from all subjects. The study was conducted in the Jump Simulation and Education Center in Peoria, IL with a total of seven subjects (Table 4.2).

Table 4.2: Subject demographic information

Subject ID	Medical Education	Yrs of LR&CR Practice	Yrs of SP Practice	# of LR&CR Patients /Month	# of SP Patients /Month
1	MD[1]	8	8	0	42
2	PGY4[2], MD	3	3	1 or 2	1 or 2
3	BS PT[3]	15	15	≤ 1	2-4
4	DO[4]	11	8	3	150
5	MD	15	15	10-20	10-20
6	MBBS[5], MD	3	3	190	1 to 2
7	MD	10	10	10-20	5

[1] Doctor of Medicine, [2] Postgraduate Year Four (PGY-4) of Residency, [3] Bachelor of Science in Physical Therapy,[4] Doctor of Osteopathic Medicine, [5] Bachelor of Medicine, Bachelor of Surgery.

Before starting the study, written descriptions of UPDRS and MAS scores were provided to the subject. The clinical evaluation consisted of a Classification Test (CT) and a Disclosed Assessment Test (DAT). During the CT, the arm was configured to replicate all 15 different conditions (i.e., healthy, LR UPDRS 1-3, CR UPDRS 1-3, biceps SP MAS 1-4, and triceps SP

MAS 1-4), one trial per condition and in total 15 trials each in randomized sequence (using Random Module in Python 3.9). Without knowing the condition being simulated, the subject was asked to assess each trial to classify the behavior and evaluate its severity based on their prior clinical experience. They were instructed to always start the passive stretch test from the fully flexed joint position and to check both biceps and triceps conditions.

During the DAT, the investigator walked the subject through all 15 simulated conditions (disclosed to the subject). The subject provided qualitative feedback on simulation realism of each replicated behavior, and attitude toward the potential of this device as a medical education task trainer by answering multiple five-point Likert questions (Table 4.3).

Table 4.3. DAT feedback questions. 5-point Likert scale for a) simulation realism: 1-too little, 3-about right, 5-too much; b) general usefulness: 1-strongly disagree, 3-neutral, 5-strongly agree.

Simulation Realism Questions	
Behavior	**Assessment Metrics**
LR	resistance magnitude, range of motion
CR	cogwheel frequency, cogwheel magnitude
SP (biceps + triceps)	catch angle location, catch tone amplitude, release tone amplitude, post-catch tone amplitude, range of motion
General Usefulness Questions	
As an educational tool for healthcare learners to practice rigidity and spasticity assessment techniques	

Data analysis

For the CT, the judgements from subjects were plotted against the trainer's setup using a confusion matrix to determine if subjects could distinguish the behaviors (LR, CR, and SP). The classified percentage was calculated as $\frac{\#\ of\ classified\ trials}{\#\ of\ total\ trials} \times 100\ \%$ for each behavior. Any trend

of mismatch on behavior severity was noted to be justified later by DAT results. For the DAT, the mean and standard error were calculated for each simulation aspect.

4.3 Results

A. Benchtop Validation

Torque estimation verification test

Three trials were manually conducted (average peak speed of 166 ± 3.4°/s) and the RMSE between $\hat{\tau}_{user}$ and τ_{user} remained low (0.16 Nm) across three trials (Fig. 4.9). This result validated the interaction torque estimation based on spring torque (τ_s) and forearm mass and inertia (m_T, I_T) as in (4.18).

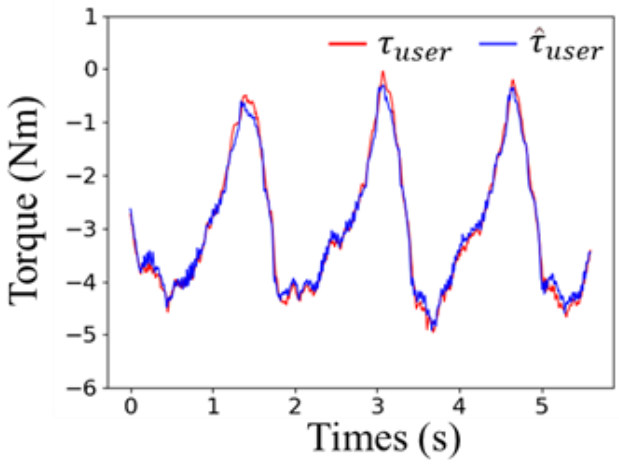

Fig. 4.9: Torque estimation verification test results.

Torque tracking accuracy test

Four different controller settings, i.e., C_{FB} only, $C_{FB} + C_{FF}$, $C_{FB} + C_{FF} + C_{DOB}$, and $C_{FB} + C_{FF} + C_{DOB}$ (HG), were tested. As more controller blocks were involved, the tracking performance was significantly improved for all behaviors (Table 4.4 and Fig. 4.10). The incorporation of feedforward control significantly improved the tracking performance by 17-49 %

from the baseline feedback controller (i.e., C_{FB} only). Furthermore, the addition of DOB further reduced the tracking error for SP and CR trials by 23-43 % compared to $C_{FB} + C_{FF}$. Eventually, with $C_{FB} + C_{FF} + C_{DOB}$ (HG), the tracking performance was again improved by 16-36 % compared to $C_{FB} + C_{FF} + C_{DOB}$. These results led us to use the $C_{FB} + C_{FF} + C_{DOB}$ (HG) controller.

Table 4.4: Torque tracking accuracy test results. Mean (SE) of RMSE for controller settings across behaviors (SP, LR, and CR) and severities (MAS and UPDRS). Unit: Nm.

		Controller			
		FB	**FB+FF**	**FB+FF+DOB**	**FB+FF+DOB (HG)**
Spasticity (MAS)	**1**	0.357 (0.011)	0.268 (0.004)	0.190 (0.013)	0.122 (0.007)
	2	0.336 (0.004)	0.263 (0.010)	0.188 (0.011)	0.122 (0.010)
	3	0.469 (0.019)	0.388 (0.010)	0.293 (0.005)	0.212 (0.004)
	4	0.662 (0.025)	0.410 (0.008)	0.314 (0.011)	0.236 (0.013)
Lead-pipe Rigidity (UPDRS)	**1**	0.135 (0.004)	0.098 (0.002)	0.084 (0.003)	0.069 (< 0.001)
	2	0.162 (0.005)	0.108 (0.004)	0.090 (0.001)	0.070 (< 0.001)
	3	0.156 (0.001)	0.106 (0.002)	0.103 (0.008)	0.087 (0.008)
Cogwheel Rigidity (UPDRS)	**1**	0.333 (0.023)	0.170 (0.009)	0.122 (0.001)	0.094 (0.002)
	2	0.293 (0.018)	0.237 (0.004)	0.163 (< 0.001)	0.111 (0.003)
	3	0.396 (0.018)	0.335 (0.031)	0.192 (0.006)	0.132 (0.004)

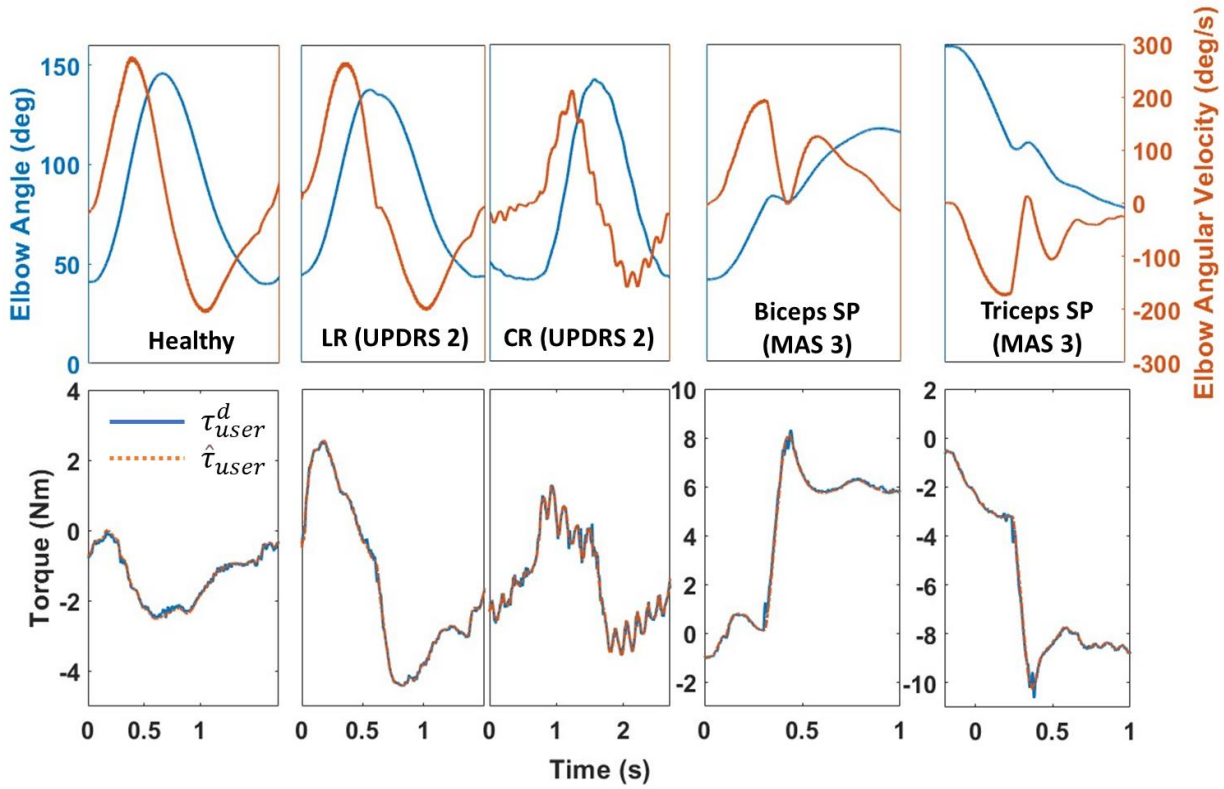

Fig. 4.10: Sample tracking results for typical SP, CR, and LR behaviors using the $C_{FB} + C_{FF} + C_{DOB}$ with high gain controller.

B. Clinical Expert Validation

Each subject went through a CT and a DAT during the clinical session. During the CT, it was noticed that Subjects 4 and 7 had different assessment patterns compared to others. Specifically, Subject 4 tended to make very quick assessments (i.e., often only performed a single passive stretch per trial and then made a judgment), while other subjects usually performed the stretch multiple times and took time to consider the simulated muscle tone behavior and severity. Subject 7 used a less standard technique, i.e., using one hand to casually move the trainer's arm without stabilizing the elbow/upper arm with another hand. Based on these observations, these two subjects were marked as potential outliers in the data analysis, and we calculated the classified percentages in the CT with and without Subjects 4 and 7. On the other hand, during DAT when

these two subjects carefully assessed the trainer same as other subjects, their feedback were consistent with the rest of the group, so their feedback were included in DAT data analysis (see Appendix A).

Based on CT results, on average, subjects were able to distinguish three different behaviors with an accuracy of 87% (or 92% if excluding Subjects 4 and 7), suggesting that the simulated SP, LR, and CR behaviors were distinctive (Fig. 4.11). Note that 10 of 16 misclassified trials (e.g., the off-diagonal entries in the confusion matrix) were found due to Subject 4 (6 trials) and 7 (4 trials), and the remaining 6 were scattered across the other five subjects (see Appendix A for the confusion matrix of individual subjects). For rigidity, severity agreement was in general satisfactory. For

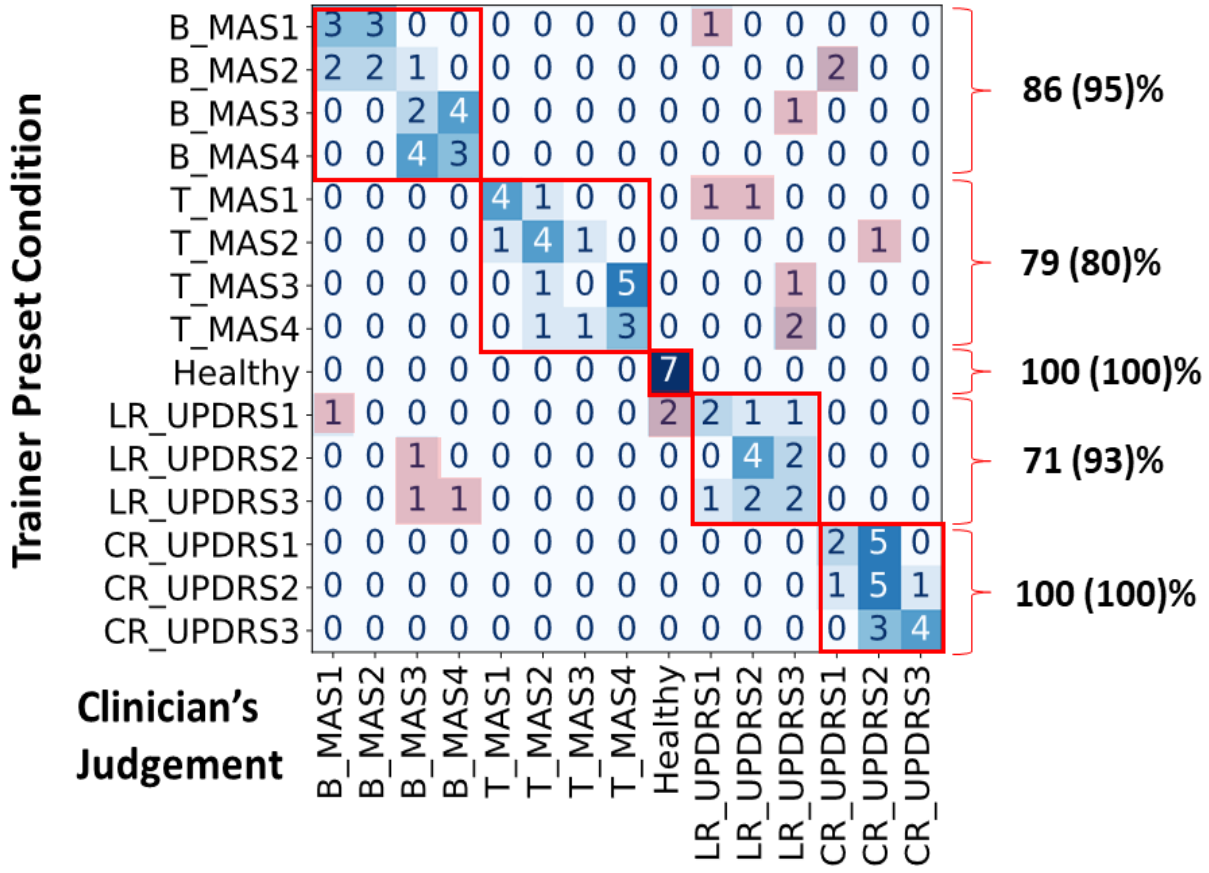

Fig. 4.11: Classification Test results reported in a confusion matrix (values in the matrix were the frequency of judgement), with correctly classified percentages reported (values in parentheses are without Subjects 4 and 7). Submatrices in red boxes indicated separate behaviors (LR, CR, Biceps-SP, Triceps-SP, and healthy).

spasticity, severity agreement matched with regular qualitative clinical assessment accuracy of interest, where mild (MAS 1 and 2) and severe (MAS 3 and 4) SP trials were mostly separated, and some trials were mixed within the severity group.

DAT results suggested that in general subjects agreed with the trainer's simulation (i.e., most aspects scored close to 3) (Fig. 4.12) and all subjects strongly agreed that the device was useful as an educational tool for healthcare trainees to learn spasticity and rigidity (scored 4.86 out of 5). A few responses that scored away from 3 were summarized and later used to explain discrepancies in Classification Test in Section 4.4B. For LR, subjects reported that the resistance magnitude should be lower for UPDRS 1 and higher for UPDRS 3. For CR, subjects indicated that the cogwheel frequency was "about right" across levels, whereas the cogwheel magnitude was

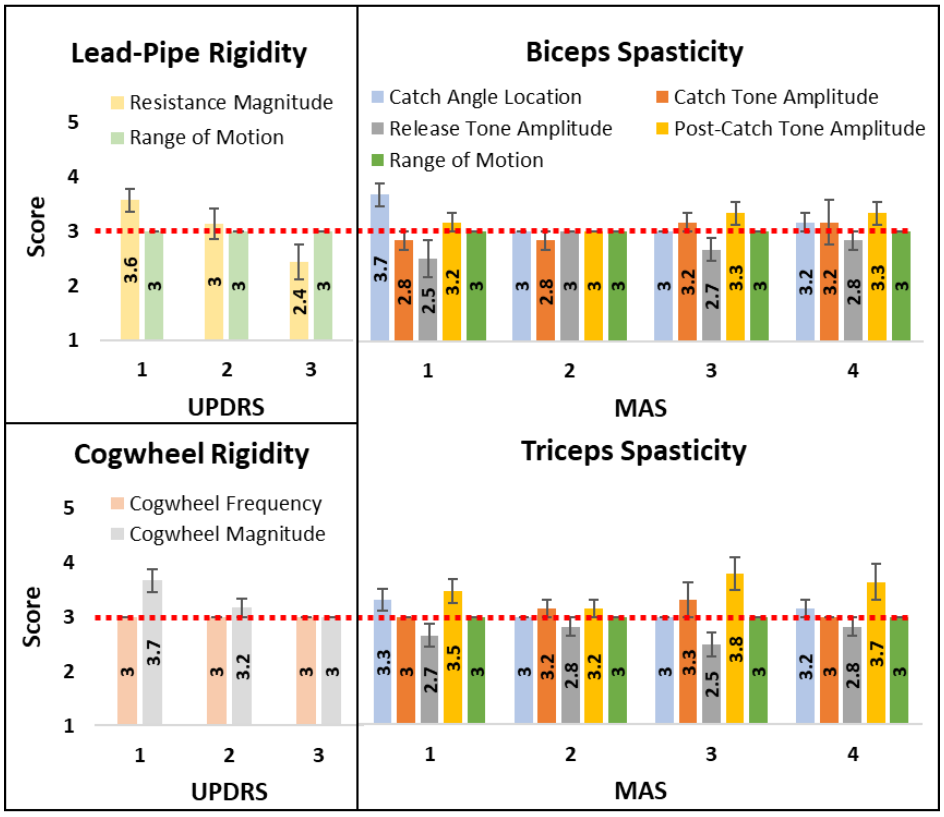

Fig. 4.12: DAT results on simulation aspects of LR, CR, and SP. A score of 3 was considered "about right" or "neutral". Mean scores were reported for each aspect. Error bar: standard error.

higher than expected for UPDRS 1 and 2. On the other hand, for SP, subjects reported that the catch should occur earlier in the ROM for MAS 1 and 4. They also indicated that the catch tone should be lower for MAS 3. Furthermore, there should be more release for MAS 1 and MAS 3 and the post-catch tone should be lower for MAS 1, 3, and 4.

4.4 Discussion

A. Modeling, Control, and Benchtop Validation

In summary, three abnormal muscle conditions at different severity levels and health normal condition (for a total of 15 conditions) were mathematically modeled, and their corresponding torque profiles were tracked by a proposed control system involving feedback, feedforward, and disturbance observer control on the SEA-based task trainer.

We started with the feedback controller inherited from the ankle-foot trainer (Chapter 2 and [58]), but since the mass and inertia of the trainer's forearm were lower than an actual human forearm, we incorporated a model-based feedforward controller to compensate for the mismatch. In the context of our SEA, the force sensor is the series spring located between the elbow and forearm, so the mass and inertia of forearm mechanism and protective shrouds were considered as post-sensor mass and inertia. It is known that it is difficult to modulate the apparent post-sensor mass and inertia with feedback force control algorithms and such systems usually need to rely on feedforward control [137]. In the case of the ankle-foot trainer, the post-sensor mass and inertia were similar to that of a biological foot, so the feedforward control was not involved. Other than rendering the trainer's forearm with a higher mass and inertia, the feedforward control also took over several tasks from the feedback control (such as compressing the spring and accelerating the motor), leaving the feedback control to only address the remaining torque error due to unmodeled dynamics.

This robotic task trainer is a typical application with force control accuracy requirement under external disturbance. The user's input motion (i.e., moving the forearm to assess the muscle tone) represents the motion disturbance that constantly perturbs the end of the series spring connected to the forearm and this motion disturbance should be rejected in the perspective of the force control. In addition, as the user holds onto the trainer's forearm, the mass and inertia of the user's own arm is coupled with the robotic trainer's dynamics, causing model variation that degrades the performance of model-based control schemes. Therefore, DOB was introduced in our control system, which is a simple and effective robust control scheme widely used in the industrial motion control [134]. We implemented the DOB with a nominal plant only considering the robotic trainer model (ignoring human interaction dynamics) to reduce the effect of internal and external disturbance from human interaction in the innermost current loop [123], in order to facilitate the design of cascaded feedback control (i.e., enable higher gains in the outer loop controllers).

Overall, the proposed control system ($C_{FB} + C_{FF} + C_{DOB}$ with high gain) was found effective in tracking all three behaviors (Table 4.2 and Fig. 4.9). Among the three behaviors, as expected, the LR profile was the simplest to track, resulting in the lowest RMSE (< 0.16 Nm even for just C_{FB} only). On the other hand, SP and CR profiles were more complex and challenging due to an abruptly changing piecewise torque trajectory and high frequency oscillations, respectively, so their tracking errors were higher. Note that for all behaviors, although the amplitude of RMSE increased with MAS and UPDRS scores because of higher torque command amplitudes associated with higher severities, the error percentage remained about the same across severities (small error percentages, i.e., < 2.5 % for LR, < 2.8 % for CR, and < 2.3 % for SP).

B. Clinical Expert Validation

Classification Test results suggested that subjects were able to distinguish three different behaviors with a good accuracy of 87 % (92 % without Subjects 4 and 7) (Fig. 4.9). Occasionally, subjects identified some SP trials as LR or CR. For MAS 1 (both biceps and triceps), the catch occurred later than expected in the ROM (Table 4.1) (scores of 3.7 and 3.3). Since the release behavior was barely felt as it was too late (scores of 2.5 and 2.7), subjects might consider LR occurring at the end of the ROM, thus rating the trial as mild LR (UPDRS 1 or 2). Similarly, for severe SP trials (i.e., MAS 3 and 4), the catch and post-catch resistance magnitudes were quite higher than expected (scores > 3). It was difficult to push the arm through the entire ROM and subjects might have felt a constant high resistance for a large portion of the ROM, therefore judging the trial as severe LR case (i.e., UPDRS 3). Additionally, Subjects 3 and 4 confused two of the SP trials with CR, where Subject 4 commented that the vibrations coming from the drivetrain could be the confusing factor (i.e., it felt similar to the tremor of CR), which might explain this misclassification.

Some discrepancies were observed between their judgement and the actual simulated severity and DAT results might provide some explanations (Fig. 4.10). For LR, the resistance magnitude was scored 3.5 for UPDRS 1 and 2.3 for UPDRS 3, which could explain why subjects misinterpreted UPDRS 1 as higher levels, or UPDRS 3 as lower levels. For CR, subjects mentioned that the cogwheel magnitude should be lower for UPDRS 1 (a score of 3.7) which suggests why this severity was confused with UPDRS 2. For SP, subjects suggested more release and lower post-catch tone amplitude should be implemented for MAS 1 which may explain why they misidentified MAS 1 as MAS 2 in some trials. They also indicated that the catch and post-catch tone amplitudes

were higher than their expectations for MAS 3 which may also explain why MAS 3 was confused with MAS 4.

Three subjects also commented that clinically they would usually pay more attention to rating the patient based on severity groups such as mild (MAS 1 and 2) or severe (MAS 3 and 4) to determine the treatment plan, rather than identifying the exact MAS level within a severity group. Furthermore, during a normal assessment, clinical signs from other parts of the body (e.g., posture, hand positioning) usually also provide insights regarding the patient's neurologic conditions, not solely the muscle tone. Therefore, our Classification Test was more difficult than during the clinician's regular practice, in the sense that it required subjects to rate the exact severity level only based on muscle tone information. Even in this strict and challenging assessment scenario, it is quite promising to see that subjects were able to distinguish across behaviors and identify the severity group for each behavior. This observation suggests that the simulation provided by our task trainer captured the key characteristics of each behavior and the design of each severity level mostly aligned with the subjects' previous experience. Furthermore, if the examiner used improper technique or did not closely feel the muscle tone with multiple trials, it was observed that assessing muscle tone was challenging even for experienced clinical experts (e.g., Subjects 4 and 7). This observation further motivated the significance of the robotic task trainers in improving the proficiency and standardization of the assessment technique for the trainee. Overall, subjects agreed that the device could be a useful medical education training tool for healthcare learners to practice both rigidity and spasticity assessment techniques and highly recommended this training approach to their students.

C. Limitations and Future Work

In retrospect, some control complexity could have been avoided if the control requirements

were comprehensively accounted in the mechanical design. For example, the task trainer was originally designed to only mimic LR (i.e., a slow-varying torque profile), and the system natural frequency (determined by the spring stiffness, gear ratio, etc.) was around 3 Hz, which posed difficulties to perform fast simulation tasks such as CR and SP. These faster tasks motivated us to use DOB with a faster nominal plant to suppress the open-loop system resonance.

In this human-robot interaction scenario, the trainee's dynamics (or more generally, environment dynamics) are coupled to the task trainer's dynamics. It is known that force control performance varies with different environment dynamics [88]. Therefore, in this work, the environment dynamics was considered as a source of disturbance, and we attempted to reject it by a fixed-gain feedback controller and a DOB scheme. In the context of medical training, trainees with different body sizes (i.e., load mass), joint stiffness (i.e., load impedance) and techniques (i.e., load motion disturbance) represented different possible environment dynamics to interact with the task trainer. Therefore, a variable-gain controller might be more suitable for this application and potential controllers could be explored, e.g., adaptive control, gain-scheduling control, or optimization-based control (e.g., model predictive control).

Furthermore, valuable feedback was received from the clinical validation study regarding the fine-tuning of the simulation aspects. As future steps, the device should be experimentally deployed and incorporated into the curriculum for healthcare students.

4.5 Conclusion

This chapter presented the modeling, control, and clinical validation pipeline of a robotic arm task trainer to mimic three abnormal muscle behaviors namely lead-pipe rigidity, cogwheel rigidity, and spasticity at varied severities. The SEA-based system together with the presented control system was validated to be able to deliver accurate torque control during user interaction.

Based on the clinical study results, this task trainer can be a clinically useful and cost-effective medical education tool to provide realistic and consistent practice opportunities for clinical learners to get proficient with rigidity and spasticity assessment techniques to reduce the need for human patients.

CHAPTER 5

PRELIMINARY RESULTS OF CLINICAL QUANTIFICATION OF SPASTICITY AND RIGIDITY IN THE UPPER EXTREMITY [11]

Abstract

To systematically design task trainers to mimic abnormal muscle behaviors and severity levels, quantitative data describing kinematic and kinetic relationships of these behaviors are necessary. Currently, there is a lack of quantitative data in the literature to describe these relationships when using a passive stretch test to assess spasticity or rigidity (lead-pipe and cogwheel types). To assist with development of an upper-extremity task trainer for practicing the neurologic exam and to establish a large database on the upper arm muscle groups (biceps/triceps), we are conducting a cross-sectional study across individuals with spasticity or rigidity. This clinical data collection study is being conducted in China with a goal of documenting kinematic and kinetic data for different severity levels of spasticity and rigidity (lead-pipe and cogwheel types) and healthy control subjects. The target is to assess at least 10 individuals per behavior and severity level, for a total of 110 subjects. Given the COVID-19 pandemic in China, the study has been delayed and only a pilot group of 15 spasticity subjects have been tested. Data from 10 are

[11] A brief report of preliminary results from spasticity patients was presented in [73]: Pei, Y., Feng, Y., Song S.Y., Zallek, C.M., Liu, T., and Hsiao-Wecksler, E.T., 2022. Quantification of Elbow Spasticity (Preliminary Results), North American Congress on Biomechanics, Ottawa, Canada, August 21-25, 2022.

included in the analysis of this chapter. Among these subjects, elbow kinematics, clinician's applied force and torque, and surface electromyography data were collected. An inverse dynamics procedure was performed to compute the elbow net joint torque. Clinical observations obtained through the progress of this study have been used to guide the choice of spasticity model parameters in Chapter 4 Section 4.2B. Through the pilot study, a few limitations of the current sensor setup have been identified, and potential solutions are proposed.

5.1 Introduction

Accurate clinical assessments of spasticity and rigidity are needed for effective patient diagnosis and management. These abnormal muscle behaviors arise from upper motor neuron or basal ganglia lesions observed with some neurologic conditions. Assessment involves a clinician passively stretching the patient's muscles and assessing the resistance to movement. Clinical scales, e.g., the Modified Ashworth Scale (MAS) for spasticity [138] (Table 5.1) and the motor portion of the Unified Parkinson's Disease Rating Scale (UPDRS) for rigidity [139] (Table 5.2), are used to rate a patient's severity level based on behaviors observed or felt by the clinician. The qualitative nature of these scales can result in poor consistency and low reliability.

The establishment of a quantitative database containing kinematic, kinetic, and muscle activation patterns of abnormal muscle tone during clinical assessments can be useful for a board spectrum of audience. Quantitative measurements could improve assessment and clinicians can objectively track the severity of their patient's impairment with an instrumented device. Furthermore, the database will provide quantitative evidence for neuropathologists and neuroscientists to understand the underlying neuromuscular mechanics of abnormal muscle tones. For engineers like us who want to develop medical education task trainers for neurologic

examination training, the kinematic and kinetic relationship of the pathologic muscles will guide the design of the simulated behaviors.

The overarching goal is to recruit and test at least 110 participants of various muscle condition and severity for data collection purpose. Therefore, this study serves as a pilot study to this long-term goal and we aim to develop a robust and efficient clinical pipeline. This study presented the implementation of a feasible instrumented wearable sensor setup, the test protocol design, and potential data analysis approaches. A pilot group of 15 subjects (spasticity only) were recruited and tested with the proposed workflow.

Table 5.1: Modified Ashworth Scale (MAS) for assessing spasticity [138].

Score	Description
0 (0)[a]	No increase in muscle tone
1 (1)	Slight increase in muscle tone, manifested by a catch and release or by minimal resistance at the end of the range of motion when the affected part(s) is moved in flexion or extension
1+ (2)	Slight increase in muscle tone, manifested by a catch, followed by minimal resistance throughout the reminder (less than half) of the range of motion
2 (3)	More marked increase in muscle tone through most of the range of motion, but affected part is easily moved
3 (4)	Considerable increase in muscle tone, passive movement difficult
4 (5)	Affected part is rigid in flexion or extension

[a] Numbers in parenthesis represent a variant of the Modified Ashworth Scale [15] and this convention was used throughout this dissertation.

Table 5.2: Motor section of the Unified Parkinson's Disease Rating Scale (UPDRS) for assessing rigidity [139].

Score	Description
0	No rigidity
1	Slight or detectable rigidity only detected with activation maneuver
2	Mild to moderate rigidity detected without the activation maneuver, but full ROM is easily achieved.
3	Marked rigidity detected without the activation maneuver; full ROM is achieved with effort.
4	Severe rigidity detected without the activation maneuver and full range of motion not achieved.

5.2 Scope of Quantitative Database

We seek to conduct a cross-sectional study targeting at least 110 test participants (Table 5.3) to build a quantitative database on measured elbow kinematic and kinetic behaviors in patients with spasticity, lead-pipe rigidity, and cogwheel rigidity across severities and healthy controls during passive stretch tests. These four types of subject groups (18-80 yrs) will be recruited by clinicians at Zhejiang Hospital and Pudixin Rehabilitation Hospital in Hangzhou, China. IRB approval has been received from the University of Illinois at Urbana-Champaign and Zhejiang Hospital System.

Table 5.3: Recruitment target for the quantitative database.

Subject Condition	Severity	Sample Size	Total Recruitment Number
Spasticity	MAS levels 1, 2, 3, 4	10	40
Lead-pipe Rigidity	UPDRS levels 1, 2, 3		30
Cogwheel Rigidity			30
Healthy	/		10

The desire is to collect data from at least 10 individuals per behavior and severity level, which would result in needing only 110 test participants. The same severity level of rigidity (lead-pipe or cogwheel) is typically observed for both agonist and antagonist muscle groups; however, in

spasticity, agonist and antagonist muscle groups may present as different severity levels. Therefore if a spasticity patient presents with different severity levels in the agonist and antagonist muscle groups (biceps/triceps), then additional patients will be recruited to achieve 10 samples per condition and severity level.

5.3 Instrumented Clinical Assessment Tools

A multi-sensor wearable instrumented setup was established (Fig 5.1, left). A custom device created by our group, the Position, Velocity, and Resistance Meter (PVRM) [72], consisted of two modules: moving (wrist) and main (upper arm). Each module contained a 6-axis IMU[12] (MPU 6050, InvenSense, USA). The moving module also included a 6-axis force/torque (F/T) sensor (M3703C, Sunrise Instruments, China). The compact design of the moving module allows clinicians to use their regular manual assessment technique (Fig 5.1, right). The PVRM records elbow joint angular position and velocity via the IMUs and the clinician's applied load via the F/T sensor. This IMU was selected because the absolute heading measurement was not required and also there would be no magnetic interference issue due to surrounding ferrous objects in the indoor

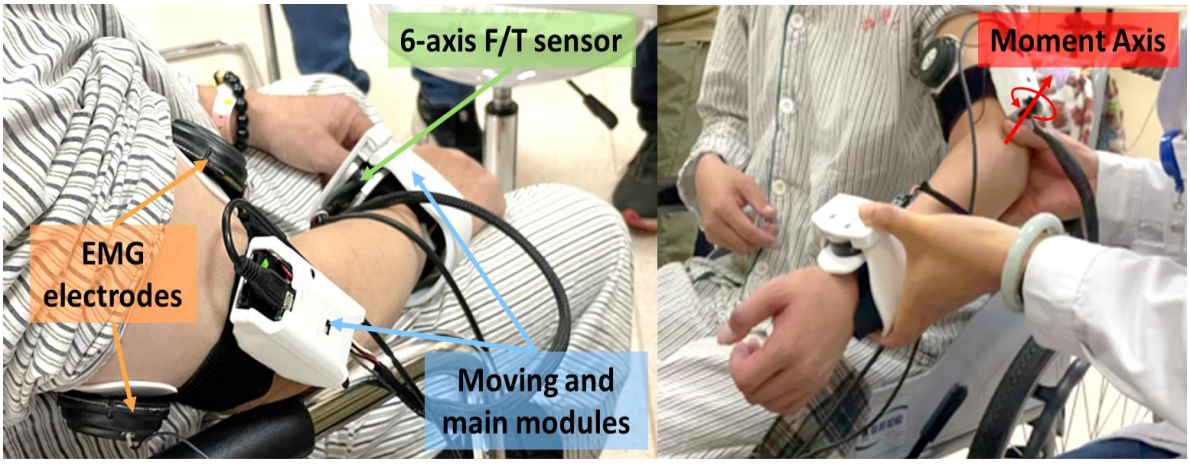

Fig 5.1: (Left) Sensor placements of the PVRM. (Right) Clinician's assessment technique with the instrumented setup.

[12] A 6-axis IMUs only contains a 3-axis accelerometer and a 3-axis gyroscope, without a magnetometer. A 9-axis IMU will also have a 3-axis magnetometer to measure the magnetic field strength.

environment. As opposed to using a uniaxial load cell, the 6-axis F/T sensor decouples measurements of all forces and torques applied by the clinician at the subject's wrist. This way, only the force and torque components that generate torque around the elbow joint are considered in the calculation. Additionally, surface electromyography (sEMG) of the biceps and triceps were monitored by a wireless sEMG system (Kine, Kiso Inc., Iceland) to ensure that the subject was fully relaxed before the passive stretch, so that the effect of voluntary muscle contraction could be minimized.

5.4 Test Protocol

Before the passive stretch test, three maximum voluntary isometric contraction (MVIC) trials are performed for both the biceps and triceps, and sEMG data corresponding to MVIC trials are recorded (V_{MVC_bi} and V_{MVC_tri}).

All subjects (regardless of conditions) will go through the same set of passive stretch tests with two different speeds. Each subject's elbow is first passively moved in slow speed (i.e., peak speed < 30 °/s) for five extension-flexion cycles. Next, the elbow is moved using the clinician's preferred fast speed for three trials per muscle group (i.e., biceps and triceps). Throughout this process, the tested arm should remain in the vertical plane (i.e., no shoulder abduction). The slow trials aim to document the baseline biomechanical muscle tone with minimal reflex activity, so that the neural component of muscle tone is expected to be small. The fast trials are used to elicit hyperactive stretch reflex to record the spastic muscle tone, providing a combination of biomechanical and neural components of muscle tone. After each fast stretch, the forearm is reset for next the fast stretch trial by slowly moving the forearm to the most flexed or extended position based on whether the biceps or triceps is being assessed. Kinematic data are sampled at 100 Hz. Applied forces and torques are sampled at 400 Hz. sEMG signals are collected from biceps and

triceps muscles at 1600 Hz. The protocol and PVRM system were designed to align with the regular clinical assessment procedure and technique used, so that the quantified responses documented in this study also reflect the type of exam observations that clinicians normally encounter in their daily routines.

5.5 Data Analysis

Readings from IMUs and the F/T sensor are used to compute the elbow kinematics and calculate the net muscle torque at the elbow. Forearm and upper arm segment angles (ϕ_f, ϕ_u, respectively) are determined by the IMU orientations. The elbow joint angle (θ_E) will be calculated by the subtraction of segment inclination angles, i.e., $\theta_E = \phi_f - \phi_u$ (Fig. 5.2). Elbow angular velocity ($\dot{\theta}_E$) is obtained by the subtraction of gyroscopic readings from the two IMUs, i.e., $\dot{\theta}_E = \omega_f - \omega_u$. Torque about y-axis ($\tau_y$) and force along z-axis (F_z) are used to calculate the clinician's applied torque ($\tau_{clinician}$) with L_f recorded with a measuring tape before the passive stretch test (5.1).

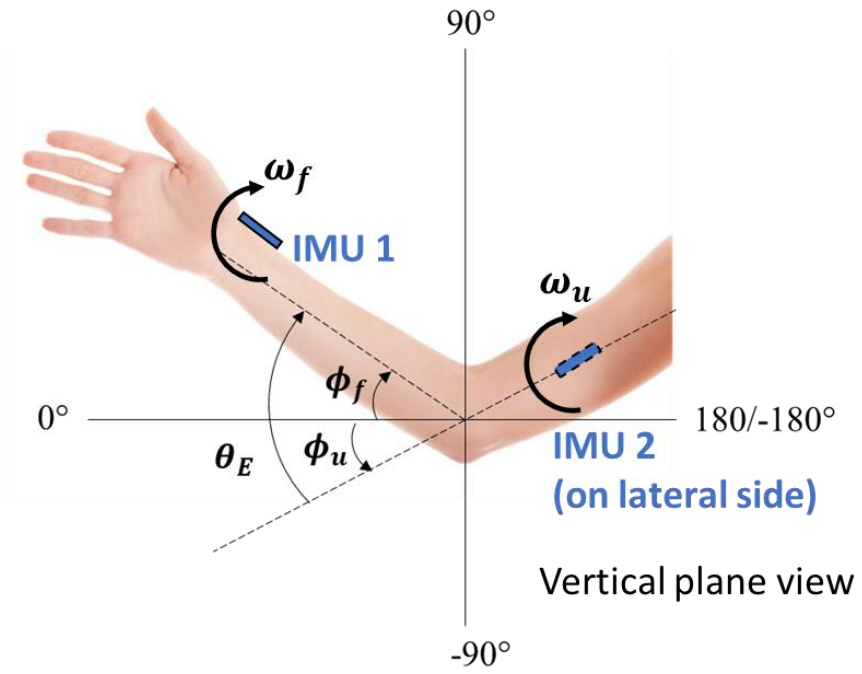

Fig 5.2: Definition of elbow joint kinematics and associated IMU readings. ϕ_f, ω_f: forearm inclination angle and angular velocity. ϕ_u, ω_u: upper arm inclination angle and angular velocity.

The moment equilibrium equation is derived with respect to elbow joint based on Fig 5.3 (5.2). Muscle resistive torque (τ_{muscle}) is calculated by removing inertial and gravitational torques from $\tau_{clinician}$ using inverse dynamics (5.3). In this equation, the forearm moment of inertia at elbow joint ($I_{f,E}$), the forearm mass (m), and forearm COM location (L_{f_COM}) are estimated using anthropometric table formulae [107] and forearm segment angle and angular acceleration ($\phi_f, \ddot{\phi}_f$) are measured by the wrist IMU. $\ddot{\phi}_f$ is obtained by numerical differentiation of the filtered forearm IMU gyroscope data (ω_f). All data will be filtered by a 4th order Butterworth filter with cut-off frequency of 4 Hz for angular position, velocity, and acceleration signals, and 15 Hz for force and torque signals.

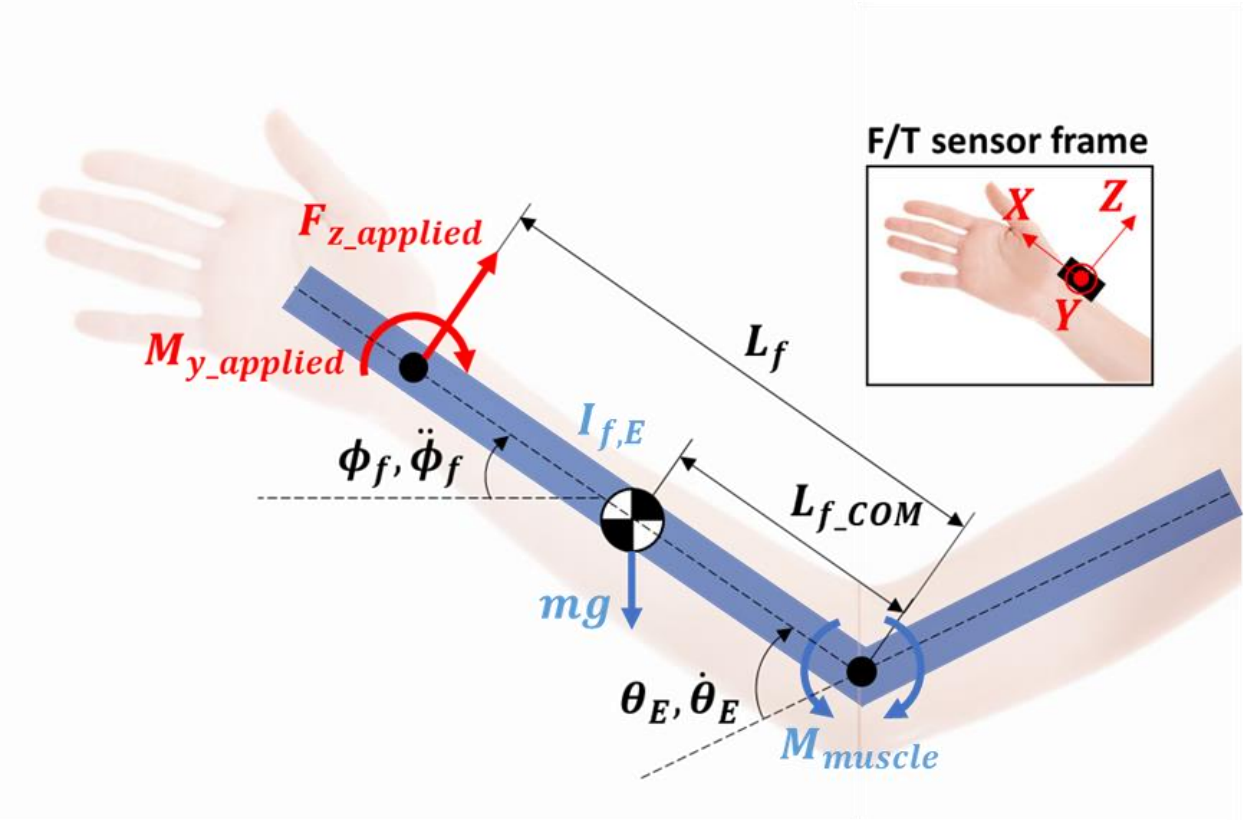

Fig 4.3: Free body diagram of forearm and elbow for inverse dynamics calculation.

$$+\circlearrowleft \sum \tau_{applied@elbow} = \tau_{clinician} = \tau_{y\_applied} + F_{z\_applied} L_f \quad (5.1)$$

$$+\circlearrowleft \sum \tau_{forearm@elbow} = I_{f,E}\ddot{\phi}_f = \tau_{clinician} - mgL_{f_{COM}} cos\phi_f - \tau_{muscle} \quad (5.2)$$

$$\tau_{muscle} = \tau_{clinician} - I_{f,E}\ddot{\phi}_f - mgL_{f\_COM} cos\phi_f \quad (5.3)$$

sEMG signals will be detrended, notch filtered (at 50 Hz), bandpass filtered (4th order Butterworth filter at 10-500 Hz), and rectified. If the resulting signals exceed 70% of MVIC voltage (i.e., $0.7V_{MVC\_bi}$ or $0.7V_{MVC\_tri}$) for 0.5 s, that trial will be considered as containing voluntary muscle contraction and therefore will be rejected.

5.6 Preliminary Results and Discussion

In this preliminary stage, 15 spasticity subjects have been assessed by three experienced clinicians (Table 5.3). Five subjects were excluded from the data analysis due to hardware technical problems and incorrect shoulder abduction placement (discussed in Section 5.7). This initial pilot study validated the sensor setup and test protocol. The recorded time history of muscle tone pattern remained consistent across trials (Fig. 5.4). No sign of loosening-up of muscle tone was observed after the specified number of passive stretch trials in the protocol (e.g., muscle tone did not reduce after repetitive stretches).

Table 5.3: Subject demographic summary. MAS scores were assessed before testing.

Subject ID*	Age	Gender	Affected side	Biceps MAS	Triceps MAS	Cause**	Post Injury	Clinician
1	49	M	R	0	1	HS	2 months	1
2	36	M	L	2	2	HS	3 months	1
3	79	F	L	1	1	IS	3 months	1
4	61	M	L	2	2	HS	6 yrs	1
5	60	M	R	2	2	IS	2 yrs	1
6	68	M	L	2	0	IS	1 month	2
7	57	F	L	2	3	IS	7 yrs	2
8	72	F	L	1	3	IS	9 yrs	2
12	61	M	R	1	1	HS	1 month	3
15	38	M	R	1	2	IS	9 months	3

**HS: hemorrhagic stroke, IS: ischemic stroke

Two sample datasets from Subjects 5 (moderate spasticity) and 1 (very mild spasticity) are presented for demonstration (Fig. 5.4-5.6). Increased muscle tone was observed in the fast trials compared to slow trials (Fig. 5.4), demonstrating the speed-dependency of spasticity. The catch-release behavior was elicited for Subject 5 with moderate spasticity (Fig. 4.4BC, yellow shaded areas), where there was an abrupt rise of the muscle tone followed by a decrease of the muscle tone. Furthermore, by examining the relationship between moment profiles and joint angle, regardless of patient severity, moments were similar in biceps and triceps during slow trials (i.e., tight hysteresis loop) (Fig 5.5A and 5.6A). Subject 5 with moderate spasticity had significantly elevated muscle tone during fast stretch of the affected muscle group (Fig. 5.5BC), compared to the muscle tone during the slow reset motion, which was similar to those observed during slow trials (Fig. 5.5A). For Subject 1 with very mild spasticity, during fast trials, although stretch speeds were different between extension and flexion, there was little muscle tone difference between two motion directions (Fig 5.6BC). In addition, the trend of τ_{muscle} was more consistent across severity

levels (roughly positive slopes of moment vs. angle) (Fig 5.5 and 5.6), whereas $\tau_{clinician}$ (muscle tone sensed by the clinician) had the opposite trend (negative slopes) in Subject 1 with mild spasticity (Fig 5.6). This observation suggested that the inertia and gravitational effect of the patient's forearm might distort the clinician's feeling of elbow muscle resistance when spastic muscle tone is less dominating; thus, highlighting the difficulty of clinically diagnosing mild spasticity at an early stage [140]. Based on these basic plots (Fig. 5.4-5.6), more advanced parameters, such as catch amplitude, release amplitude, catch angle location, were derived to model the spasticity behaviors at different severity levels (presented in Chapter 4 Section 4.2B).

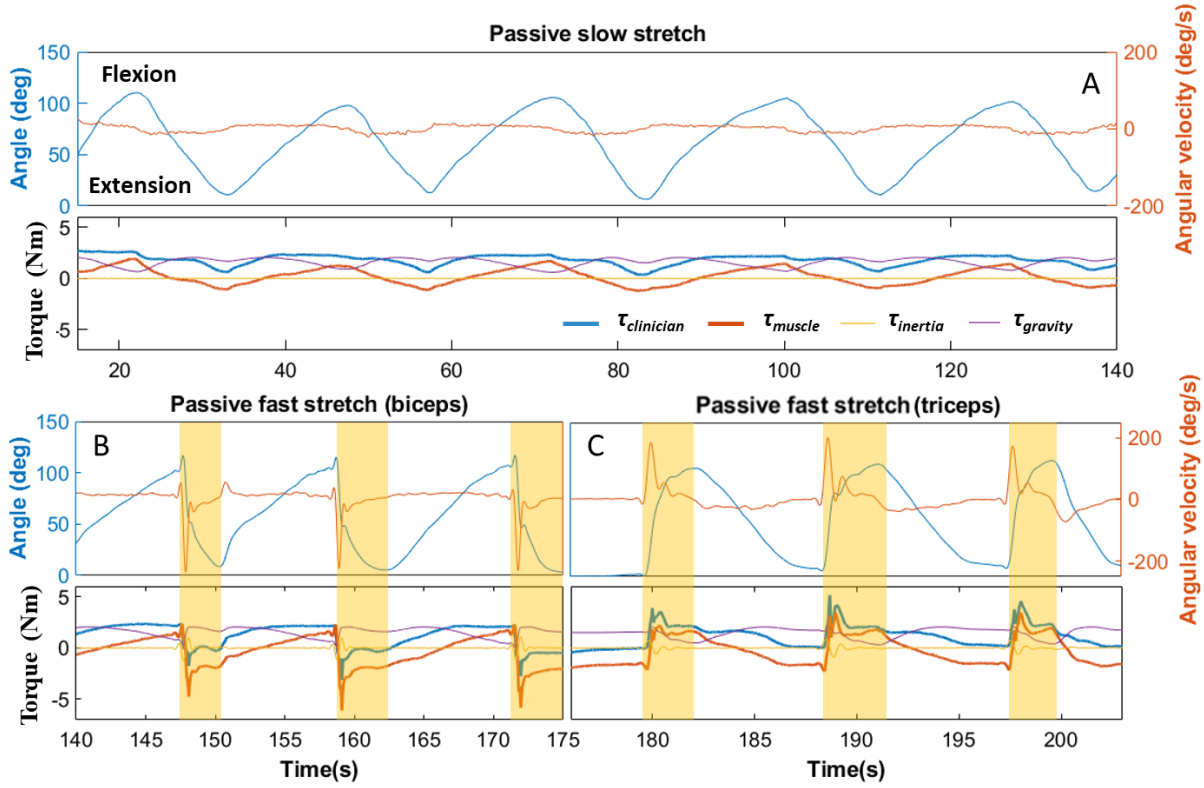

Fig. 5.4: A sample dataset from Subject 5 (biceps MAS 2 and triceps MAS 2). Time-series of kinematics and moment profiles during (A) slow extension-flexion cycles, fast stretch of (B) biceps and (C) triceps. Yellow shaded areas indicated the time window for fast passive stretch.

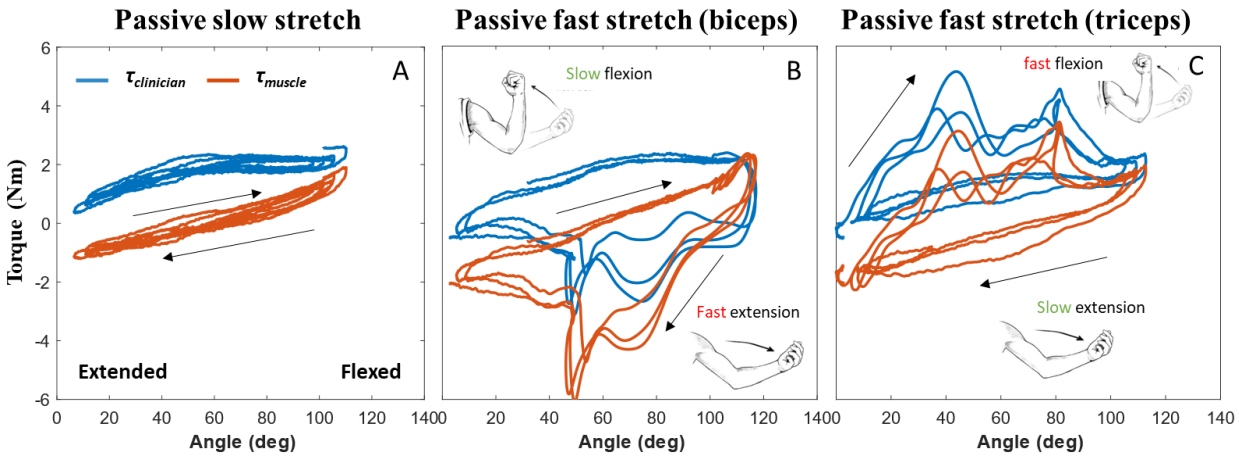

Fig. 5.5 A sample dataset from Subject 5 (biceps MAS 2 and triceps MAS 2). Moment profiles versus elbow joint angle during (A) slow extension-flexion cycles, (B) fast stretch of biceps, and (C) fast stretch of triceps.

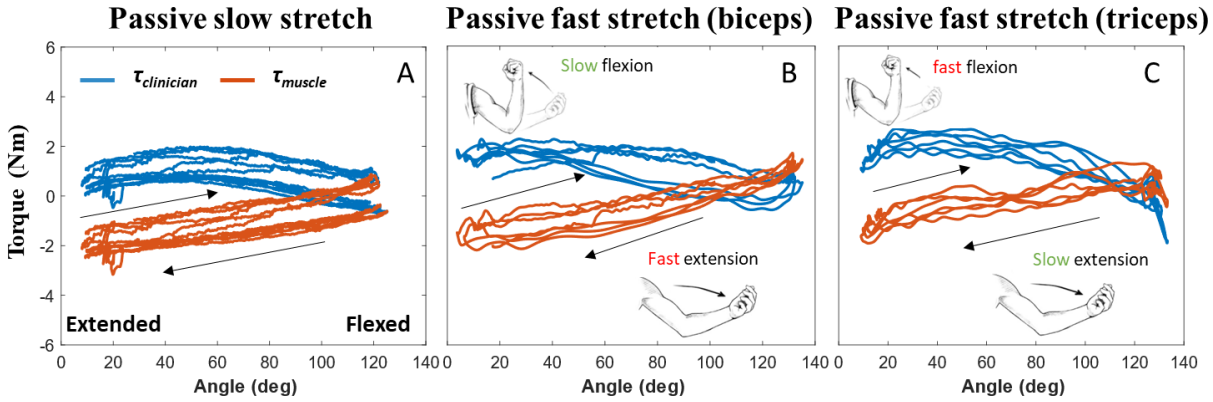

Fig. 5.6 A sample dataset from Subject 1 (biceps MAS 0 and triceps MAS 1). Moment profiles versus elbow joint angle during slow extension-flexion cycles, fast stretch of biceps, and fast stretch of triceps.

5.7 Potential Problems and Possible Solutions

At this stage, the pilot dataset was weighted on mild spasticity cases and there is a lack of data for severe spasticity conditions. Due to the COVID Omicron wave in major cities in China, hospital access is strictly restricted, and our data collection has slowed down. This situation delays the study progress and makes it more difficult for patient recruitment. Due to this delay, two participating Zhejiang University undergraduate researchers who are previously responsible for

on-site data collection graduated in the summer of 2022. The responsibility for data collection has been transferred to other grad students in Prof. Liu's lab. New recruited researchers will need training and will have a learning curve. Finally, severe spasticity patients (MAS 3 and 4) are rare in general and rigidity patients (usually due to Parkinson's diseases) are usually absent from rehabilitation centers, so it will be difficult and time-consuming to recruit these subjects. Given the available dataset of ten spasticity subjects and convenience of recruitment, future analysis and recruitment could prioritize the spasticity group. For this incremental milestone, the ideal sample size will be around 28-40 per muscle group (7~10 samples per MAS level, for MAS 1, 2, 3, 4). In the future, additional study centers might be explored for the recruitment of rigidity patients.

Through the pilot study, a few clinical observations suggested a more robust joint angle calculation scheme would be necessary. Due to the increased involuntary muscle tone associated with the abnormal muscle behaviors, some patients developed muscle atrophy in their upper-extremities given a prolonged period of lack of exercise [141,142]. As an added consequence of muscle atrophy, there was excessive skin movement affecting the attachment of the sensor module. Furthermore, due to the pathological body posture, a few patients could not reach the desired testing posture (i.e., keeping the limb motion in the vertical plane) because of the lack of flexibility in their shoulder joints. Therefore, these subjects had to be tested with nonzero shoulder abduction angles. Two potential problems related to IMU measurement were identified : a) sensor misalignment (especially the upper arm module) and b) joint angle calculation in the presence of nonzero shoulder abduction angle (Fig. 5.7). These problems will degrade the fidelity of the joint angle calculation based on segment inclination angles, because the assumption that limb motion stays in the vertical plane is violated. In order to account for these clinical cases, more robust joint angle calculation methods such as the one proposed by Seel et al. [143] should be explored. The

algorithm proposed by Seel and colleagues was tailored for biomechanics application of using 6-axis IMU (only gyroscope and accelerometer, no magnetometer) to measure human joint angles. It first involves a self-alignment procedure of the joint axis with respect to local sensor frames to compensate any misalignment issue and then calculates the joint angle using any sensor fusion method (in their case, a complementary filter) in the aligned frame. This alignment procedure would account for sensor misalignment relative to the elbow joint. Also, since the IMU readings would be mapped into the local aligned frame regardless of the orientation of the limb in the global frame, a nonzero shoulder abduction angle would be allowed during data collection.

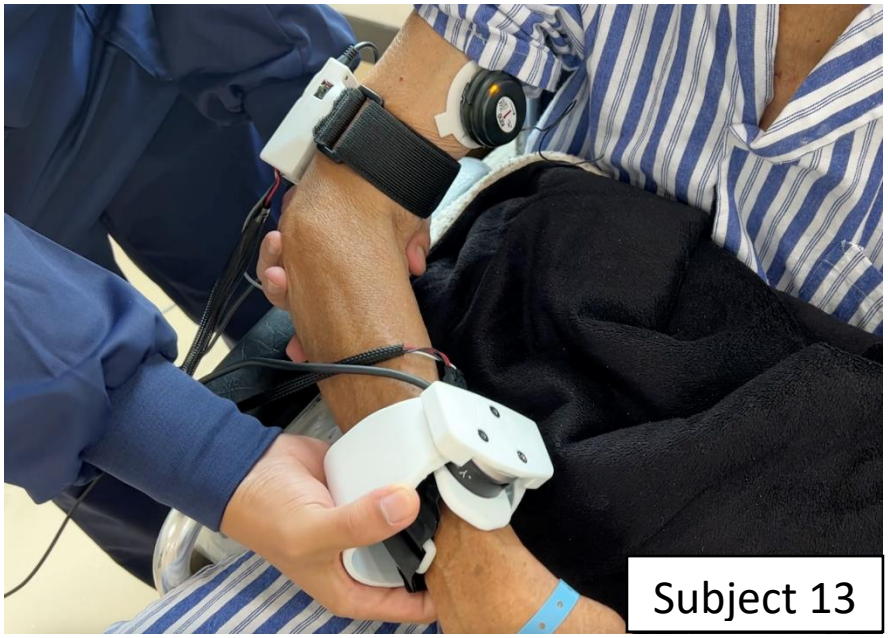

Fig. 5.7: An example photo from Subject 13 where there existed some misalignment for the upper arm IMU module as well as non-negligible shoulder abduction angle.

5.8 Future Work

A pilot dataset was collected from the first cohort of spasticity subjects. Some preliminary data analysis approaches were explored and at the same time, in order to facilitate future larger-scale data collection, a potential improvement to the IMU-based joint angle calculation was

identified and proposed to improve the robustness and efficiency of the clinical study.

Currently, as we are waiting for the data collection to resume, we are working on validating the algorithm from Seel et al. in our PVRM hardware. Compared to the high-end Xsens IMUs (> $ 500) used in their studies [143,144], we hope to implement this approach on our low-cost InvenSense MPU 6050 IMUs (~$ 5 each). Two test scenarios have been set up for a benchtop validation.

First, a motorized testbed setup proposed in [145] was adopted and modified (Fig. 5.8). This testbed consists of a stepper motor (with an optical encoder on the shaft), a lever arm, and two IMUs. The stationary IMU is mounted on the motor bracket and the moving IMU is attached to the end of the lever arm. The lever arm between two IMUs represents the human forearm and the angle of blue motor mount could be adjusted to represent different shoulder abduction angles. The joint angle calculation based on IMU readings will be validated again the ground-truth motor shaft encoder. IMU 2 and the moment arm will be driven by the stepper motor at slow (< 30 °/s), medium (100 °/s), and fast speed (200 °/s) at various motor mount angles to mimic shoulder abduction angles at 0 (no abduction), 30, 60°.

Second, the benchtop validation will be carried out in a less structured environment, i.e., the 3D-printed housings representing the main and moving modules of the PVRM will be mounted on a human subject in a motion capture space. The IMU-based joint angle estimation will be compared with another ground-truth motion capture system (Fig. 4.9). Eight motion markers will be placed on the shoulder, elbow, wrists, and 3D-printed housings. The motion capture system will provide an estimate of elbow joint angle, which is used to validate the IMU results. Approximately six healthy subjects (three males and three females) will be recruited to participate in the study. This PVRM-like IMU setup will be attached to the dominant arm of the subject and then the subject

will be asked to voluntarily move the forearm through the ROM at slow (< 30 °/s), medium (100 °/s), and fast speed (200 °/s) at shoulder abduction angles at 0 (no abduction), 30, 60°, similar to the first test. Once the IMU algorithm is validated via these benchtop tests, we will use it to process previously collected data where we noticed any IMU misalignment or significant shoulder abduction.

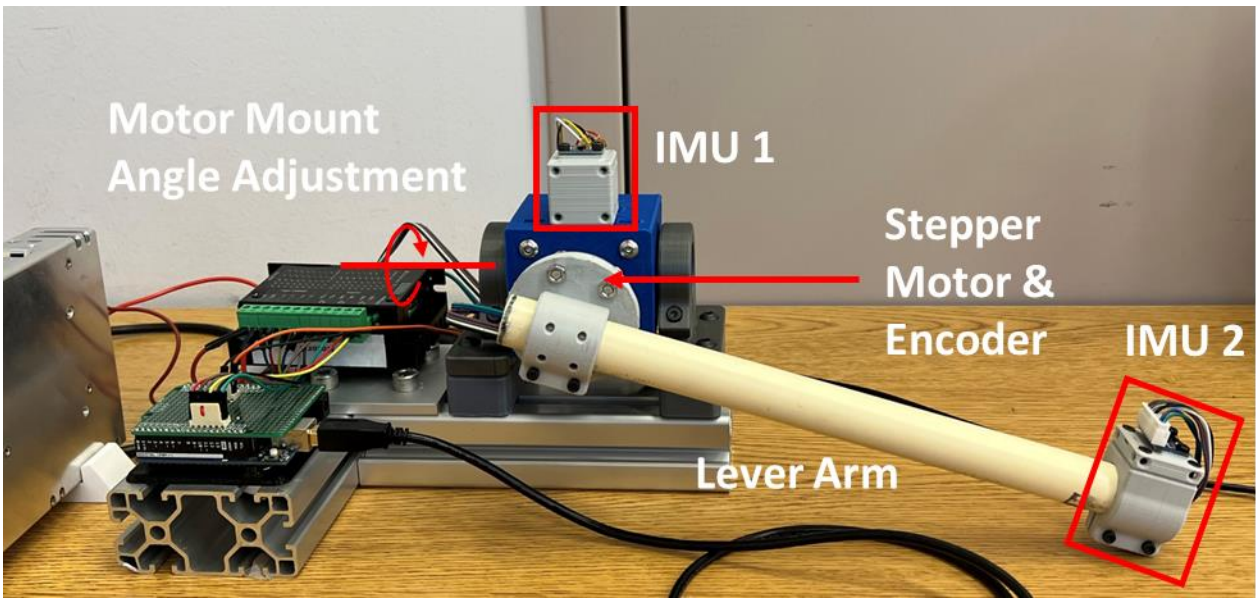

Fig. 4.8: A stepper-motor testbed to validate the joint angle calculation based on IMU measurement against motor shaft encoder reading. The angle of the motor mount can be adjusted to represent different shoulder abduction angle.

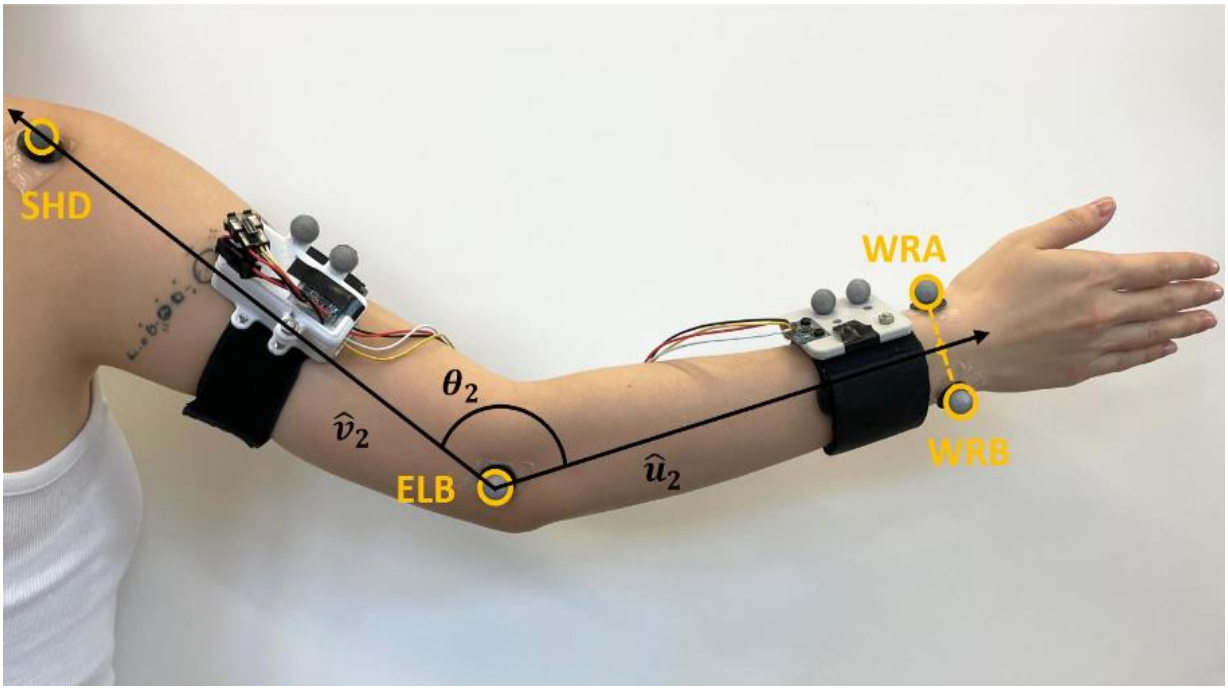

Fig. 4.9: The motion capture marker setup for the benchtop validation. Motion capture markers will be attached on 3D printed housings representing the main and moving modules of the PVRM as well as the human subject.

5.9 Conclusion

In this chapter, we presented an ongoing clinical data collection study conducted in China with a goal of documenting kinematic and kinetic data for different severity levels of spasticity and rigidity (lead-pipe and cogwheel types) and healthy control subjects. The pilot study recruited and tested 15 spasticity subjects. Among these subjects, elbow kinematics, clinician's applied force and torque, and sEMG data were collected and an inverse dynamics procedure was performed to compute the elbow net joint torque in the post-processing. A few limitations of the current sensor setup have been identified and potential solutions are proposed. Future steps involves validating the robust IMU algorithm in the lab environment and then deploying to the clinical setting to facilitate the large-scale data collection in the next phase.

CHAPTER 6

CONCLUSIONS

In contrast to the wide deployment of medical training simulators for surgical or anatomical tasks, currently there are no commercially available robotic training simulators for neurologic exams. Although there exist commercial solutions for kinematic-based training simulators and standalone haptic devices, a custom solution integrating force control capability into a robotic human-size mannequin for practicing neurological exams technique is still far from maturity. Therefore, so far this type of device remains in the proof-of-concept stage and the ideal actuation, sensing, and control solutions are yet to be identified in the academia. A few research prototypes have been proposed in the past [48–56], but none was deployed beyond their developers' own institutions possibly due to cost, maintenance, portability, or mechanical complexity issues. To deliver cost-effective and safe task trainers with high-fidelity force control capability, we selected the SEA design strategy and developed two electromechanical training simulators for mimicking common abnormal muscle behaviors in both lower (Chapters 2 and 3) and upper extremities ([57] and Chapter 4). Through benchtop performance and clinical feedback, these devices have the potential to be transformed into feasible commercial training solutions for clinical learners in the fields of neurology, physical therapy, occupational therapy, etc.

6.1 Contributions and Connections

In this dissertation, design-validation frameworks for these robotic medical training simulators were presented. Chapter 1 reviewed previous designs of either active or passive training simulators, summarized the common actuation, sensing, modeling, and control approaches, and discussed their pros and cons. The advantages and disadvantages of the SEA strategy were

reviewed, and we reasoned why SEA could be a promising choice to achieve a balance across cost, performance, and safety, which have not been possible in the past designs.

In Chapter 2, we described our efforts on creating a novel SEA-based ankle-foot training simulator for replicating ankle clonus. To explore the design guideline and performance envelope of the SEA strategy for the ankle clonus simulation (potentially also for other common behaviors yet to be implemented), in this study, we emphasized the mechatronic design and system modeling of the actuation system. The device was validated in both benchtop tests and clinical evaluation. The experimental results and clinical feedback were promising and suggested that this device could mimic a real patient by a) generating a simulated clonus behavior whose triggering and maintaining mechanism aligned with clinicians' experience, and b) recreating a relatively realistic haptic response of affected muscles. The use of a SEA system resulted in not only a high-performance research simulator, but also a cost-effective and compact design that could become viable to be widely deployed as a valuable training tool for learners. In this study, the control problem associated with mimicking ankle clonus was essentially an indirect force control problem (i.e., via impedance control), since the replication of oscillatory clonus motion was of more importance compared to the accuracy of the haptic feedback force. Therefore, we only implemented a basic cascaded feedback control scheme in the low-level torque control to track an oscillatory ankle motion reference via the high-level impedance control. No gravity or inertial effect of the foot were rendered.

Inheriting the ankle-foot simulator platform developed in Chapter 2, we made minor hardware changes (i.e., adding an artificial tendon structure and a load cell) and then focused on the systematic model-based simulation of an abnormal muscle behavior (i.e., ankle tendon reflex) in Chapter 3. We presented our design methodology to enable trainees to practice tendon tap

technique on a robotic training simulator. The entire flow of tendon tap assessment (i.e., input tap force, reflex response model, and the ankle haptic response) was quantified for modeling and control purposes. Benchtop and clinical validation results were promising for deploying the SEA-based simulator to mimic ankle tendon reflex assessment training. This study also represented a case study that demonstrated how the existing hardware of the ankle-foot simulator could be easily expanded and reprogramed to mimic a different abnormal muscle behavior. Compared to ankle clonus simulation, the control task for replicating ankle tendon reflex became a direct force control problem. Even though the same low-level torque control was used as in Chapter 2, more considerations were put into the design of the high-level control command, which accounted for the gravitational and inertial of the foot, the stiffness and damping of the ankle joint, as well as the reflexive torque triggered by the tendon tap. Note that although the torque tracking accuracy in this study was satisfactory (with some undesired delay in Fig. 3.9), this performance was only achieved when there was minimal external motion disturbance (i.e., the trainee supports the foot statically and tap on a sensor on the ankle tendon structure). As we moved to replicate abnormal muscle behaviors in the upper extremity, we would face a direct force control problem with strong motion disturbance from the trainee, i.e., rendering forearm dynamics and muscle resistance during rapid passive stretch tests. Therefore, we started to realize that a low-level torque controller with only feedback scheme might not be sufficient and thus explored other control architectures in Chapter 4.

In Chapter 4, we presented the modeling, control, and clinical validation pipeline of a robotic arm training simulator to mimic three abnormal muscle behaviors namely lead-pipe rigidity, cogwheel rigidity, and spasticity at various severities. The SEA-based actuation system together with the proposed control system, i.e., consisting of feedback, feedforward, and disturbance

observer (DOB) controllers, was validated to be able to deliver accurate torque control during user interaction. Based on the clinical study results, this training simulator can be a clinically useful and cost-effective medical education tool to provide realistic and consistent practice opportunities for clinical learners to get proficient with rigidity and spasticity assessment techniques to reduce the need for human patients. This study represented the most difficult force control task so far because the device needed to track complex torque profiles, especially for spasticity (i.e., piecewise torque patterns with rapid changes), under strong motion disturbance as the trainees quickly moved through the ROM within one second. Therefore, additional model-based feedforward and DOB controllers were used to augment the original model-free feedback control, where the external trainee's motion was regarded as a disturbance source to be rejected. The control ablation test shown that feedforward and DOB controller significantly improved the tracking performance. Eventually, on our low-cost hardware (BOM cost < $ 2000), a high-fidelity torque control (torque error < 0.1 Nm) was achieved across simulated behaviors and severities under external disturbance.

Chapter 5 described our ongoing efforts to collect clinical data from a large group of spasticity and rigidity patients in parallel with the development of the robotic training simulators. Currently a pilot group of 15 spasticity patients have been tested. Using data from 10 subjects, we identified several improvements to the test protocol and sensor data analysis. The resulting dataset has been used to guide the choice of spasticity simulation parameters as we started to work on abnormal muscle behaviors at the elbow joint in Chapter 4.

6.2 Limitations and Future Work

Throughout the mechatronic, sensing, control development of two robotic training simulators, although the SEA-based robotic training simulators not only successfully achieved our initial engineering targets (e.g., cost-effectiveness, good force control capability) but also received very positive feedback from its clinical users, there are still several limitations associated with the current designs, and we hope this discussion could lay out potential future research directions.

Regarding the simulator mechatronic system design, comments from the clinical studies have suggested that ultimately the dexterity of the simulator should match the DOFs of the upper and lower extremities. For example, although we implemented a 2-DOF ankle joint (dorsiflexion-plantarflexion (DF-PF): active; inversion-eversion (I-E): passive) on the ankle-foot simulator, it will be also helpful to include knee and hip DOFs, since the assessment in supine configuration involves the coordinated movement of the entire leg (e.g., hip external rotation). Similarly, for the arm simulator, on top of the actuated elbow joint, a passive wrist joint was implemented via a ball socket design with adjustable friction. However, some clinical subjects expected more sophisticated haptic torque feedback at the wrist to mimic useful clinical signs found in other parts of the body (e.g., Parkinson's disease patient might develop lead-pipe or cogwheel rigidity at the wrist). In addition, currently both simulators only have one actuated DOF (ankle and elbow). Having multiple actuated DOFs on a single simulator could further enhance the hardware cost-efficiency and usefulness. This way the trainees could practice assessment techniques for multiple the joints in the upper or lower extremity without needing to switch back and forth between different simulators, and they could also practice the assessment that requires the coordination of multiple joints. Given the compact SEA-based actuation system, it should be relatively

straightforward to install additional custom SEAs at those large joints such as hip and knee and still keep all the components (e.g., transmission, spring cage) within the realistic arm or leg shrouds. However, for smaller joints with high DOFs such as wrist, ankle, and fingers, the design will be significantly more difficult. One potential solution could be utilizing SEAs at the large joints, but using miniature active brakes (such as an MRF brake) in the smaller joints without any transmission, or a combination of the two for a multi-DOF joint (e.g., at the ankle, a SEA for DF-PF and a MRF for I-E), similar to [146]. Essentially, deploying the SEA at the joint where active behaviors need to be produced (e.g., tremor, clonus, reflex response) and using the active brake where only passive resistance is observed (still can generate programable, complex resistance profiles). Considering that a few of the clinical expert subjects complained about the gear-meshing feeling and drivetrain vibration, another benefit of this approach is that a MRF brake could generate smoother resistance to better mimic human muscle tone compared to geared electric motors.

Regarding the choice of transmission and mechanical design details, a few lessons were learned. Except for the noise, vibration, and backlash, another reason why gear transmission is not ideal for the training simulator application is that high output torque would always occur on a few specific gear teeth regardless of the gear ratio (hunting or non-hunting). For example, if the catch angle is fixed in spasticity simulation, each time the high spastic catch torque would transmit through the same pair of gear teeth. Over time with repetitive practice trials from the trainees, these high torque-bearing teeth would be susceptible to premature failure though the rest of the gear teeth are well within their life span. A planetary-type gear transmission might be able to handle this issue since there are multiple gear teeth sustaining the load simultaneously (i.e., same as the number of planet gears). Alternatively, the belt drive used in the ankle-foot simulator might

distribute the output torque loading more uniformly and even out the wear on the drivetrain. However, the downside of using a belt drive in a SEA is that the intrinsic compliance of the belt would inevitably affect the overall effective stiffness of the drivetrain, since the belt is connected in series with the SEA, which further reduces the system control bandwidth. The stiffness of the linkage drive in the ankle-foot simulator is another concern. This drive consisted of four slender links (first fabricated with aluminum, and later changed to fiberglass) (Fig. 2.1). The buckling risk associated with the slender design (even though the components were designed with a safety factor considering the Euler's critical buckling load) and low material Young's modulus (~70 GPa for aluminum vs. ~17 GPa for fiberglass) might be another source of system compliance. A ball-screw drive might be a better alternative solution given its high stiffness, low backlash, high efficiency, and high load transmission capability in a compact form factor. However, it might be more expensive compared to other drivetrain solutions, so the design trade-off should be considered. Eventually, in retrospect, although many design considerations were accounted for in the spring cage design, when selecting the spring constant and specifying the deformation length, the shear stress on the spring coils should be analyzed and ideally needs to be kept below the endurance limit of the steel (approximately half of the yield strength) to avoid fatigue failure. Fortunately, we had a preload on the springs to ensure they were always in compression even at the largest deformation, which mitigated the cyclic loading condition, but this would worth considering in the future design.

For the control aspect, even though the control system proposed in Chapter 5 delivered very good control accuracy (torque error < 3 %), in this human-robot interaction scenario, depending on the body size, body posture, and technique of the trainee who operates the device (representing variable environmental dynamics), the force control scheme presented in Chapter 5

potentially might still have degraded performance. Therefore, more advanced variable-gain controllers might worth considering in the future. Furthermore, it might be interesting to run the benchtop control test with different investigators and observe if the tracking accuracy would vary with the investigator. This could lead a future research direction for force control in the human-robot interaction scenario and these simulators could be useful testbeds to evaluate the proposed algorithms. Force control that explicitly accounts for environmental dynamics is an open research topic and will have significance not only for SEAs [88], but also for a much boarder community, such as legged robots [124], powered exoskeletons [147], humanoids [76], etc.

Eventually, as these robotic training simulators are developed and validated in benchtop and clinical evaluations, the next phase of this research should shift its emphasis to the training effectiveness of robot-aided teaching for learning neurologic exam assessment technique. Potential comparison studies could be conducted to have different cohorts of students exposed to different training methods (practice patients vs. robotic training simulators) and evaluate their learning outcome as well as subjective feedback, similar to previous studies such as [148].

Furthermore, the trainees are not only limited to medical/clinical students, residents, and fellows, but instead potentially a much boarder audience might benefit from this technology. For example, these simulators could be used as a patient education tool to improve the treatment compliance and willingness. The device could present a spectrum of the severity level given an abnormal muscle behavior and demonstrate to the patients how their muscle tone would worsen if no proper intervention or management plans were implemented.

In addition, the spasticity replication at various MAS levels could be used to demonstrate the effect of Botox injection (also the effect of dosage). Practitioners who frequently need to assign Botox injection could get a haptic feeling of how much the spastic muscle would loosen up given

the specific dosage of an injection. Of course, in order to program the correlation between the decrease of muscle tone and the Botox dosage, a separate clinical quantification study would be required unless there are sufficient clinically-observed data exist in the literature. Eventually, the sale representatives from pharmaceutical companies, especially the ones who come from nonmedical background, could have a first-hand haptic knowledge of the pathological muscle behaviors through these devices, rather than learning through text-only training materials. This exposure could enhance their understanding towards the products they are advocating as well as their customer's needs.

All of these potential and interesting use cases were inspired via the interaction with industry representatives during public demonstrations of these devices, so future collaborations with industry might help to find their unique positioning in the market and transform the engineering prototypes into feasible and useful commercial products.

REFERENCES

[1] Mukherjee, A., and Chakravarty, A., 2010, "Spasticity Mechanisms - for the Clinician," Front. Neurol., **1**, p. 149.

[2] Pandyan, A. D., Gregoric, M., Barnes, M. P., Wood, D., Van Wijck, F., Burridge, J., Hermens, H., and Johnson, G. R., 2005, "Spasticity: Clinical Perceptions, Neurological Realities and Meaningful Measurement," Disabil. Rehabil., **27**(1–2), pp. 2–6.

[3] O'Sullivan, S. B., Schmitz, T. J., and Fulk, G. D., 2014, *Physical Rehabilitation*, F.A. Davis, Philadelphia, USA.

[4] Rekand, T., 2010, "Clinical Assessment and Management of Spasticity: A Review," Acta Neurol. Scand., **122**(SUPPL. 190), pp. 62–66.

[5] Barnes, Michael P., G. R. J., 2008, *Upper Motor Neurone Syndrome and Spasticity: Clinical Management and Neurophysiology*, Cambridge University Press., New York, USA.

[6] "Spasticity – Causes, Symptoms and Treatments" [Online]. Available: http://www.aans.org/Patients/Neurosurgical-Conditions-and-Treatments/Spasticity. [Accessed: 25-Jun-2018].

[7] Campbell, W. W., and DeJong, R. N., 2005, *DeJong's the Neurologic Examination*, Lippincott Williams & Wilkins, Philadelphia, USA.

[8] Nick, J. M., 2003, "Deep Tendon Reflexes: The What, Why, Where, and How of Tapping.," J. Obstet. Gynecol. Neonatal Nurs., **32**(3), pp. 297–306.

[9] Uysal, H., Boyraz, I., Yaĝcioĝlu, S., Oktay, F., Kafali, P., and Tönük, E., 2011, "Ankle Clonus and Its Relationship with the Medium-Latency Reflex Response of the Soleus by Peroneal Nerve Stimulation," J. Electromyogr. Kinesiol., **21**(3), pp. 438–444.

[10] Guttman, M., Kish, S. J., and Furukawa, Y., 2003, "Current Concepts in the Diagnosis and Management of Parkinson's Disease," Cmaj, **168**(3), pp. 293–301.

[11] Dauer, W., and Przedborski, S., 2003, "Parkinson's Disease: Mechanisms and Models," Neuron, **39**(6), pp. 889–909.

[12] Sepehri, B., Esteki, A., Ebrahimi-Takamjani, E., Shahidi, G. A., Khamseh, F., and Moinodin, M., 2007, "Quantification of Rigidity in Parkinson's Disease," Ann. Biomed. Eng., **35**(12), pp. 2196–2203.

[13] Ghiglione, P., Mutani, R., and Chiò, A., 2005, "Cogwheel Rigidity," Arch. Neurol., **62**(5), pp. 828–830.

[14] Calota, A., Feldman, A. G., and Levin, M. F., 2008, "Spasticity Measurement Based on Tonic Stretch Reflex Threshold in Stroke Using a Portable Device," Clin. Neurophysiol., **119**(10), pp. 2329–2337.

[15] McGibbon, C. A., Sexton, A., Jones, M., and O'Connell, C., 2013, "Elbow Spasticity during Passive Stretch-Reflex: Clinical Evaluation Using a Wearable Sensor System," J.

Neuroeng. Rehabil., **10**(1), p. 61.

[16] Pandyan, A., 1999, "A Review of the Properties and Limitations of the Ashworth and Midified Ashworth Scales as Measures of Spasticity," Clin. Rehabil., **13**, pp. 373–383.

[17] Biering-Sørensen, F., Nielsen, J. B., and Klinge, K., 2006, "Spasticity-Assessment: A Review," Spinal Cord, **44**(12), pp. 708–722.

[18] Allison, S. C., Abraham, L. D., and Petersen, C. L., 1996, "Reliability of the Modified Ashworth Scale in the Assessment of Plantarflexor Muscle Spasticity in Patients with Traumatic Brain Injury," Int. J. Rehabil. Res., **19**(1), pp. 67–78.

[19] Blackburn, M., van Vliet, P., and Mockett, S., 2002, "Reliability of Measurements Obtained With the Modified Ashworth Scale in the Lower Extremities of People With Stroke," Phys Ther, **82**(1), pp. 25–34.

[20] Kunkler, K., 2006, "The Role of Medical Simulation: An Overview," Int. J. Med. Robot. Comput. Assist. Surg., **2**, pp. 203 –210.

[21] Rosen, K. R., 2008, "The History of Medical Simulation," J. Crit. Care, **23**(2), pp. 157–166.

[22] Passiment, M., Sacks, H., and Huang, G., 2011, "Medical Simulation in Medical Education: Results of an AAMC Survey," Assoc. Am. Med. Coll., (September), pp. 1–48.

[23] Cantrell, M. J., and Deloney, L. A., 2007, "Integration of Standardized Patients into Simulation," Anesthesiol. Clin., **25**(2), pp. 377–383.

[24] Fujisawa, T., Takagi, M., Takahashi, Y., Inoue, K., Terada, T., Kawakami, Y., and Komeda, T., 2007, "Basic Research on the Upper Limb Patient Simulator," *2007 IEEE 10th International Conference on Rehabilitation Robotics, ICORR'07*, IEEE, Noordwijk, Netherlands, June 13-15, pp. 48–51.

[25] Brown, R. S., Graham, C. L., Richeson, N., Wu, J., and McDermott, S., 2010, "Evaluation of Medical Student Performance on Objective Structured Clinical Exams with Standardized Patients with and without Disabilities," Acad. Med., **85**(11), pp. 1766–1771.

[26] Jeon, C., 2015, "The Virtual Flier: The Link Trainer, Flight Simulation, and Pilot Identity," Technol. Cult., **56**(1), pp. 28–53.

[27] Myers, B., 1998, "A Brief History of Human Computer Interaction Technology," Interactions, **5**(2), pp. 44–54.

[28] Haug, E. J., Anderson, D., Berbaum, K., Evans, D., Hinrichs, J., Kim, S.-S., Kuhl, J., Lee, W.-S., Lenel, J., Stoner, J., Tsai, F.-T., Bernard, J., Malwitz, D., Turpin, D., Sinacori, J., Allen, W., and McAreavy, J., 1990, "Feasibility Study and Conceptual Design of a National Advanced Driving Simulator," (NHTSA Report DOTHS 807596), p. 334.

[29] Gordon, M. S., Ewy, G. A., DeLeon, A. C., Waugh, R. A., Felner, J. M., Forker, A. D., Gessner, I. H., Mayer, J. W., and Patterson, D., 1980, "'Harvey,' the Cardiology Patient Simulator: Pilot Studies on Teaching Effectiveness," Am. J. Cardiol., **45**(4), pp. 791–796.

[30] "Medical Simulation Market Size Report, 2021-2028" [Online]. Available:

https://www.grandviewresearch.com/industry-analysis/medical-healthcare-simulation-market. [Accessed: 04-Oct-2022].

[31] Al-Elq, A. H., 2010, “Simulation-Based Medical Teaching and Learning,” J. Fam. Community Med., **17**(1), pp. 35–40.

[32] Papp, C., Deeb, R. S., Booth, C., El-Sayed, A., and Freilicher, T., 2018, “Bridging Medical Simulation with Computer Science and Engineering: A Growing Field of Study,” Nurse Educ. Today, **71**(February), pp. 1–6.

[33] Colt, H. G., Crawford, S. W., and Galbraith, O., 2001, “Virtual Reality Bronchoscopy Simulation: A Revolution in Procedural Training,” Chest, **120**(4), pp. 1333–1339.

[34] Boulet, J. R., Murray, D., Kras, J., Woodhouse, J., McAllister, J., and Ziv, A., 2003, “Reliability and Validity of a Simulation-Based Acute Care Skills Assessment for Medical Students and Residents,” Anesthesiology, **99**(6), pp. 1270–1280.

[35] Morgan, P. J., and Cleave-Hogg, D., 2002, “Comparison between Medical Students’ Experience, Confidence and Competence,” Med. Educ., **36**(6), pp. 534–539.

[36] “New Study: Frost & Sullivan Report Shows Payback Takes Under Six Months for Immersion Medical Training Simulators - Immersion Corporation” [Online]. Available: https://ir.immersion.com/news-releases/news-release-details/new-study-frost-sullivan-report-shows-payback-takes-under-six. [Accessed: 04-Oct-2022].

[37] Deng, A., Wang, J. J., and Tsui, B. C. H., 2020, “Keeping Trainees Safe in a Pandemic: The Evolving Role of Medical Simulation Training,” Can. J. Anesth., **67**(9), pp. 1292–1293.

[38] “Benefits of Simulation in Education | USAHS” [Online]. Available: https://www.usa.edu/blog/simulation-in-education/. [Accessed: 03-Oct-2022].

[39] “Nursing Mannequin | Healthcare Simulation | HealthySimulation.Com” [Online]. Available: https://www.healthysimulation.com/nursing-mannequin/. [Accessed: 03-Oct-2022].

[40] “Emergency Care Patient Simulator - HeartWorks - Intelligent Ultrasound - for General Care / for Cardiopulmonary Care / Cardiac Surgery” [Online]. Available: https://www.medicalexpo.com/prod/intelligent-ultrasound/product-301944-1018076.html. [Accessed: 03-Oct-2022].

[41] Linde, A. S., and Kunkler, K., 2016, “The Evolution of Medical Training Simulation in the U.S. Military,” Stud. Health Technol. Inform., **220**(October), pp. 209–214.

[42] Satava, R. M., 2001, “Accomplishments and Challenges of Surgical Simulation: Dawning of the next-Generation Surgical Education,” Surg. Endosc., **15**(3), pp. 232–241.

[43] Edmond, J., Wiet, G. J., and Bolger, L. T. C. B., 1998, “Virtual Environments: Surgical Simulation in Otolaryngology,” Otolaryngol. Clin. North Am., **31**(2), pp. 369–381.

[44] Raibert, M., Playter, R., and Krummel, T. M., 1998, “The Use of a Virtual Reality Haptic Device in Surgical Training,” Acad. Med., **73**(5), p. 596.

[45] Metatla, O., Martin, F., Parkinson, A., Bryan-Kinns, N., Stockman, T., and Tanaka, A., 2016, "Audio-Haptic Interfaces for Digital Audio Workstations: A Participatory Design Approach," J. Multimodal User Interfaces, **10**(3), pp. 247–258.

[46] "Novint Falcon" [Online]. Available: http://ai.stanford.edu/~conti/falcon.html. [Accessed: 17-Oct-2022].

[47] Massie, T. H., Salisbury, J. K., and Kenneth Salisbury, J., 1994, "The PHANTOM Haptic Interface: A Device for Probing Virtual," Proc. ASME Winter Annu. Meet. Symp. Haptic Interfaces Virtual Environ. Teleoperator Syst., **55**(1), pp. 295–300.

[48] Park, H. S., Kim, J., and Damiano, D. L., 2012, "Development of a Haptic Elbow Spasticity Simulator (HESS) for Improving Accuracy and Reliability of Clinical Assessment of Spasticity," IEEE Trans. Neural Syst. Rehabil. Eng., **20**(3), pp. 361–370.

[49] Grow, D. I., Wu, M., Locastro, M. J., Arora, S. K., Bastian, A. J., and Okamura, A. M., 2008, "Haptic Simulation of Elbow Joint Spasticity," *Symposium on Haptics Interfaces for Virtual Environment and Teleoperator Systems 2008 - Proceedings, Haptics*, IEEE, Reno, USA, March 13-14, pp. 475–476.

[50] Wang, C., Noh, Y., Ebihara, K., Terunaga, C., Tokumoto, M., Okuyama, I., Yusuke, M., Ishii, H., Takanishi, A., Hatake, K., and Shoji, S., 2012, "Development of an Arm Robot for Neurologic Examination Training," *IEEE International Conference on Intelligent Robots and Systems*, IEEE, Vilamoura-Algarve, Portugal, October 7-12, pp. 1090–1095.

[51] Ishikawa, S., Okamoto, S., Isogai, K., Akiyama, Y., Yanagihara, N., and Yamada, Y., 2015, "Assessment of Robotic Patient Simulators for Training in Manual Physical Therapy Examination Techniques," PLoS One, **10**(4), p. e0126392.

[52] Takhashi, Y., Komeda, T., Koyama, H., Yamamoto, S.-I., Arimatsu, T., Kawakami, Y., Inoue, K., and Ito, Y., 2011, "Development of an Upper Limb Patient Simulator for Physical Therapy Exercise," *2011 IEEE International Conference on Rehabilitation Robotics*, IEEE, Zurich, Switzerland, June 29 - July 1, pp. 1–4.

[53] Liang, J., Pei, Y., Ewoldt, R. H., Tippett, S. R., and Hsiao-Wecksler, E. T., 2020, "Passive Hydraulic Training Simulator for Upper Arm Spasticity," J. Mech. Robot., **12**(4), p. 045001 (9 pages).

[54] Kikuchi, T., Oda, K., and Furusho, J., 2010, "Leg-Robot for Demonstration of Spastic Movements of Brain-Injured Patients with Compact Magnetorheological Fluid Clutch," Adv. Robot., **24**(5–6), pp. 671–686.

[55] Okumura, H., Okamoto, S., Ishikawa, S., Isogai, K., Yanagihara-Yamada, N., Akiyama, Y., and Yamada, Y., 2015, "Exoskeleton Simulator of Impaired Ankle: Simulation of Spasticity and Clonus," *Haptic Interaction*, Springer, Tokyo, pp. 209–214.

[56] Pei, Y., Ewoldt, R. H., Zallek, C. M., and Hsiao-Wecksler, E. T., 2021, "Design Framework and Clinical Evaluation of a Passive Hydraulic Patient Simulator for Biceps Spasticity Assessment Training," J. Mech. Robot., **13**(4), p. 041006.

[57] Gim, K. G., He, M., Mansouri, M., Pei, Y., Ripperger, E., Zallek, C. M., and Hsiao-Wecksler, E. T., 2021, "Development of a Series Elastic Elbow Neurological Exam

Training Simulator for Lead-Pipe Rigidity," *Proceedings - IEEE International Conference on Robotics and Automation*, IEEE, Xian, China, May 30 - June 5, pp. 10340–10346.

[58] Pei, Y., Han, T., Zallek, C. M., Liu, T., Yang, L., and Hsiao-Wecksler, E. T., 2021, "Design and Clinical Validation of a Robotic Ankle-Foot Simulator with Series Elastic Actuator for Ankle Clonus Assessment Training," IEEE Robot. Autom. Lett., **6**(2), pp. 3793–3800.

[59] Wensing, P. M., Wang, A., Seok, S., Otten, D., Lang, J., and Kim, S., 2017, "Proprioceptive Actuator Design in the MIT Cheetah: Impact Mitigation and High-Bandwidth Physical Interaction for Dynamic Legged Robots," IEEE Trans. Robot., **33**(3), pp. 509–522.

[60] Seok, S., Wang, A., Chuah, M. Y., Hyun, D. J., Lee, J., Otten, D. M., Lang, J. H., and Kim, S., 2015, "Design Principles for Energy-Efficient Legged Locomotion and Implementation on the MIT Cheetah Robot," IEEE/ASME Trans. Mechatronics, **20**(3), pp. 1117–1129.

[61] Kenneally, G., De, A., and Koditschek, D. E., 2016, "Design Principles for a Family of Direct-Drive Legged Robots," IEEE Robot. Autom. Lett., **1**(2), pp. 900–907.

[62] Massie, T. H., Salisbury, J. K., and Kenneth Salisbury, J., 1994, "The PHANTOM Haptic Interface: A Device for Probing Virtual," Proc. ASME Winter Annu. Meet. Symp. Haptic Interfaces Virtual Environ. Teleoperator Syst., **55**(1), pp. 1–6.

[63] Ramos, J., Wang, A., Ubellacker, W., Mayo, J., and Kim, S., 2015, "A Balance Feedback Interface for Whole-Body Teleoperation of a Humanoid Robot and Implementation in the HERMES System," IEEE-RAS Int. Conf. Humanoid Robot., **2015-Decem**, pp. 844–850.

[64] Maron, C., Dieckmann, T., Hauck, S., and Prinzler, H., 1997, "Electromechanical Brake System: Actuator Control Development System," SAE Tech. Pap., **1**(412).

[65] Bossis, G., Lacis, S., Meunier, A., and Volkova, O., 2002, "Magnetorheological Fluids," J. Magn. Magn. Mater., **252**, pp. 224–228.

[66] Rossa, C., Jaegy, A., Lozada, J., and Micaelli, A., 2014, "Design Considerations for Magnetorheological Brakes," IEEE/ASME Trans. Mechatronics, **19**(5), pp. 1669–1680.

[67] Liu, G., Gao, F., Wang, D., and Liao, W. H., 2022, "Medical Applications of Magnetorheological Fluid: A Systematic Review," Smart Mater. Struct., **31**(4).

[68] "Industrial Suspension Systems | LORD Corp" [Online]. Available: https://www.lord.com/products-and-solutions/active-vibration-control/industrial-suspension-systems. [Accessed: 05-Oct-2022].

[69] Line, C., Manzie, M. C., and Good, M. C., 2008, "Electromechanical Brake Modeling and Control: From PI to MPC," IEEE Trans. Control Syst. Technol., **16**(3), pp. 446–457.

[70] Kikuchi, T., Oda, K., Yamaguchi, S., and Furusho, J., 2010, "Leg-Robot with MR Clutch to Realize Virtual Spastic Movements," J. Intell. Mater. Syst. Struct., **21**(15), pp. 1523–1529.

[71] Song, S. Y., Pei, Y., Tippett, S. R., Lamichhane, D., Zallek, C. M., and Hsiao-Wecksler, E. T., 2018, "Validation of a Wearable Position, Velocity, and Resistance Meter for Assessing Spasticity and Rigidity," *Frontiers in Biomedical Devices, BIOMED - 2018 Design of Medical Devices Conference, DMD 2018*, ASME, Minneapolis, USA, April 9–12, p. V001T10A007.

[72] Song, S. Y., Pei, Y., Liang, J., and Hsiao-Wecksler, E. T., 2017, "Design of a Portable Position, Velocity, and Resistance Meter (PVRM) for Convenient Clinical Evaluation of Spasticity or Rigidity," *Frontiers in Biomedical Devices, BIOMED - 2017 Design of Medical Devices Conference, DMD 2017*, ASME, Minneapolis, USA, April 10-13, p. V001T11A020.

[73] Pei, Y., Feng, Y., Song, S. Y. S. Y., Zallek, C. M. C. M., Liu, T., and Hsiao-Wecksler, E. T. E. T., 2022, "Quantification of Elbow Spasticity (Preliminary Results)," *North American Congress on Biomechanics*, Ottawa, Canada, August 21-25.

[74] Rollinson, D., Bilgen, Y., Brown, B., Enner, F., Ford, S., Layton, C., Rembisz, J., Schwerin, M., Willig, A., Velagapudi, P., and Choset, H., 2014, "Design and Architecture of a Series Elastic Snake Robot," *IEEE International Conference on Intelligent Robots and Systems*, IEEE, Chicago, USA, September 14-18, pp. 4630–4636.

[75] Minniti, M. V., Farshidian, F., Grandia, R., and Hutter, M., 2019, "Whole-Body MPC for a Dynamically Stable Mobile Manipulator," IEEE Robot. Autom. Lett., **4**(4), pp. 3687–3694.

[76] Paine, N., Mehling, J. S., Holley, J., Radford, N. A., Johnson, G., Fok, C.-L., and Sentis, L., 2015, "Actuator Control for the NASA-JSC Valkyrie Humanoid Robot: A Decoupled Dynamics Approach for Torque Control of Series Elastic Robots," J. F. Robot., **32**(3), pp. 378–396.

[77] Hutter, M., Gehring, C., Jud, D., Lauber, A., Bellicoso, C. D., Tsounis, V., Hwangbo, J., Bodie, K., Fankhauser, P., Bloesch, M., Diethelm, R., Bachmann, S., Melzer, A., and Hoepflinger, M., 2016, "ANYmal - A Highly Mobile and Dynamic Quadrupedal Robot," *IEEE International Conference on Intelligent Robots and Systems*, IEEE, Daejeon, Korea, October 9-14, pp. 38–44.

[78] Rouse, E. J., Mooney, L. M., and Herr, H. M., 2014, "Clutchable Series-Elastic Actuator: Implications for Prosthetic Knee Design," Int. J. Rob. Res., **33**(13), pp. 1611–1625.

[79] Abate, A. M., 2018, "Mechanical Design for Robot Locomotion," Ph.D. Dissertation, Robotics Program, Oregon State University.

[80] "Sawyer, the High Performance Collaborative Robot | Rethink Robotics" [Online]. Available: https://www.rethinkrobotics.com/sawyer. [Accessed: 21-Mar-2022].

[81] Pratt, G. A., and Williamson, M. M., 1995, "Series Elastic Actuators," *IEEE International Conference on Intelligent Robots and Systems*, IEEE, Pittsburgh, USA, August 5-9, pp. 399–406.

[82] Pratt, J., Krupp, B., and Morse, C., 2002, "Series Elastic Actuators for High Fidelity Force Control," Ind. Robot An Int. J., **29**(3), pp. 234–241.

[83] Eppinger, S. D., and Seering, W. P., 1992, "Three Dynamic Problems in Robot Force Control," IEEE Trans. Robot. Autom., **8**(6), pp. 751–758.

[84] Seok, S., Wang, A., Otten, D., and Kim, S., 2012, "Actuator Design for High Force Proprioceptive Control in Fast Legged Locomotion," *IEEE International Conference on Intelligent Robots and Systems*, IEEE, Vilamoura-Algarve, Portugal, October 7-12, pp. 1970–1975.

[85] "Atlas™ | Boston Dynamics" [Online]. Available: https://www.bostondynamics.com/atlas. [Accessed: 09-Oct-2022].

[86] Katz, B., Carlo, J. DI, and Kim, S., 2019, "Mini Cheetah: A Platform for Pushing the Limits of Dynamic Quadruped Control," *Proceedings - IEEE International Conference on Robotics and Automation*, IEEE, Montreal, Canada, May 20-24, pp. 6295–6301.

[87] Whitney, D. E., 1987, "Historical Perspective and State of the Art in Robot Force Control," Int. J. Rob. Res., **6**(1), pp. 3–14.

[88] Calanca, A., and Fiorini, P., 2018, "A Rationale for Acceleration Feedback in Force Control of Series Elastic Actuators," IEEE Trans. Robot., **34**(1), pp. 48–61.

[89] Williamson, M. M., 1995, "Series Elastic Actuators," M.S. Thesis, Department of Electrical Engineering and Computer Science, Massachusetts Institute of Technology.

[90] Sensinger, J. W., and Weir, R. F., 2007, "Improvements to Series Elastic Actuators," *Proceedings of the 2nd IEEE/ASME International Conference on Mechatronic and Embedded Systems and Applications, MESA 2006*, IEEE, Beijing, China, August 13-16.

[91] Wyeth, G., 2008, "Demonstrating the Safety and Performance of a Velocity Sourced Series Elastic Actuator," *Proceedings - IEEE International Conference on Robotics and Automation*, IEEE, Pasadena, USA, May 19-23, pp. 3642–3647.

[92] Eppinger, S., and Seering, W., 1987, "Understanding Bandwidth Limitations in Robot Force Control," *Proceedings. 1987 IEEE International Conference on Robotics and Automation*, IEEE, Raleigh, USA, March 31 - April 3, pp. 904–909.

[93] William T Townsend, J. K. S., 1989, "Mechanical Bandwidth as a Guideline to High-Performance Manipulator Design," *1989 IEEE International Conference on Robotics and Automation*, IEEE, Scottsdale, USA, May 14-19, pp. 1390–1395.

[94] LeWitt, P. A., 2014, "Clonus," Encycl. Neurol. Sci., **1**(1976), pp. 806–806.

[95] Gottlieb, G. L., and Agarwal, G. C., 1977, "Physiological Clonus in Man," Exp. Neurol., **54**(3), pp. 616–621.

[96] Rossi, A., Mazzocchio, R., and Scarpini, C., 1990, "Clonus in Man: A Rhythmic Oscillation Maintained by a Reflex Mechanism," Electroencephalogr. Clin. Neurophysiol., **75**(1–2), pp. 56–63.

[97] Boyraz, I., Uysal, H., Koc, B., and Sarman, H., 2015, "Clonus: Definition, Mechanism, Treatment," Med. Glas., **12**(1), pp. 19–26.

[98] Hidler, J. M., and Rymer, W. Z., 1999, "A Simulation Study of Reflex Instability in

Spasticity: Origins of Clonus," IEEE Trans. Rehabil. Eng., **7**(3), pp. 327–340.

[99] Walsh, E. G., and Wright, G. W., 1987, "Patellar Clonus: An Autonomous Central Generator," J. Neurol. Neurosurg. Psychiatry, **50**(9), pp. 1225–1227.

[100] Manella, K. J., Roach, K. E., and Field-Fote, E. C., 2017, "Temporal Indices of Ankle Clonus and Relationship to Electrophysiologic and Clinical Measures in Persons with Spinal Cord Injury," J. Neurol. Phys. Ther., **41**(4), pp. 229–238.

[101] Beres-Jones, J. A., Johnson, T. D., and Harkema, S. J., 2003, "Clonus after Human Spinal Cord Injury Cannot Be Attributed Solely to Recurrent Muscle-Tendon Stretch," Exp Brain Res, **149**, pp. 222–236.

[102] Butler, J. E., Godfrey, S., and Thomas, C. K., 2006, "Depression of Involuntary Activity in Muscle Paralyzed by Spinal Cord Injury," Muscle and Nerve, **33**(5), pp. 637–44.

[103] Dimitrijevic, M. R., Nathan, P. W., and Sherwood, A. M., 1980, "Clonus: The Role of Central Mechanisms," J. Neurol. Neurosurg. Psychiatry, **43**(4), pp. 321–332.

[104] Wallace, D. M., Ross, B. H., and Thomas, C. K., 2005, "Motor Unit Behavior during Clonus," J. Appl. Physiol., **99**(6), pp. 2166–2172.

[105] De Vlugt, E., de Groot, J. H., Wisman, W. H. J., and Meskers, C. G. M., 2012, "Clonus Is Explained from Increased Reflex Gain and Enlarged Tissue Viscoelasticity," J. Biomech., **45**(1), pp. 148–155.

[106] De Vlugt, E., De Groot, J. H., Schenkeveld, K. E., Arendzen, J. H., Van Der Helm, F. C., and Meskers, C. G., 2010, "The Relation between Neuromechanical Parameters and Ashworth Score in Stroke Patients," J. Neuroeng. Rehabil., **7**(1), pp. 5–7.

[107] De Leva, P., 1996, "Adjustments to Zatsiorsky-Seluyanov's Segment Inertia Parameters," J. Biomech., **29**(9), pp. 1223–1230.

[108] Pratt, J., Krupp, B., and Morse, C., 2002, "Series Elastic Actuators for High Fidelity Force Control," Ind. Robot An Int. J., **29**(3), pp. 234–241.

[109] Garag, P., 2019, "Mechatronic and Biomechanical Considerations toward the Design of an Ankle Clonus Simulator," M.S. Thesis, Department of Mechanical Science and Engineering, University of Illinois at Urbana-Champaign.

[110] Hallett, M., 1993, "Ninds Myotatic Reflex Scale," Neurology, **43**(12), p. 2723.

[111] Chung, S. G., van Rey, E., Bai, Z., Rymer, W. Z., Roth, E. J., and Zhang, L. Q., 2008, "Separate Quantification of Reflex and Nonreflex Components of Spastic Hypertonia in Chronic Hemiparesis," Arch. Phys. Med. Rehabil., **89**(4), pp. 700–710.

[112] Mirbagheri, M. M., Barbeau, H., and Kearney, R. E., 2000, "Intrinsic and Reflex Contributions to Human Ankle Stiffness: Variation with Activation Level and Position," Exp. Brain Res., **135**(4), pp. 423–436.

[113] Mirbagheri, M. M., and Kearney, R. E., 2000, "Mechanisms Underlying a Third-Order Parametric Model of Dynamic Reflex Stiffness," *Annual International Conference of the IEEE Engineering in Medicine and Biology - Proceedings*, IEEE, Chicago, USA, July 23-

28, pp. 924–927.

[114] Mirbagheri, M. M., Barbeau, H., Ladouceur, M., and Kearney, R. E., 2001, "Intrinsic and Reflex Stiffness in Normal and Spastic, Spinal Cord Injured Subjects," Exp. Brain Res., **141**(4), pp. 446–459.

[115] Pick, A. J., and Cole, D. J., 2008, "A Mathematical Model of Driver Steering Control Including Neuromuscular Dynamics," J. Dyn. Syst. Meas. Control. Trans. ASME, **130**(3).

[116] Meinhold, W., Yamakawa, Y., Honda, H., Mori, T., Izumi, S. I., and Ueda, J., 2021, "A Smart Tendon Hammer System for Remote Neurological Examination," Front. Robot. AI, **8**(March), pp. 1–6.

[117] Kim, K. J., Hwang, I. K., and Wertsch, J. J., 2002, "Development of a Quantitative Reflex Hammer for Measurement of Tendon Stretch Reflex," IEEE Trans. Neural Syst. Rehabil. Eng., **10**(3), pp. 165–169.

[118] Xia, R., 2012, "Etiology and Pathophysiology of Parkinson's Disease," *Etiology and Pathophysiology of Parkinson's Disease*, InTech, Vienna, Austria, pp. 485–506.

[119] Findley, L. J., Gresty, M. A., and Halmagyi, G. M., 1981, "Tremor, the Cogwheel Phenomenon and Clonus in Parkinson's Disease," J. Neurol. Neurosurgery, Psychiatry, **44**, pp. 534–546.

[120] Pandyan, A. D., Gregoric, M., Barnes, M. P., Wood, D., Van Wijck, F., Burridge, J., Hermens, H., and Johnson, G. R., 2005, "Spasticity: Clinical Perceptions, Neurological Realities and Meaningful Measurement," Disabil. Rehabil., **27**(1–2), pp. 2–6.

[121] Mutlu, A., Livanelioglu, A., and Gunel, M. K., 2008, "Reliability of Ashworth and Modified Ashworth Scales in Children with Spastic Cerebral Palsy," BMC Musculoskelet. Disord., **9**(1), p. 44.

[122] Wang, C., Duan, L., Li, M., Lu, Z., Shen, Y., Wei, J., Shi, Q., Wang, Y., Zecca, M., Li, W., and Wu, Z., 2015, "Development an Arm Robot to Simulate the Lead-Pipe Rigidity for Medical Education," *2015 IEEE International Conference on Information and Automation, ICIA 2015 - In Conjunction with 2015 IEEE International Conference on Automation and Logistics*, IEEE, Lijiang, China, August 8-10, pp. 619–624.

[123] Oh, S., and Kong, K., 2017, "High-Precision Robust Force Control of a Series Elastic Actuator," IEEE/ASME Trans. Mechatronics, **22**(1), pp. 71–80.

[124] Boaventura, T., Focchi, M., Frigerio, M., Buchli, J., Semini, C., Medrano-Cerda, G. A., and Caldwell, D. G., 2012, "On the Role of Load Motion Compensation in High-Performance Force Control," *IEEE International Conference on Intelligent Robots and Systems*, IEEE, Vilamoura-Algarve, Portugal, October 7-12, pp. 4066–4071.

[125] Vallery, H., Veneman, J., van Asseldonk, E., Ekkelenkamp, R., Buss, M., and van Der Kooij, H., 2008, "Compliant Actuation of Rehabilitation Robots," IEEE Robot. Autom. Mag., **15**(3), pp. 60–69.

[126] Kong, K., Bae, J., and Tomizuka, M., 2009, "Control of Rotary Series Elastic Actuator for Ideal Force-Mode Actuation in Human-Robot Interaction Applications," IEEE/ASME

Trans. Mechatronics, **14**(1), pp. 105–118.

[127] Kong, K., Bae, J., and Tomizuka, M., 2012, "A Compact Rotary Series Elastic Actuator for Human Assistive Systems," IEEE/ASME Trans. Mechatronics, **17**(2), pp. 288–297.

[128] Calanca, A., and Fiorini, P., 2014, "Human-Adaptive Control of Series Elastic Actuators," Robotica, **32**(8), pp. 1301–1316.

[129] Grun, M., Muller, R., and Konigorski, U., 2012, "Model Based Control of Series Elastic Actuators," *Proceedings of the IEEE RAS and EMBS International Conference on Biomedical Robotics and Biomechatronics*, Rome, Italy, June 24-27, pp. 538–543.

[130] Song, S. Y., 2019, "Quantification of Spasticity and Rigidity for Biceps and Triceps Using the PVRM (Position, Velocity, and Resistance Meter)," M.S. Thesis, Department of Mechanical Science and Engineering, University of Illinois at Urbana-Champaign.

[131] He, M., Mansouri, M., Pei, Y., Pedroza, I., Zallek, C. M., and Hsiao-Wecksler, E. T., 2022, "Clinical Validation Testing of an Upper Limb Robotic Medical Education Training Simulator for Rigidity Assessment," *Proceedings of the 2022 Design of Medical Devices Conference, DMD 2022*, Minneapolis, USA, April 11–14, p. V001T06A008.

[132] Vallery, H., Ekkelenkamp, R., Van Der Kooij, H., and Buss, M., 2007, "Passive and Accurate Torque Control of Series Elastic Actuators," *IEEE International Conference on Intelligent Robots and Systems*, IEEE, San Diego, USA, October 29 - November 2, pp. 3534–3538.

[133] Pratt, G. A. G. A., Willisson, P., Bolton, C., and Hofman, A., 2004, "Late Motor Processing in Low-Impedance Robots: Impedance Control of Series-Elastic Actuators," Am. Control Conf. 2004. Proc. 2004, **4**, pp. 3245–3251.

[134] Sariyildiz, E., Oboe, R., and Ohnishi, K., 2020, "Disturbance Observer-Based Robust Control and Its Applications: 35th Anniversary Overview," IEEE Trans. Ind. Electron., **67**(3), pp. 2042–2053.

[135] Yu, H., Huang, S., Chen, G., and Thakor, N., 2013, "Control Design of a Novel Compliant Actuator for Rehabilitation Robots," Mechatronics, **23**, pp. 1072–1083.

[136] Paine, N., Oh, S., and Sentis, L., 2014, "Design and Control Considerations for High-Performance Series Elastic Actuators," IEEE/ASME Trans. Mechatronics, **19**(3), pp. 1080–1091.

[137] Keemink, A. Q. L., van der Kooij, H., and Stienen, A. H. A., 2018, "Admittance Control for Physical Human–Robot Interaction," Int. J. Rob. Res., **37**(11), pp. 1421–1444.

[138] Bohannon, R. W., and Smith, M. B., 1987, "Interrater Reliability of a Modified Ashworth Scale of Muscle Spasticity," Phys Ther., **67**(2), pp. 206–207.

[139] Goetz, C. G., Tilley, B. C., Shaftman, S. R., Stebbins, G. T., Fahn, S., Martinez-Martin, P., Poewe, W., Sampaio, C., Stern, M. B., Dodel, R., Dubois, B., Holloway, R., Jankovic, J., Kulisevsky, J., Lang, A. E., Lees, A., Leurgans, S., LeWitt, P. A., Nyenhuis, D., Olanow, C. W., Rascol, O., Schrag, A., Teresi, J. A., van Hilten, J. J., LaPelle, N., Agarwal, P., Athar, S., Bordelan, Y., Bronte-Stewart, H. M., Camicioli, R., Chou, K.,

Cole, W., Dalvi, A., Delgado, H., Diamond, A., Dick, J. P., Duda, J., Elble, R. J., Evans, C., Evidente, V. G., Fernandez, H. H., Fox, S., Friedman, J. H., Fross, R. D., Gallagher, D., Goetz, C. G., Hall, D., Hermanowicz, N., Hinson, V., Horn, S., Hurtig, H., Kang, U. J., Kleiner-Fisman, G., Klepitskaya, O., Kompoliti, K., Lai, E. C., Leehey, M. L., Leroi, I., Lyons, K. E., McClain, T., Metzer, S. W., Miyasaki, J., Morgan, J. C., Nance, M., Nemeth, J., Pahwa, R., Parashos, S. A., Schneider, J. S. J. S., Schrag, A., Sethi, K., Shulman, L. M., Siderowf, A., Silverdale, M., Simuni, T., Stacy, M., Stern, M. B., Stewart, R. M., Sullivan, K., Swope, D. M., Wadia, P. M., Walker, R. W., Walker, R., Weiner, W. J., Wiener, J., Wilkinson, J., Wojcieszek, J. M., Wolfrath, S., Wooten, F., Wu, A., Zesiewicz, T. A., and Zweig, R. M., 2008, "Movement Disorder Society-Sponsored Revision of the Unified Parkinson's Disease Rating Scale (MDS-UPDRS): Scale Presentation and Clinimetric Testing Results," Mov. Disord., **23**(15), pp. 2129–2170.

[140] Wissel, J., Verrier, M., Simpson, D. M., Charles, D., Guinto, P., Papapetropoulos, S., and Sunnerhagen, K. S., 2015, "Post-Stroke Spasticity: Predictors of Early Development and Considerations for Therapeutic Intervention," PM R, **7**(1), pp. 60–67.

[141] Thomaz, S. R., Cipriano, G., Formiga, M. F., Fachin-Martins, E., Cipriano, G. F. B., Martins, W. R., and Cahalin, L. P., 2019, "Effect of Electrical Stimulation on Muscle Atrophy and Spasticity in Patients with Spinal Cord Injury – a Systematic Review with Meta-Analysis," Spinal Cord, **57**(4), pp. 258–266.

[142] Castro, M. J., Apple, D. F., Rogers, S., and Dudley, G. A., 2000, "Influence of Complete Spinal Cord Injury on Skeletal Muscle Mechanics within the First 6 Months of Injury," Eur. J. Appl. Physiol. Occup. Physiol., **81**(1–2), pp. 128–131.

[143] Seel, T., Raisch, J., and Schauer, T., 2014, "IMU-Based Joint Angle Measurement for Gait Analysis," Sensors (Switzerland), **14**(4), pp. 6891–6909.

[144] Nowka, D., Kok, M., and Seel, T., 2019, "On Motions That Allow for Identification of Hinge Joint Axes from Kinematic Constraints and 6D IMU Data," *2019 18th European Control Conference, ECC 2019*, Naples, Italy, June 25-28, pp. 4325–4331.

[145] Song, S. Y., Pei, Y., and Hsiao-Wecksler, E. T., 2022, "Estimating Relative Angles Using Two Inertial Measurement Units Without Magnetometers," IEEE Sens. J., **22**(20), pp. 19688–19699.

[146] Garcia, E., Arevalo, J. C., Muoz, G., and Gonzalez-De-Santos, P., 2011, "Combining Series Elastic Actuation and Magneto-Rheological Damping for the Control of Agile Locomotion," Rob. Auton. Syst., **59**(10), pp. 827–839.

[147] Aguirre-Ollinger, G., and Yu, H., 2021, "Lower-Limb Exoskeleton with Variable-Structure Series Elastic Actuators: Phase-Synchronized Force Control for Gait Asymmetry Correction," IEEE Trans. Robot., **37**(3), pp. 763–779.

[148] Luctkar-Flude, M., Wilson-Keates, B., and Larocque, M., 2012, "Evaluating High-Fidelity Human Simulators and Standardized Patients in an Undergraduate Nursing Health Assessment Course," Nurse Educ. Today, **32**(4), pp. 448–452.

[149] Beigzadeh, A., Bahmanbijari, B., Sharifpoor, E., and Rahimi, M., 2015, "Standardized Patients versus Simulated Patients in Medical Education: Are They the Same or

Different," J. Emerg. Pract. Trauma, **2**(1), pp. 25–28.

[150] Franklin, G. F., Powell, J. D., and Emami-Naeini, A., 2019, *Feedback Control of Dynamic Systems*, Pearson, New York, USA.

[151] Pei, Y., Zallek, C. M., and Hsiao-Wecksler, E. T., 2022, "Control Design and Preliminary Evaluation of a Medical Education Simulator for Ankle Tendon Reflex Assessment Training," *Proceedings of the 2022 Design of Medical Devices Conference, DMD 2022*, Minneapolis, USA, April 11–14, p. Vol. 84815, V001T06A007.

[152] Ifeachor, E. C., and Jervis, B. W., 2002, *Digital Signal Processing: A Practical Approach*, Pearson Education, London, UK.

APPENDIX A: SUPPLEMENTARY CLINICAL RESULTS FOR CHAPTER 4

This appendix presents the recorded results and feedback for each individual subject who participated in the clinical study in Chapter 4.

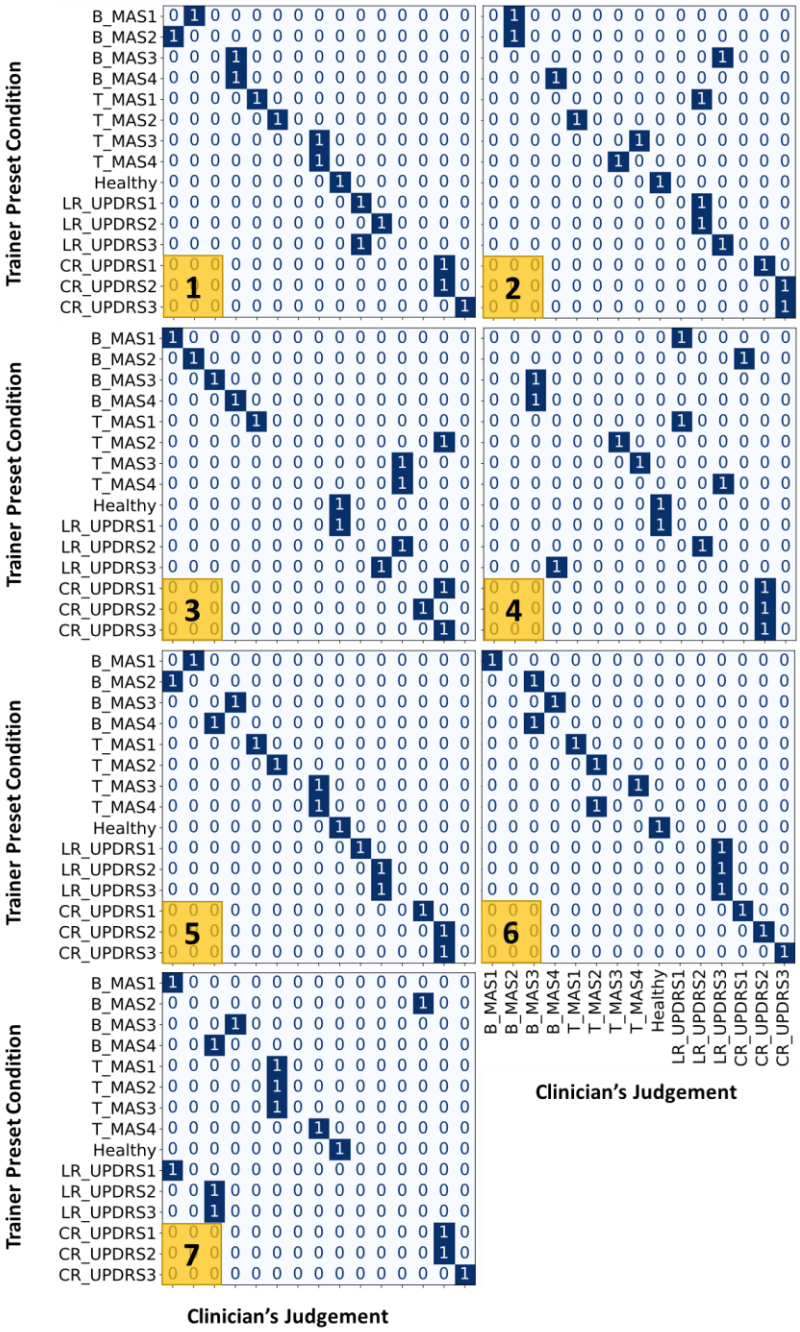

Fig. A1: Classification Test results of seven clinical subjects presented in confusion matrices.

Table A1: Disclosed Assessment Test results (mean and standard error) of seven clinical subjects for healthy, lead-pipe rigidity and cogwheel rigidity.

			Subject								
	Severity Level	**Simulation Aspect**	**1**	**2**	**3**	**4**	**5**	**6**	**7**	**Mean**	**SE**
Healthy	**/**	Resistance Magnitude	3	3	3	4	3	3	4	3.29	0.18
		Range of Motion	3	2	2	3	3	3	3	2.71	0.18
LR	**1**	Resistance Magnitude	3	3	3	4	4	4	4	3.57	0.20
		Range of Motion	3	3	3	3	3	3	3	3.00	0.00
	2	Resistance Magnitude	3	3	3	3	2	4	4	3.14	0.26
		Range of Motion	3	3	3	3	3	3	3	3.00	0.00
	3	Resistance Magnitude	2	3	2	3	1	3	3	2.43	0.30
		Range of Motion	3	3	3	3	3	3	3	3.00	0.00
CR	**1**	Cogwheel Frequency	3	3	3	3	3	3	3	3.00	0.00
		Cogwheel Magnitude	4	4	3	3	4	4	3	3.57	0.20
	2	Cogwheel Frequency	3	3	3	3	3	3	3	3.00	0.00
		Cogwheel Magnitude	3	3	3	3	3	4	4	3.29	0.18
	3	Cogwheel Frequency	3	3	3	3	3	3	3	3.00	0.00
		Cogwheel Magnitude	3	3	3	3	3	3	4	3.14	0.14

Table A2: Disclosed Assessment Test results (mean and standard error) of seven clinical subjects for biceps spasticity.

			Subject								
	Severity Level	**Simulation Aspect**	**1**	**2**	**3**	**4**	**5**	**6**	**7**	**Mean**	**SE**
SP-B	**1**	Catch Angle Location	3	4	4	3	4	4	4	3.71	0.18
		Catch Tone Amplitude	3	3	3	3	3	2	3	2.86	0.14
		Release Tone Amplitude	3	3	2	3	3	1	3	2.57	0.30
		Post-Catch Tone Amplitude	3	3	4	3	3	3	3	3.14	0.14
		Range of Motion	3	3	3	3	3	3	3	3.00	0.00
	2	Catch Angle Location	3	3	3	3	3	3	3	3.00	0.00
		Catch Tone Amplitude	3	3	2	3	3	3	3	2.86	0.14
		Release Tone Amplitude	3	3	3	3	3	3	3	3.00	0.00
		Post-Catch Tone Amplitude	3	3	3	3	3	3	3	3.00	0.00
		Range of Motion	3	3	3	3	3	3	3	3.00	0.00
	3	Catch Angle Location	3	3	3	3	3	3	3	3.00	0.00
		Catch Tone Amplitude	3	3	3	4	3	3	4	3.29	0.18
		Release Tone Amplitude	3	3	2	3	3	2	3	2.71	0.18
		Post-Catch Tone Amplitude	3	3	4	3	3	4	3	3.29	0.18
		Range of Motion	3	3	3	3	3	3	3	3.00	0.00
	4	Catch Angle Location	3	3	4	3	3	3	3	3.14	0.14
		Catch Tone Amplitude	3	3	3	3	2	5	4	3.29	0.36
		Release Tone Amplitude	3	3	2	3	3	3	3	2.86	0.14
		Post-Catch Tone Amplitude	3	3	4	3	3	4	3	3.29	0.18
		Range of Motion	3	3	3	3	3	3	3	3.00	0.00

Table A3: Disclosed Assessment Test results (mean and standard error) of seven clinical subjects for triceps spasticity.

			Subject								
	Severity Level	**Simulation Aspect**	**1**	**2**	**3**	**4**	**5**	**6**	**7**	**Mean**	**SE**
SP-T	**1**	Catch Angle Location	3	4	4	3	3	3	3	3.29	0.18
		Catch Tone Amplitude	3	3	3	3	3	3	3	3.00	0.00
		Release Tone Amplitude	3	3	2	3	3	2	3	2.71	0.18
		Post-Catch Tone Amplitude	4	3	4	3	4	3	3	3.43	0.20
		Range of Motion	3	3	3	3	3	3	3	3.00	0.00
	2	Catch Angle Location	3	3	3	3	3	3	3	3.00	0.00
		Catch Tone Amplitude	3	3	3	4	3	3	4	3.29	0.18
		Release Tone Amplitude	3	3	2	3	3	3	3	2.86	0.14
		Post-Catch Tone Amplitude	3	3	4	3	3	3	3	3.14	0.14
		Range of Motion	3	3	3	3	3	3	3	3.00	0.00
	3	Catch Angle Location	3	3	3	3	3	3	3	3.00	0.00
		Catch Tone Amplitude	3	3	3	5	3	3	4	3.43	0.30
		Release Tone Amplitude	3	3	2	3	2	2	3	2.57	0.20
		Post-Catch Tone Amplitude	4	3	5	3	4	4	3	3.71	0.29
		Range of Motion	3	3	3	3	3	3	3	3.00	0.00
	4	Catch Angle Location	3	3	3	3	4	3	3	3.14	0.14
		Catch Tone Amplitude	3	3	3	3	3	3	4	3.14	0.14
		Release Tone Amplitude	3	3	2	3	3	3	3	2.86	0.14
		Post-Catch Tone Amplitude	4	3	4	3	3	5	3	3.57	0.30
		Range of Motion	3	3	3	3	3	3	3	3.00	0.00